A SENSING METHODOLOGY FOR AN INTELLIGENT TRAFFIC SIGN INVENTORY AND CONDITION ASSESSMENT USING GPS/GIS, COMPUTER VISION AND MOBILE LIDAR TECHNOLOGIES

A Ph.D. Dissertation
Presented to
The Academic Faculty

By

Chengbo Ai

In Partial Fulfillment
Of the Requirements for the Degree
Doctor of Philosophy in the
School of Civil and Environmental Engineering

Georgia Institute of Technology
May 2013

A SENSING METHODOLOGY FOR AN INTELLIGENT TRAFFIC SIGN INVENTORY AND CONDITION ASSESSMENT USING GPS/GIS, COMPUTER VISION AND MOBILE LIDAR TECHNOLOGIES

Approved by:

Dr. Yi-Chang James Tsai, Advisor
School of Civil and Environmental Engineering
Georgia Institute of Technology

Dr. Zhaohua Wang
School of Center for GIS
Georgia Institute of Technology

Dr. Michael P. Hunter
School of Civil and Environmental Engineering
Georgia Institute of Technology

Dr. Michael D. Meyer
Private Company

Dr. Anthony J. Yezzi
School of Electrical and Computer Engineering
Georgia Institute of Technology

Date Approved: March 27th, 2013

In dedication to

my father, my mother, and my wife

for their constant support and unconditional love.

I love you all dearly!

ACKNOWLEDGEMENTS

I would like to express my deepest appreciation and thanks to my advisor, Dr. Yi-Chang James Tsai. His invaluable guidance, support, friendship, and generosity made this journey more enjoyable and fruitful. Without him, this dissertation would have been impossible. I could not have asked for a better mentor.

I would like to express my appreciation to Dr. Michael Hunter, Dr. Anthony Yezzi, Dr. Zhaohua Wang, and Dr. Michael Meyer for serving as my committee members. Their patient help and insightful guidance are greatly appreciated.

I would like to express my thanks to all my colleagues in my research group, Yi-Ching Wu, Feng Li, Zach Lewis, Chenglong Jiang, Chieh Wang, Daniel Luh, Bruno Pop-Stefanov, Roger Purcell, Jinqi Fang, Zhengbo Li, and Russell Aziz.

I would like to thank the members of my family for their unconditional love and support. It is their love that makes every piece of me today.

Last but not least, I would like to give my sincere thanks to my lovely wife, Yuanyuan Fang, for her unconditional love, constant support, and strong belief in me.

TABLE OF CONTENTS

LIST OF TABLES

Page

LIST OF FIGURES

SUMMARY

Traffic signs, which transportation agencies must inventory and manage, are one of the most important roadway assets because they are used to ensure roadway safety and provide important travel guidance/information. Traffic sign inventory and condition assessment are two important components that are essential for establishing a cost-effective and sustainable traffic sign management system. Traditionally, state departments of transportation (DOTs) have conducted traffic sign inventory and condition assessment manually, a process that is labor-intensive, time-consuming, and sometimes hazardous to field engineers in the roadway environment. Methods have been developed to automate sign inventory and condition assessment using video log images in previous studies. However, the performance of these methods still needs to be improved. Based on the need to inventory signs and manage them more effectively, this study has two focuses. The first focus is to develop an enhanced traffic sign detection methodology to improve the productivity of an image-based sign inventory for state DOTs. The proposed methodology includes two enhanced algorithms: a) a lighting dependent statistical color model (LD-SCM)-based color segmentation algorithm that is robust to different image lighting conditions, especially adverse lighting and b) an ordinary/partial differential equation (ODE/PDE)-based shape detection algorithm that is immune to discontinuous sign boundaries in a cluttered background. The second focus of the study is to explore a new traffic sign retroreflectivity condition assessment methodology to develop a mobile method that uses emerging computer vision and mobile light detection and ranging (LiDAR) technologies to assess traffic sign retroreflectivity conditions. The proposed methodology includes a) an image-LiDAR registration method employing camera calibration and point co-planarity to register the 3D LiDAR point cloud with 2D video log images, b) a theoretical-empirical normalization scheme to adjust the

magnitude of the LiDAR retro-intensity values with respect to LiDAR beam distance and incidence angle based on the radiometric responses, and c) a population-based retroreflectivity condition assessment method to evaluate the adequacy of a traffic sign retroreflectivity condition based on the correlation between the normalized LiDAR retro-intensity and the retroreflectivity values. For the proposed traffic sign detection methodology, comprehensive tests using representative datasets (e.g. with different road functions, data collection sources, and data qualities) were conducted to validate the performance of the two enhanced algorithms and the complete methodology. For the proposed retroreflectivity condition assessment methodology, the fundamental behavior of LiDAR retro-intensity was comprehensively tested and simulated under a controlled lab and roadway environment to quantify the impact of beam distance and incidence angle. A preliminary test on Type 1 engineer grade stop signs was conducted in the field to validate the performance of the proposed sign retro-reflectivity condition assessment method. The results from both of the proposed methodologies are promising.

CHAPTER 1

INTRODUCTION

1.1. Background

Traffic signs are one of the most important assets for transportation systems; they provide vital guidance to road users regarding traffic regulation, warnings, destination information, and temporary road condition information. Because of the vital role traffic signs play in roadway safety and information conveyance, they must be managed effectively by state departments of transportation (DOTs) using a traffic sign management system. A traffic sign management system is "a coordinated program of policies and procedures which ensure that the highway agency provides a sign system that meets the needs of the user most cost-effectively within available budget and constraints" (McGee & Paniati, 1998). It contains the four primary components shown in Figure 1-1 and described as follows:

- Inventory, which collects the locations and attributes of every individual traffic sign;
- Condition assessment, which determines the performance adequacy of inventoried signs by assessing retroreflectivity and identifying visual defects;
- Performance evaluation, which evaluates a traffic sign system's performance and predicts the performance and life of an individual sign or a group of signs in the system based on the collected condition data;
- Decision-making, which generates maintenance strategies, methods, and prioritizations based on the performance evaluation outcomes and available budget, and generates the needed annual budget based on expected safety requirements.

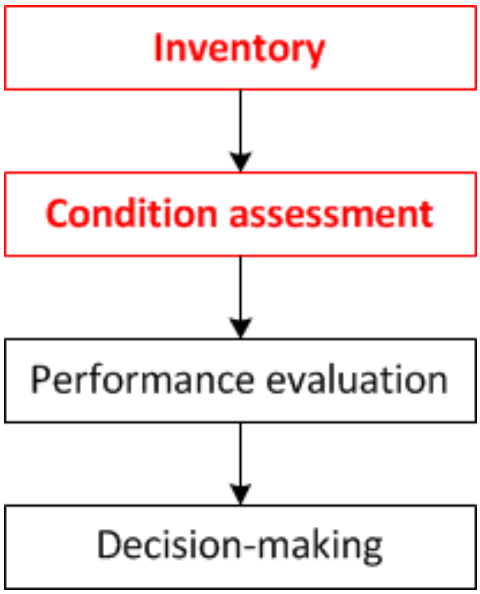

Figure 1-1 Diagram of the four primary components of a traffic sign management system

As pointed out by Wolshon (2003) and Rasdorf (2009), traffic sign inventory and condition assessment are the two most important components in a traffic sign management system. Management actions can only be effectively carried out with reliable inventory and condition assessment information.

During traffic sign inventory, detailed traffic sign information, including sign locations and attributes (e.g. type, dimension, lateral offset, etc.), is recorded and used to build a comprehensive traffic sign inventory database. Among all traffic sign information in a sign inventory database, identifying "where the traffic signs are" (i.e. traffic sign detection) is the first and most critical step, without which all the remaining sign attribute information cannot be acquired or populated in the database. However, most transportation agencies do not even have the information about where their traffic signs are along the road, not to mention the detailed traffic sign attribute information. There is an urgent need to develop methods to cost-effectively and reliably locate traffic signs first so that the remaining detailed traffic sign information can be populated and the subsequent management operations can be successfully carried out, e.g. condition assessment, performance evaluation, etc.

During traffic sign condition assessment, the traffic signs that do not meet requirements are identified by insufficient retroreflectivity and/or visual surface defects that interfere with traffic signs' displayed information (Howe, 2006). Among all the traffic sign conditions, traffic sign retroreflectivity condition is the most critical one for nighttime driving safety. There is an urgent need to develop methods to cost-effectively and reliably evaluate traffic sign retroreflectivity condition because the Federal Highway Administration (FHWA) has mandated minimum traffic sign retroreflectivity standards, which transportation agencies must implement.

Traditionally, traffic sign detection and retroreflectivity condition assessments have used manual methods in state DOTs. However, manual methods require field engineers to physically inspect and record the information of each individual traffic sign, which takes excessive time, consumes great amounts of labor, and sometimes puts field engineers in dangerous situations. To overcome the drawbacks of manual methods, some effort has been made to develop automated methods for both traffic sign detection and retroreflectivity condition assessment using video log images. However, the performance of these methods still needs to be improved so that they can be practically applied in state DOTs' practices. In recent years, emerging sensing technologies, e.g. computer vision, mobile light detection and ranging (LiDAR), etc. have advanced greatly so that current image-based automatic methods have been improved, and new traffic sign detection and retroreflectivity condition assessment methods have become possible. Consequently, this study focuses on the two key needs in the inventory and condition assessment components of a traffic sign management system: 1) developing an enhanced traffic sign detection methodology to improve the productivity of an image-based sign inventory for state DOTs, and 2) exploring and developing a new traffic sign retroreflectivity condition assessment methodology to cost-effectively and reliably assess traffic sign retroreflectivity conditions using the emerging computer vision and mobile LiDAR technologies.

1.2. Research Objective

The objective of this study is to propose a sensing methodology that takes advantage of computer vision and mobile LiDAR technologies supporting an intelligent traffic sign inventory and condition assessment. The specific objectives are as follows:

- Develop an enhanced traffic sign detection methodology to improve the productivity of an image-based sign inventory for state DOTs.
    - Develop new automated algorithms to ensure the enhanced traffic sign detection methodology produces a reliable outcome.
- Explore and develop a new traffic sign retroreflectivity condition assessment methodology employing the emerging computer vision and mobile LiDAR technologies.
    - Study the fundamental behavior of LiDAR retro-intensity values to reveal the feasibility of developing a mobile retroreflectivity condition assessment methodology by conducting simulated and field tests under controlled lab and roadway environments;
    - Develop new automated algorithms and methods to ensure the new traffic sign retroreflectivity condition assessment methodology produces a reliable and consistent outcome.

1.3. Dissertation Organization

The background of traffic sign inventory and retroreflectivity condition assessment is briefly introduced, and the research need and objectives are identified in Chapter 1. A literature review of current practices and studies of traffic sign inventory and traffic sign retroreflectivity condition assessment are presented in Chapter 2. The methodology for an enhanced traffic sign inventory using image processing is presented in Chapter 3. The methodology for an automatic traffic sign retroreflectivity condition

assessment using computer vision and mobile LiDAR technologies is presented in Chapter 4. The experimental tests for validating the methodologies for traffic sign inventory and retroreflectivity condition assessment are presented in Chapter 5. Finally, the contributions and findings of this study and recommendations for a future research are summarized in Chapter 6.

CHAPTER 2

LITERATURE REVIEW

Traffic signs are the traffic control devices erected on public roads to provide critical information for road users, including notification of regulations, warning of hazards on or near the roadway, and guidance for destinations. The Manual on Uniform Traffic Control Devices (MUTCD) developed by Federal Highway Administration (FHWA) requires all transportation agencies to adopt a sign management and maintenance program to promote the functionality and efficiency of traffic signs (FHWA, 2009). Traffic sign inventory and traffic sign retroreflectivity condition assessments are the two indispensable components of a traffic sign management and maintenance program. Traffic sign inventory collects the locations and attributes of each individual traffic sign, while retroreflectivity condition assessment determines the performance adequacy of the inventoried signs by assessing their retroreflectivity. This chapter reviews manual and automatic traffic sign inventory and retroreflectivity condition assessment methods and the practices adopted by transportation agencies. In addition, this chapter identifies the challenges and research needs in the current manual and automatic methods.

2.1. Traffic Sign Inventory

A traffic sign inventory is a data collection process obtaining essential traffic sign information, e.g. traffic sign location, type, etc. The data is used by transportation agencies to manage their invested assets. This section reviews manual and automatic traffic sign inventory technologies and the practices adopted by different transportation agencies.

2.1.1. Traffic Sign Inventory Data Collection

The objective of traffic sign inventory for transportation agencies is to identify the locations of their invested assets by constructing a geo-referenced inventory database. The inventory database will be used for estimating sign life, managing and prioritizing maintenance activities, and budgeting and minimizing tort liability. To fulfill the objective of the traffic sign inventory, two key data items, the location and the MUTCD code, are included in all traffic sign inventory programs (McGee, 2010); some other auxiliary data items, such as sign support type, sign offset, etc., are also collected. Both manual method and video logging method are used by transportation agencies to collect these inventory data items.

2.1.1.1. Manual Method

Many transportation agencies use manual methods for traffic sign inventory data collection because it is easy to implement and relatively inexpensive. The manual data collection method requires that field engineers physically approach each traffic sign and collect the necessary data. The field engineers use paper-based spreadsheets to input the data (Larson & Skrypczuk, 2004). With the development of portable devices and GPS technologies in recent years, many agencies have started to use GPS-equipped handheld computers to accelerate the data collection process (Paoly & Staud, 2010; Rasdorf, et al., 2009).

Although the applications of the information technology improve the data collection efficiency, the manual method is still labor-intensive, dangerous, and time-consuming because the manual method still requires field engineers to physically approach traffic signs to collect data. Many traffic signs are difficult and dangerous to approach, such as median signs, overhead signs, etc. In addition, the discrete distribution of traffic signs along roads needs much traveling and frequent stops between different

signs, which costs transportation agencies much in terms of resources and effort (Wolshon, 2003).

2.1.1.2. Video-logging Method

To improve the data collection efficiency and safety, many transportation agencies and vendors use video-logging methods to collect traffic sign inventory data. Video log images are first collected by using a data collection vehicle at highway speed. The collected data is then transferred to the office and manually processed by the operators who perform a frame-by-frame review, manually extract traffic sign information, and input the sign attributes into a data system.

Many transportation agencies, including almost all the state departments of transportation (DOTs), are equipped with a mobile data collection system (Findley, et al., 2011), and they collect video log image data for roadway visualization purposes periodically (PennDOT, 2010). Nevertheless, there are only a limited number of transportation agencies that use these data for traffic sign inventory because the image reviewing process is time-consuming and tedious. The North Carolina Department of Transportation (NCDOT) only uses the video-logging method to inventory overhead signs (2011). The city of Phoenix, Arizona, uses a similar method to inventory the 28,000 traffic signs in the city area (Moreno & Cook, 2010). There are also several contracting vendors using such methods to help large transportation agencies inventory their traffic signs, e.g. Trimble® Geo-3D, Roadware®, Mandli®, etc. Although some data-reviewing software has been developed to facilitate the process, manual review of the collected video log images frame by frame is still required. In 2010, Roadware conducted an internal study on the efficiency of traffic sign inventory using the video-logging method; the result implied that the processing rate is approximately 10 traffic signs per hour (Dew, 2010). It is identified that although video log image data are widely available in many transportation agencies, manually reviewing the images and inputting attribute data

are so labor-intensive and time-consuming that they hinder the full utilization of these data for traffic sign inventory. There is a need for an automatic method to process video log images in support of traffic sign inventory efficiently.

2.1.2. Image-based Traffic Sign Detection Methods

To fully utilize the widely available video log images and to improve the efficiency of the traffic sign inventory process, some automatic methods have been developed using video log images in recent studies. These automatic methods attempt to reduce the effort of manual review. Based on a thorough literature review, the majority of the studies using this approach set the inventory problem into two stages: detection and recognition. The traffic sign detection stage serves as a filter to eliminate the majority of the video log images that do not contain traffic signs and to extract the regions of interest (ROIs) within the video log images in which traffic signs may exist; the traffic sign recognition stage serves as a classifier to validate whether or not the extracted ROIs contains a sign and to associate them with the MUTCD code if a sign is present.

It is identified that traffic sign detection is the most critical and challenging stage. Unreliable detection results could lead to excessive errors in subsequent stages of recognition. Developing a robust sign detection algorithm using video log images contains such technical challenges as light condition changes, noise introduced by the camera, and complicated image contexts (e.g. cluttered backgrounds, occlusions, etc.) within a natural environment. In addition, because there are more than 670 types of traffic signs defined in the MUTCD, it is even more challenging to design a reliable traffic sign detection algorithm for all the MUTCD specified signs. Therefore, this dissertation focuses on image-based traffic sign detection, while traffic sign recognition is recommended for future research.

From the literature, it is identified that most of the existing image-based traffic sign detection algorithms have been developed following a two-stage approach using the

two distinct traffic sign features defined in the MUTCD, color and shape. In these algorithms, color segmentation is first applied to video log images to segment different color clusters, and then shape detection is employed to extract the traffic sign candidates (i.e. ROIs) from the segmentation results.

2.1.2.1. Color Segmentation

Color segmentation is a process of partitioning the collected video log images into different segments which contain different colors. The unique traffic sign colors are used to differentiate potential traffic signs from the background objects within video log images. General color segmentation techniques for an object detection problem attempt to find an optimal boundary in the defined color space that can accurately cluster the pixels that belong to the same color. Traffic sign color segmentation follows the same principle. However, two unique challenges need to be addressed specifically for traffic sign detection: 1) there are ten colors specified in the MUTCD that should be distinguished from the background rather than a single color; 2) there is a discrepancy between the MUTCD defined sign colors and the actual colors in the video log images due to the change of illumination, the noise introduced by the camera, or the deterioration of signs. To address these unique challenges, previous studies have been carried out, focusing on the selection of color spaces and the methods for color classification.

2.1.2.1.1. Color Space Selection

RGB/nRGB Color Space: Red, green, and blue (RGB) color space is one of the most basic color spaces used in a camera and monitor system. Therefore, it is the simplest color space for segmentation without need for transformation. Therefore, many studies have employed RGB color space for traffic sign detection (Benallal & Meunier, 2003; Wu & Tsai, 2006). However, due to the high correlation among the three color components, the segmentation results are typically not robust to illumination changes. In

order to improve the performance, normalized RGB (nRGB) color space was introduced by Janssen et al. (1993) and Kamada et al. (1990). The original RGB values are normalized by the summation of RGB values (i.e., intensity) so that illumination changes have less effect on RGB color. Although RGB/nRGB color space is simple to implement, each color component (i.e. R, G or B) is still lighting-condition dependent.

HSV Color Space: Hue, saturation, and value (HSV) is a color space that is defined as being similar to what the human eye perceives (Berk, et al., 1982). Hue represents the perceived color information, and saturation represents the purity of the perceived color. Value represents the brightness of the perceived color. By isolating the color information from the brightness, such color space is more immune to the lighting condition changes in the video log images. Many studies have employed HSV color space for traffic sign detection with reasonably good segmentation results (de la Escalera et al., 2003; de la Escalera et al., 2004; Maldonado-Bascon et al., 2007).

Other Color Spaces: Other color spaces, including YUV, L*u*v*, Ohta, etc., have also been attempted in processing video log images for traffic sign detection. YUV is a color space that is defined as being similar to how a television system displays the image. The brightness component (Y) and the chromatic components (UV) are completely separated. The chromatic components only rely on the R and B components in the RGB color space, while the Y component is a weighted average of all the RGB values. L*u*v* is a color space that is defined by international commission on illumination (CIE) by reserving the simplicity of the legacy CIE XYZ color space while attempting perceptual uniformity. L*u*v* values are computed with a non-linear transformation from the XYZ values. There have been several attempts to use these color spaces in previous studies (Kang et al., 1994; Miura et al., 2000). Ohta et al. (1980) proposed a new Ohta space that demonstrates some true beneficial characteristics in processing video log images. The Ohta color space is derived from attempting to find the best uncorrelated color components. Therefore, each color component can be

independently processed. The transformation matrix is derived by Ohta et al. (1980) based on extensive experiments and the Karhunen-Loeve transform. However, due to the limited physical correlation between the color components in these color spaces and the video log image color features, the attempts were not extensively carried on in processing video log images.

From the literature review of different color spaces, there is no single color space that can robustly work for all video log images in different contexts and lighting conditions. Among all of other color spaces, HSV color space is the most accepted color space for image processing in natural settings. The isolation of the color and illumination information into different components minimizes the impact of the change of lighting conditions in video log images with natural scene settings. The further isolation of the chromatic information into two individual components, i.e. H and S, ten MUTCD defined colors can be distinctively separated with limited confusion (Tsai et al., 2009). However, the HSV color space has one drawback: color information in the hue component becomes unreliable for achromatic pixels, especially when the image is really bright (e.g. over-exposure) or dark (e.g. under-exposure) where the RGB values of the pixel are too close (Maldonado-Bascon et al., 2007).

2.1.2.1.2. Color Classification

Color classification groups pixels with similar color features into the same cluster. As a general color classification problem, many classical methods have been studied, such as connected component analysis (Khan et al., 2011; Marinas et al., 2011), the Gaussian and Gaussian mixture model (GMM) (Ruta et al., 2010), etc. To deal specifically with traffic sign color classification problems, two popular groups of methods, thresholding, neural network (NN) and support vector machine (SVM), focusing on processing speed and robustness, have been used. In addition,

chromatic/achromatic decomposition (CAD) has been introduced to be used individually or to complement other methods for white and black color classification.

Thresholding Method

Color classification uses thresholding to find a set of optimal values that can effectively threshold the components in a selected color space. Most of the threshold values are empirically established by selecting the traffic sign image samples with different colors. By analyzing the distribution (Maldonado-Bascon et al., 2007) or histogram (de la Escalera et al., 2003) of the selected samples, the best thresholding values are empirically selected for each color. To ease the process for empirical threshold value selection, color spaces that contain uncorrelated components are commonly used, e.g. HSV, Ohta, etc. Although the thresholding method is easy to implement with a fast processing speed, it has two drawbacks: 1) there are a large number of threshold values to be adjusted, especially when the number of color classes are large; 2) the effectiveness of the color classification dramatically depends on the generality of the traffic sign samples used for determining threshold values.

Neural Network and Support Vector Machine Method

To obtain a good generalization for color classification and reduce the need for empirical threshold value adjustment, color classification methods using NN and SVM have been introduced. Both NN and SVM-based approaches follow a training-validation process, which requires a training dataset to establish the classifier, i.e. a neural network and support vectors, respectively. The established classifier is used to achieve the classification job.

NN was introduced first and received considerable attention. In most of the NN formation, the input is typically the value of each component in the selected color space, while the output is the labeling indicating different traffic sign color. Nguwi and Kouzani (2008) segmented the input image in the HSV color space and located traffic signs. The classification module determined the type of detected traffic signs using a series of one-

to-one architectural multilayer perceptron neural network. Tsai et al. (2009) input the HSV component values and an additional 157 non-linear compound components to formulate a function linked network (FLN) to classify ten MUTCD colors. Fang et al. (2003) proposed spatial neural network to classify seven different colors based on only the hue value and spatial adjacency of the values. Although NN demonstrated good color classification capability with good generalization, the structure of the hidden layer can only be arbitrarily designed with empirical experience, the network weights are hard to correlate with physical meanings of the input or output, and the network could have multiple solutions associated with local minima (Vemuri, 1993).

To improve the performance of NN, SVM is more popularly used in color classification and many other classification problems. SVM deploys the simple concept of maximizing classification boundary in a linear setup. Then it introduces the concept of kernel functions so that a non-linear classification problem is transformed into linear classification problem in a higher dimension. Eventually, by solving a quadratic programming optimization problem, the optimal classification boundary is identified (Cortes & Vapnik, 1995). With such formation, SVM demonstrates better generalization and optimal solution convergence than NN. However, due to the nature of SVM, SVM is only capable of classifying two classes, which is not feasible for traffic sign color. Therefore, multi-class SVM has been introduced and used in multiple color classification by introducing one-over-all or pair-wise strategy. Maldonado-Bascon et al (2007) formulated the SVM using one-over-all strategy to classify different traffic sign colors using RGB color space.

The previous studies show many studies have been carried out for traffic sign color segmentation. HSV color space and NN- or SVM-based color classification are among the most popular methods to achieve reasonably good color segmentation results. However, due to the complication of the natural scene video log image, especially the variant lighting condition changes, there is no universal method that can robustly segment

all the MUTCD colors. One possible direction to further improve the performance of color segmentation is to adapt the existing color segmentation methods to the natural variant lighting conditions.

2.1.2.2. Shape Detection

Shape detection is a process of identifying unique geometrical shapes as defined in the MUTCD. These unique shapes can be used to detect traffic signs from the segmented images. After the color segmentation, the video log images are segmented based on different color clusters, represented by the boundary contours or image blobs. Shape detection methods are proposed to analyze the geometry information of contours or blobs. Three primary challenges include: 1) there are ten types of traffic sign shapes defined in the MUTCD; 2) the segmented contour or image blob may contain defects compared with the original shape due to color segmentation error. For example, a straight line could be curved, a small corner could be missed in a square shape, etc.; 3) the perspective view of the video log camera distorts the geometrical shape of the traffic sign. For example, parallel lines in a rectangular traffic sign are not long parallel. In previous studies, element-based methods and pattern-based methods have been developed to address the identified challenges.

2.1.2.2.1. Element-Based Method

An element-based method detects a traffic sign by identifying fundamental sign elements from color segmented images, i.e. corner, edge, etc. The identified elements are further assembled into detected traffic sign candidates. Most of the element-based methods are used when the color-segmented results are represented as contours.
De la Escalera et al. (1997) used different pre-defined masks to identify the corner points, and then used the triangular and rectangular constraint to identify the detected corner points as the vertexes of different shapes. Haritaoglu (2003) applied two effective

enhancement methods, including a symmetric neighborhood filter (SNF) to retain the edge and hierarchical connected component (HCC) analysis to identify the traffic sign region, and then the corner points of the traffic sign could be revealed. Garcia et al. (2003) used the horizontal and vertical gradient of the image to extract the traffic sign edges in the images, followed by the two directional projections to extract the shape of the traffic sign region. There are several other methods that are applied to identify the edges of traffic signs, such as Harris corner detection (Paulo & Correia, 2007), radial and circular edge detections (Sandoval, et al., 2000), etc. The element-based methods are robust to the defects from color segmentation because only local element-based features are extracted. However, assembling the extracted elements is not an easy task. It requires a priori elimination of the false assembling of the extracted elements. Blancard (1992) defined a group of a priori knowledge that is essential for assembling the extracted elements, including perimeter (number of pixels), outside bounding box, center of gravity, aspect ratio, freeman code, etc. Piccioli et al. (1994) concentrated exclusively on the geometry reasoning for assembling the extracted elements to formulate different traffic sign shapes. Escalera et al. (1997) formulated a composite energy function using the fundamental elements of a traffic sign, including gradient, sign distance, sign geometry, etc. Detection is achieved by minimizing the formulated energy using a genetic algorithm (GA).

2.1.2.2.2. Pattern-Based Method

A pattern-based method detects the overall patterns of traffic sign shapes instead of the individual element to improve the algorithm's robustness. Most of the element-based methods are used when the color segmented results are represented as blobs. Maldonado-Bascon et al. (2007) proposed a distance-to-boundary (DtB) pattern for traffic signs so the rotations of the traffic sign in natural scenes are addressed. By plotting the DtB in 1-D, the traffic sign shape can be classified based on the sudden change of

DtB values where there is vertex. The DtB pattern is further generalized using the SVM-based classification method. Parada-Loira and Alba-Castro (2010) proposed the local contour pattern (LCP), derived from a local binary pattern (LBP), and applied the pattern to the texture area for detecting areas with unique shapes. For traffic signs, only the LCP code-word representing linear structures with selected angles are kept for detection. However, the DtB method and the LCP method require "perfect" extraction results from the color segmentation step. Otherwise, the defined patterns cannot be reliably recognized. Haar-like patterns that are originally proposed for face detection were, also, introduced for traffic sign detection (Bahlmann, et al., 2005). However, the Haar-like patterns are very hard to be generalized when defining different types of traffic signs (Hu & Tsai, 2011).

Through the review of previous studies, it is identified that neither the edge-based nor pattern-based method pose a reliable solution for robust shape extraction due to the complications of the cluttered background captured in the video log image and imperfect color segmentation results. For the edge-based method, it is challenging to effectively assemble the extracted unorganized elements. For the pattern-based method, it is challenging to provide perfect blobs from color segmentation for the algorithm to recognize the shape pattern reliably. One way to improve the performance of shape detection might be to combine the edge-based method and pattern-based method by retaining the capabilities to reliably extract individual sign elements and maintain the integrity of sign shape features from both methods, respectively.

2.1.2.3. Generalized Image-Based Traffic Sign Detection

Despite the fact that researchers have made numerous efforts to implement an automatic traffic sign detection algorithm for transportation agencies using video log images, implementing an effective algorithm still remains a challenge. This hinders the use of widely available video log images. Most of the existing traffic sign detection

methods have only focused on certain types of traffic signs, which are primarily designed for driver support systems (DSS) and focus only on safety-related traffic signs, e.g. regulatory signs, etc. Many of the methods are implemented in high-class vehicles or new anonymous vehicles, e.g. Google driverless car. For example, the traffic sign recognition (TSR) module is found on Volkswagen and Audi cars for speed limit signs and no-parking signs (Volkswagen, 2010), while similar technology is used on BMW cars for speed limit sign recognition (BMW, 2012). For the new Google driverless car (Guizzo, 2011), although light detection and ranging (LiDAR) is used as the primary object detection sensor, image-based TSR is still used for detecting and recognizing certain types of traffic signs, e.g. stop sign, speed limit sign, etc., that might impact the behavior of the vehicle. Although many of these methods can achieve very good detection accuracy, i.e. more than 95% for speed limit sign detection (Wei et al., 2011), and have been commercially available, these methods cannot be practically used for traffic sign inventory purposes because they do not work for all types of traffic sign types. A generalized traffic sign detection method is hard to find in the literature. De la Escalera et al. (1997, 2003, 2004) and Gil-Jiménez et al. (2005, 2007, 2007) both developed a generalized traffic sign detection method using pictograms and a priori knowledge of the shapes and colors of traffic signs was proposed for the European traffic sign system. The algorithms developed by de la Escalera et al. achieved a detection rate of 90.4% (true positive rate) and approx. 30% (false positive rate) using 83 tested traffic signs. Gil-Jiménez et al. achieved a detection rate of 93.24% (true positive rate) and 21.2% (false positive rate) using 5,176 video log images collected by the research team in Spain. However, both algorithms only detect a small number of sign types and colors (only red circles, blue circles, and blue rectangles).

The algorithm developed by Tsai et al. (2009) is the first and only attempt identified in the literature review to detect all types of traffic signs defined in the MUTCD. The algorithm was developed using an NN-based color segmentation model

and a Douglas-Parker (DP)-based shape approximation method. The algorithm was validated using 37,640 video log images collected by the Louisiana Department of Transportation and Development (LaDOTD) and achieved a detection rate of 83.7% (true positive rate) and 12.9% (false positive rate).

To obtain a better understanding of the algorithm's performance, a critical assessment was conducted using the actual video log images collected in Nashville, Tennessee, by Georgia Tech's sensing vehicle. The algorithm developed by Tsai et al. was tested. From the results of the assessment, the following issues were identified (detailed assessment results can be found in the Appendix):

- Variant lighting condition: The appearance of the colors of traffic signs within video log images can be severely distorted due to the varying illumination captured by video log images. In addition, colors of traffic signs can also be distorted non-homogeneously by shadows cast from surrounding objects (Garcia-Garrido et al., 2006; Huang et al., 2010).
- Cluttered background: Both colors and boundaries of signs captured in video log images can be confused with cluttered backgrounds that contain similar colors (e.g. green vegetation and green information signs, etc.) and/or shape patterns (e.g. house windows and rectangular signs, etc.) (Lowe, 1999; Piccioli et al., 1996; Ruta, et al., 2008).
- Occlusion: Trees, poles, buildings, vehicles, and pedestrians captured by video log images frequently occlude traffic signs due to the camera view angle. Occlusions can break the integrity of shape patterns or boundaries captured by video log images (de la Escalera et al., 2003, 2004; Khan, et al., 2009; Maldonado-Bascon et al., 2007; Paclik, et al., 2006).
- Physical condition change: Traffic signs with poor physical conditions, such as sheeting deterioration, vandalism, tilting, etc., do not share colors and/or shape features in common with signs in good condition (Tsai et al., 2010).

- Video log image quality: Because of the vibrations of a moving vehicle, camera malfunctions, and /or lens debris, many video log images are captured with poor quality. These images may not be usable for automatic sign detection (Sheikh & Bovik, 2005; Tsai & Huang, 2010).

Among all the identified issues from the assessment, varying lighting conditions and cluttered backgrounds contribute more than half of the identified false negative cases. Therefore, these two key issues are identified for enhancement as the focus of this dissertation.

2.1.2.4. Discussion

Through the literature review of image-based traffic sign detection methods and the corresponding assessment (presented in the Appendix), challenges and research needs are identified primarily on the algorithm development level. Although there are many image-based traffic sign detection algorithms, to develop a reliable and generalized image-based traffic sign detection algorithm that is capable of accurately detecting more than the 670 types of signs specified in the MUTCD still remains a challenge. Several key technical challenges are identified in the literature and the assessment of the selected algorithm, including variant lighting conditions, cluttered backgrounds, occlusions, physical condition changes, poor image quality, etc. This dissertation focuses on enhancing the image-based traffic sign detection algorithm by addressing the light condition challenge and the cluttered background challenge.

2.2. Traffic Sign Retroreflectivity Condition Assessment

Traffic sign condition assessment is used to determine the performance adequacy of the traffic signs so that transportation agencies can determine the signs that need to be maintained or replaced. Failed traffic signs are indicated by insufficient retroreflectivity and/or visual defects that obscure the displayed information of the traffic sign (Howe,

2006). A reliable and effective traffic sign condition assessment method is needed to enable transportation agencies to determine the adequate timing for traffic sign maintenance and replacement. As FHWA has proposed the minimum traffic sign retroreflectivity conditions and mandated that transportation agencies plan and implement procedures to maintain minimum traffic sign retroreflectivity, the need for a reliable and effective retroreflectivity condition assessment method is urgent. This dissertation focuses on traffic sign retroreflectivity condition assessment to meet the urgent need of transportation agencies. Other visual defects will be recommended for future research.

2.2.1. Traffic Sign Retroreflectivity Condition Data Collection

Traffic signs are designed to be reflective during the nighttime under the illumination of vehicles' headlights so that drivers can read the vital information without other external lighting. To serve such a purpose, special sheeting materials with "retro"-reflective feature are used for traffic signs so that light can be reflected back to its original source and perceived effectively by drivers' eyes. The objective of traffic sign retroreflectivity condition assessment is to evaluate the retro-reflective capability of traffic signs in support of traffic sign replacement or maintenance. "*Highway statistics nationwide reveal that the nighttime fatal crash rate is approximately three times that of the daytime crash rate, measured in million miles traveled*" (Carlson & Picha, 2009). Every transportation agency responsible for maintaining public highways and streets is required to use retro-reflective materials on traffic control devices to facilitate driver safety. Traffic sign retroreflectivity condition is determined using nighttime visual inspection by using retroreflectometer measurement or a management method. The following introduces the existing traffic sign retroreflectivity condition determination methods.

- Nighttime visual inspection. Nighttime visual inspection is a manual process that requires an investigator to drive a sport utility vehicle (SUV)-type vehicle during the

nighttime and visually assess the traffic sign retroreflectivity condition using “trained eyes” (FHWA, 2009). As it is easy to conduct, most transportation agencies use nighttime visual inspection as the primary method to determine the traffic sign retroreflectivity condition. For example, the Georgia Department of Transportation (GDOT) annually conducts retroreflectivity condition assessment using this method. Although the nighttime visual inspection is widely used by state DOTs, the assessment results are subjective and inconsistent from one investigator to another. Hawkins and Carlson conducted a field test using 50 traffic signs removed from the roadside. Sign investigators in the test identified 26 unacceptable signs, while only one traffic sign was considered unacceptable using a retroreflectometer following FHWA's standard (2001).

- Retroreflectometer measurement. Retroreflectometer measurement is a manual process that requires the investigator to conduct contact measurements for each traffic sign using a retroreflectometer. The American Society for Testing and Materials (ASTM) has provided a standard measurement procedure using the retroreflectometer, which mimics the traffic sign brightness as seen by an SUV driver at a distance of 200 m distance. An average or median of four measurements for each reflective color of the traffic sign are required. The average of the readings for each reflective color will be compared with the MUTCD standard to determine the sign's retroreflectivity condition (ASTM, 2009). The retroreflectometer can provide a quantitative and consistent measurement to determine the traffic sign's retroreflectivity for each measurement point. Several transportation agencies are using this method, including LaDOTD, the Indiana Department of Transportation (InDOT), the Virginia Department of Transportation (VDOT), Hillsborough County, Florida, etc. However, as the retroreflectometer measures the traffic sign retroreflectivity by contacting the traffic sign surface, the investigator needs to physically approach each traffic sign and conduct the survey, which is time-

consuming, costly, and sometimes dangerous. In addition, as the average of the selected measurements is used to represent the overall retroreflectivity condition for each reflective color, the results can be over or under-estimated if the traffic sign is non-uniformly deteriorated (Remias et al., 2011).

- Management method. The management method is a management process that predicts how long signs with similar characteristics, e.g. installation date, sign sheeting, and color, etc., will maintain an above-standard retroreflectivity. The expected sign life method, the blanket replacement method, and the control sign methods are included under the management method.
    - The expected sign life method calculates a sign's life from known sign retroreflectivity deterioration rates for combinations of sign sheeting color and sheeting type. The Michigan DOT uses expected sign life based on retroreflectivity deterioration research to determine when a sign should be replaced (Cambridge Systematics Inc. & Meyer, 2007).
    - The blanket replacement method replaces all signs along a corridor, within an area, or of the same sign and sheeting type at intervals based on the expected sign life of the signs. The city of Phoenix is performing the blanket replacement method to replace more than 28,000 traffic sign along the major corridor in the city (Moreno & Cook, 2010).
    - The control sign method uses signs either in a controlled study yard or a sample of signs from the field to determine sign life.

Although no individual retroreflectivity condition assessment is needed using management methods, there are potential issues for blindly replacing traffic signs in a region based on the limited criteria. On one hand, these management methods could potentially replace many traffic signs with good retroreflectivity condition, which is a waste of investment. On the other hand, these management methods could overlook some

critical traffic sign with a poor retroreflectivity condition while the majority of the signs in the region are still in good condition, which introduces potential liability concerns. The current practices in transportation agencies are primarily manual methods, either nighttime visual inspection or retroreflectometer measurement. These methods require individual assessment for each traffic sign, which is time-consuming and costly. In addition, the assessment result can be subjective and inconsistent (using the nighttime inspection method) or inaccurate (using the retroreflectometer measurement method). Management methods are also used by transportation agencies to save time and cost. However, blind replacement of traffic signs with good retroreflectivity condition leads to a waste of investment. Therefore, transportation agencies are in urgent need of a reliable and cost-effective traffic sign retroreflectivity condition assessment method to meet FHWA's requirements and their own management needs.

2.2.2. Traffic Sign Retroreflectivity Condition Assessment Methods

To reliably and cost-effectively collect traffic sign retroreflectivity condition information, previous research has attempted to develop automatic assessment methods. The image-based method is the most commonly used sign retroreflectivity condition assessment method. The key principle of this kind of methods is establishing the correlation between image intensity and traffic sign retroreflectivity. Nevertheless, there are very few systematic studies exploring such correlation. Most of the studies are based on the empirical results established using limited traffic sign samples. Siegmann et al. (2008) systematically developed the fundaments between image intensity and retroreflectivity from a photometrical perspective. Different factors, including the camera aperture number, the camera exposure time, the surface element and color, the distance from the light source to the surface and the incident angle, etc., were studied. A close form equation between retroreflectivity and the studied factors was derived. The equation was validated using a circular speed limit sign. This equation can be applied to

correlation of the image intensity and the retroreflectivity under different camera configurations, e.g. the camera exposure time, the camera aperture, etc., and different data collection parameters, e.g. distance, incidence angle, etc.

Using correlations established between the image intensity and the retroreflectivity, several image-based traffic sign retroreflectivity condition assessment systems have been developed. The Sign Management and Retroreflectivity Tracking System (SMARTS) van was first developed by FHWA in 1999. The pilot test was conducted by Alaska DOT (Smith & Fletcher, 2001). An external light-emitting diode (LED) was used to provide lighting to the traffic sign with known luminance to mimic a vehicle's headlight, while a single camera was used to collect video log images for the illuminate d traffic signs. However, the results from the SMARTS van demonstrated poor correlations with the retroreflectometer. Facet Inc. and Mandli® Communications Inc. developed a similar system called RetroView. Two-camera systems were used that were dedicated to collecting low and high levels of intensity separately (Retterath & Laumeyer, 2008, 2011). Several pilot tests have been conducted by the Tennessee Department of Transportation (TDOT) and the Texas Department of Transportation (TxDOT) using the RetroView system; the results indicate that the system is potentially a cost-effective method for traffic sign condition assessment. In Europe, the VISUAL Inspection of the Sign and panEL (VISUALISE) system was developed by Gonzales, et al. (2011). The VISUALISE system was tested on 500 traffic signs in Spain, and 91% of the traffic signs were correctly assessed. To avoid ambient lighting, the system can only be operated during the nighttime.

In summary, in previous studies, there have been a few attempts to develop an automatic image-based traffic sign retroreflectivity condition assessment method. Although some prototype systems have been developed, two challenges that hinder their implementation in DOTs' practices remain: 1) the existing system can only operate during nighttime to minimize the impact of ambient lighting and get reliable traffic sign

retroreflectivity condition results; 2) there are very limited validations that have been conducted for these systems to demonstrate the feasibility for implementation. Based on a nationwide survey of different vendors providing comprehensive roadway appurtenance acquisition (Findley, et al., 2011), no vendors in the current market provide any data or services for traffic sign retroreflectivity condition assessment. At present, none of the state DOTs have adopted any of these systems for traffic sign retroreflectivity condition assessment.

2.2.3. Discussion

The literature review shows that transportation agencies currently use, primarily, manual methods for traffic sign retroreflectivity condition assessment. These methods can be subjective and inconsistent when using nighttime inspection or time-consuming when using retroreflectometer measurement. Some management methods are also used by transportation agencies. Although the cost for the assessment of each individual traffic sign can be saved, such methods may replace a good percentage of traffic signs with good condition, which is potentially wasteful, or overlook some critical traffic signs with poor condition, which causes potential liability concerns. There are only a few studies on developing automatic traffic sign retroreflectivity condition assessment methods. The most commonly used methods are image-based methods that depend on the correlation between image intensity and traffic sign retroreflectivity. All of these systems can only operate during the nighttime to obtain reliable condition assessment results, and yet none of these methods have been validated or adopted by any state DOT. There is a need to explore an alternative automatic method to assess traffic sign retroreflectivity condition reliably and cost-effectively.

2.3. Summary

The following summarizes the finding from the literature review and the identified research needs:

- Video log images are widely available for different state DOTs. However, frame-by-frame reviewing of collected signs is labor-intensive and time-consuming. Although many image-based traffic sign detection algorithms have been developed, it still remains a challenge to automatically extract all types of traffic signs specified in the MUTCD from video log images because of two key challenges: 1) variant lighting conditions that distort the appearance of colors of signs within images; 2) cluttered backgrounds that confuse both the color and boundary of traffic signs with non-sign objects by adding additional false edges and interrupting the traffic sign boundaries. There is a need to develop an enhanced automatic traffic sign detection methodology to address these key challenges.
- Three traffic sign retroreflectivity condition assessment methods are currently used by transportation agencies. However, these methods can be subjective and inconsistent (using nighttime inspection method), time-consuming (using retroreflectivity measurement method), or potentially wasteful/liable (using management methods). Although several image-based automatic methods have been developed, none of them have been validated or adopted by state DOTs. There is a need to explore the feasibility of developing an automatic traffic sign retroreflectivity condition assessment methodology, e.g. using the retro-intensity values from a mobile light detection and ranging (LiDAR).

CHAPTER 3

AN ENHANCED GENERALIZED IMAGE-BASED TRAFFIC SIGN DETECITON METHODOLOGY

3.1. Objective

The objective of this chapter is to propose an enhanced image-based generalized traffic sign detection methodology to address the two challenges identified in the literature review in Chapter 2 and the critical assessment in the Appendix: 1) variant lighting conditions that distort the appearance of colors of signs within images, and 2) cluttered backgrounds that confuse both the color and boundary of traffic signs with non-sign objects. First, a lighting-dependent statistical color model (LD-SCM) -based color segmentation algorithm is proposed that is robust to different image lighting conditions, especially adverse lighting. Second, an ordinary/ partial differential equation (ODE/PDE)-based shape detection algorithm is proposed that is immune to the discontinuous sign boundaries in the cluttered background.

3.2. Proposed Methodology

The existing traffic sign detection methodology is proposed based on the fundamental features of traffic signs defined in the Manual on Uniform Traffic Control Devices (MUTCD) and consisting of three key steps: 1) color segmentation, 2) shape detection, and 3) post validation (Tsai et al., 2009). The color segmentation step is to conduct pixel-wise color classification on the video log image. The shape detection step is to conduct the polygon detection and approximation using the extracted image edge and contours. The post validation step is to conduct the verification of each of the detected sign candidates using traffic sign geometry and color constraints. Tsai et al. (2009) have established a good framework for developing a generalized traffic sign

detection algorithm. The proposed, enhanced methodology is based on the previous framework. Figure 3-1 shows the complete flow of the enhanced automatic traffic sign detection method based on the existing framework, where the highlighted steps are the enhanced algorithms that are proposed in this study. The LD-SCM-based color segmentation algorithm is proposed to enhance the performance in the color segmentation step, and the ODE/PDE-based shape detection algorithm is proposed to enhance the performance in the shape detection step. The algorithms are seamlessly integrated into the existing framework to form a new enhanced traffic sign detection methodology.

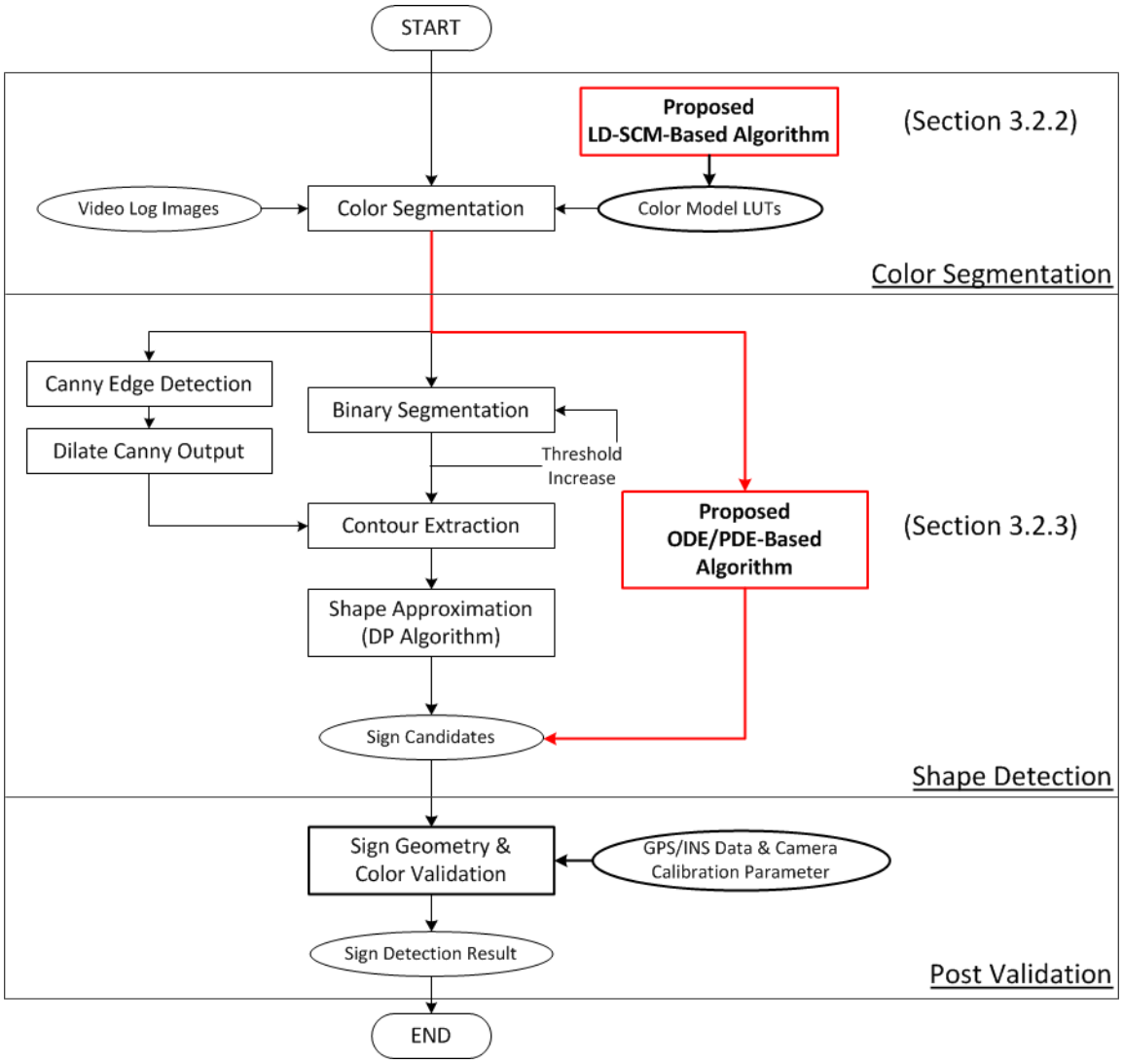

Figure 3-1 Flowchart of the enhanced image-based generalized traffic sign detection method

3.2.1. LD-SCM-Based Color Segmentation Algorithm

Variant lighting conditions are common in video log images because the data collection vehicle collects video log images under varying weather conditions, in varying driving directions, at varying times of the day, and using varying camera configurations. Figure 3-2 shows the four typical lighting conditions that are captured in video log images, including (a) over-exposure, (b) normal, (c) under-exposure and (d) adverse lighting. These lighting conditions can significantly distort the representation of the colors captured in video log images. In this section, an image lighting condition classification model is first proposed to identify the four typical lighting conditions, including the challenging adverse lighting conditions. A series of SCMs under different lighting conditions is established using local homogeneity features, and artificial neural networks (ANN) are then formulated. By selecting the corresponding SCMs for video log images under different lighting conditions, the images can be reliably segmented into different MUTCD colors to support the subsequent shape detection step.

(a) Over-Exposure **(b) Normal**

(c) Under-Exposure **(d) Adverse Lighting**

Figure 3-2 Examples of the video log images under different lighting conditions

Figure 3-3 shows the detailed flow of the proposed LD-SCM-based color segmentation algorithm. The input video log image $I_0(x, y)$ is first analyzed to be classified into one of the four lighting conditions *i* using the developed image lighting condition model. The output lighting condition associated video log image $I_0(i, x, y)$ is then input into the LD-SCM-based color segmentation. The corresponding look-up table of the LD-SCM, i.e. *LUT(i)*, is selected for this segmentation. Especially if the lighting condition of the image is identified as an adverse lighting condition, an adaptive thresholding method is applied to the image to identify the adverse lighting region $R^-(i, x, y)$ and non-adverse lighting region $R^+(i, x, y)$, where two LD-SCM LUTs, i.e. *LUT(i)* and *LUT(j)*, are applied for segmentation. Typically, the LUT associated with the over-exposure lighting condition is applied to the non-adverse lighting region, while the LUT associated with the under-exposure lighting condition is applied to the adverse lighting region. After the color segmentation, the segmented images will be input into the subsequent shape detection step. In the following three sub-sections, the formulation of the image lighting condition model, the formulation of the LD-SCM color model, and the adaptive thresholding method are presented in details.

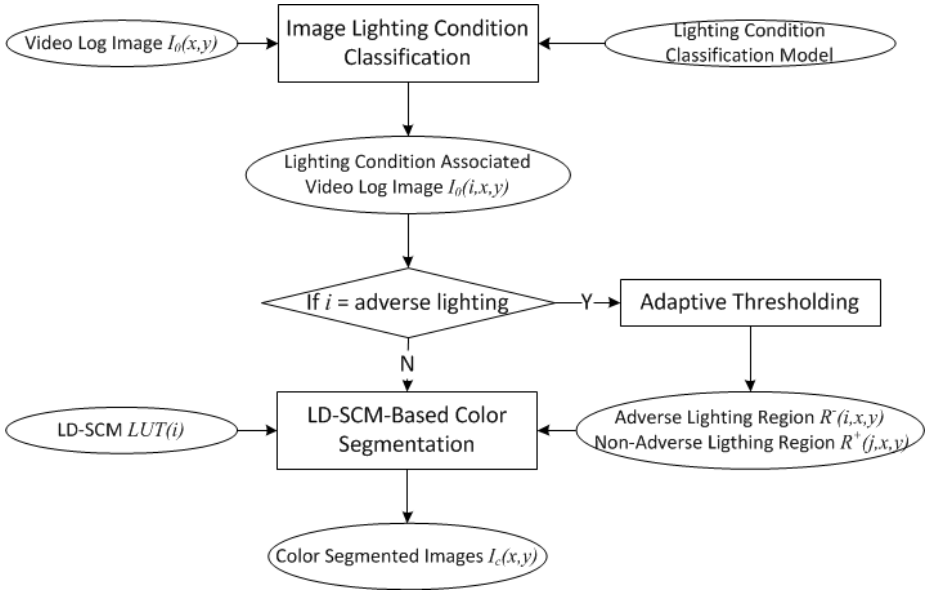

Figure 3-3 Flowchart of the proposed LD-SCM-based color segmentation algorithm

3.2.1.1. Image Lighting Condition Modeling

Four types of lighting conditions identified in video log images by Tsai and Huang (2010) are modeled in this study. They include: 1) over-exposure condition, 2) under-exposure condition, 3) normal lighting condition and 4) adverse-lighting. Figure 3-2 shows the examples of four different lighting conditions.

a) An over-exposure condition is a scene in which light sources are so strong that most of the pixels in the image are over-saturated with a general high intensity value. In such cases, most of the colors are distorted to be close to the white color, especially the light sign colors of yellow and fluorescent-yellow-green (FYG).
b) A normal lighting condition is a scene in which light sources are adequately applied to the whole image region, and the objects captured in the image truthfully reflect their real color.
c) An under-exposure condition is a scene in which light sources are not sufficient, so that most of the pixels in the image of under-exposure case are dimmed with a general low intensity value. In such cases, most of the colors are distorted to be close to the black color, especially the sign colors of red, blue, and green.
d) An adverse-lighting condition is a scene in which light sources are located behind the traffic signs. For the adverse-lighting case, the pixels in the image can be grouped into two clusters with general low and high intensity values, respectively. The adverse-lighting region typically contains pixels that are under-exposed with a low intensity value, while the non- adverse-lighting region typically contains pixels that are over-exposed with a general high intensity value.

There are some previous studies of image lighting condition identifications using the Gaussian mixture model (Tsai & Huang, 2010), fuzzy logic (Murakami & Honda, 1996), etc. Although demonstrating good identification capabilities, these methods are typically computationally complex and time consuming. To achieve an efficient, reliable

identification result, a simple lighting condition model using only a mean value and a median value of the video log image is employed in this section.

a) Over-exposure/ Normal-Lighting /Under-exposure Conditions

In the case of normal lighting conditions, the brightness level of all pixels follows a steady distribution throughout the whole color, and the average intensity is not overwhelmingly large or small. To the contrary, in the cases of over-exposure conditions, the mean value of the brightness levels tends to reside in the large-value section, while in the cases of the under-exposure condition; the mean value of the brightness levels tends to reside in the small-value section. Therefore:

$B_{over} = 1$ *while* $B_{mean} > B_{ThreshA}$, $B_{under} = 1$ *while* $B_{mean} < B_{ThreshB}$, *otherwise,* $B_{norm} = 1$

where B_{over}, B_{under} and B_{norm} are the indices indicating if the current video log image is under over-exposure, under-exposure, or normal conditions, respectively, while $B_{threshA}$ and $B_{threshB}$ are the upper and lower bounds of the image intensity.

b) Adverse Lighting Condition

In the case of normal lighting conditions, the brightness level of all pixels follows a steady distribution throughout the whole color and brightness ranges of each image. Therefore, the mean value differs little from the median value. To the contrary, in the cases of back lighting conditions, the median value of the brightness levels tends to reside in the small-value section and, consequently, it differs much from the average value of the whole array of all pixels. Therefore:

$B_{bl} = 1$ *while* $|B_{mean} - B_{median}| > D_{Thresh}$, *otherwise,* $B_{bl} = 0$

where B_{bl} is the index indicating if the current video log image is under back-lighting condition, and D_{Thresh} is the minimum value determining whether or not the current video log image is in adverse lighting condition.

In this simple lighting condition modeling process, the thresholds D_{Thresh}, $B_{ThreshA}$ and $B_{ThreshB}$ are yet to be determined. A calibrating dataset is created to calibrate these

thresholding values. Images containing four different lighting conditions and 300 images for each condition are selected, while the conditions are determined by human inspection.

3.2.1.2. LD-SCM Modeling

The LD-SCM model for traffic sign color segmentation follows the existing SCM model using statistical information of the nine MUTCD defined sign colors, as proposed by Tsai et al. (2009). In addition, two additional features are embedded into the formulation of the model: 1) replacing the local HSV feature with the local homogeneity feature to create new input for the LD-SCM; 2) incorporating the global image lighting condition to separately create different LD-SCM models for the corresponding lighting conditions. The former feature will help to reduce the impact of the local color non-homogeneity on the color model caused by the local noise, while the latter feature will help reduce the impact of the color distortion caused by lighting condition changes.

3.2.1.2.1. Local Pixel-Level Homogeneity Feature

Each pixel of a video log image is identified as an element of a larger homogenous region corresponding to an object, e.g. traffic sign. For color segmentation, it is very important to label the pixel with the correct color index but, more importantly, to associate the pixel with a larger homogenous region corresponding to an object. Therefore, instead of individually treating a pixel to be segmented, a local homogeneity feature is proposed to create more representative input for the LD-SCM, representing local color homogeneity. HSV color space is used to extract the pixel-level color feature, because HSV color space is recognized to effectively separate color information and intensity information. Assuming $I_{ij} = (H_{ij}, S_{ij}, V_{ij})$ represent the three color components of a pixel at the location of (i, j) in an $M \times N$ image, the following two steps describe the detailed process:

Step 1: Construct the local image window: For each pixel, a size $d \times d$ window is centered at (i, j) for the computation of the pixel-level color feature. The window size influences the computation of the local homogeneity value. The window should be big enough to allow enough local information to be involved in the computation of the local homogeneity for the center pixel of the window. Furthermore, using a larger window in the computation of the local homogeneity increases the smoothing effect and makes the derivative operations less sensitive to noise. However, smoothing the local area might hide some abrupt changes of the local region. Also, a large window causes significant processing time. A 5×5 size is selected in this study to avoid large computation time and maintain the representativeness of the homogeneity and robustness to noise.

Step 2: Compute the pixel color feature: Homogeneity is largely determined by the standard deviation and discontinuity of each color component. The standard deviation of color component σ_{ij}^{k} $(k = H, S, V)$ is commutated as

$$\sigma_{ij}^{k} = \sqrt{\frac{1}{d^2} \sum_{m=i-(\frac{d-1}{2})}^{i+(\frac{d-1}{2})} \sum_{n=j-(\frac{d-1}{2})}^{i+(\frac{d-1}{2})} (x_{ij}^{k} - \mu_{ij}^{k})^2}$$

Where

$$\mu_{ij}^{k} = \frac{1}{d^2} \sum_{m=i-(\frac{d-1}{2})}^{i+(\frac{d-1}{2})} \sum_{n=j-(\frac{d-1}{2})}^{i+(\frac{d-1}{2})} x_{ij}^{k}$$

The discontinuity of the color component e_{ij}^{k} $(k = H, S, V)$ is computed by edge values. Here the edge values are computed using a Sobel operator for the simplicity purpose:

$$e_{ij}^{k} = \sqrt{G_x^{k2} + G_y^{k2}}$$

Where G_x^{k} and G_y^{k} are the edge components in x and y directions for each color component, respectively.

Step 3: Normalization: To maintain the computation consistency, the computed values for both standard deviation and the discontinuity measurement should be normalized between 0 and 1:

$$\Sigma_{ij}^{k} = \frac{\sigma_{ij}^{k}}{\sigma_{max}^{k}}, E_{ij}^{k} = \frac{e_{ij}^{k}}{e_{max}^{k}}$$

where $\sigma_{max}^{k} = \max\{\sigma_{ij}^{k}\}, e_{max}^{k} = \max\{e_{ij}^{k}\}$.

Therefore, the local color homogeneity is represented as C_{ij}^{k} $(k = H, S, V)$, which is also within the range between 0 and 1. The more uniform the local region surrounding a pixel is, the larger the local color homogeneity value the pixel is associated with.

$$C_{ij}^{k} = 1 - \Sigma_{ij}^{k} \cdot E_{ij}^{k}$$

Through such computation, the HSV values for each pixel are transformed into the local color homogeneity values, i.e.$(C_{ij,}^{H}\ C_{ij}^{S}, C_{ij}^{V})$, not only retaining the original HSV information, but also incorporating the local neighboring homogeneity information.

3.2.1.2.2. SCM Formulation

The objective of the SCM is to establish an estimation function to fill up the missing reference values for the complete 24-bit RGB color space. The estimation function interpolates the probability density functions (PDFs) for each MUTCD defined color. To serve such objective, Tsai et al. (2009) used an ANN to train the MUTCD SCM estimation function. The ANN was implemented using a functional link network (FLN) architecture proposed by Pao and Takefuji (1992). Figure 3-4 shows the formulation of the ANN architecture, where the higher order input terms can be computed based on the formulation by Tsai et al (2009). However, to incorporate the local pixel-level homogeneity feature proposed in previous subsection, both (*H, S, V*) and $(C_{ij,}^{H}\ C_{ij}^{S}, C_{ij}^{V})$ are input into the ANN, together with their corresponding high-order input terms. Therefore, both the local pixel-level color information and the local pixel-level homogeneity information are integrated into the training process.

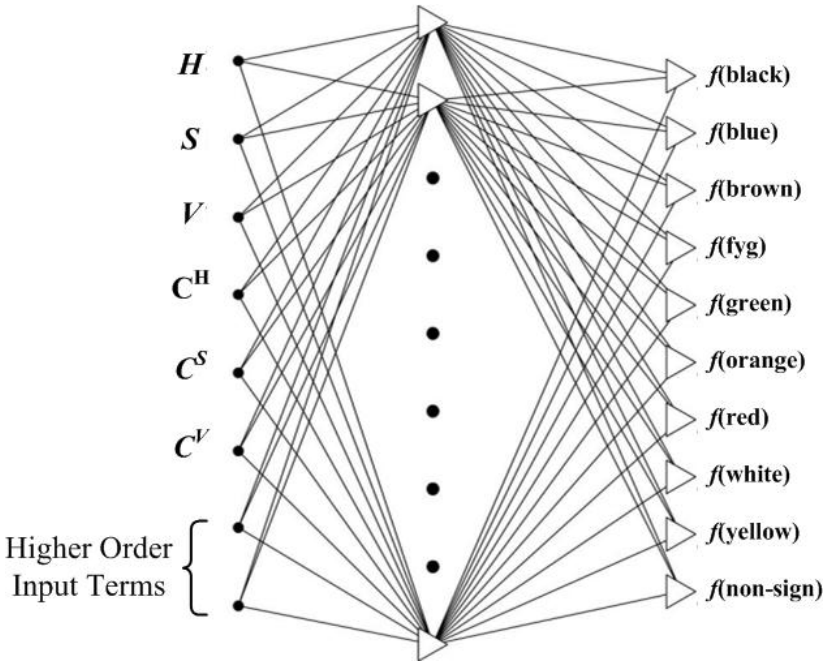

Figure 3-4 Formulation of the ANN architecture for SCM

For each lighting condition, a separate LD-SCM using the ANN training process is created. Therefore, for each pixel that is associated with different lighting conditions, three representations of the LD-SCM are used for segmentation, namely LD-SCM_{OE}, LD-SCM_{UE}, and LD-SCM_{NL}. Figure 3-5 shows an image captured in the under-exposure lighting condition and the segmentation results to demonstrate the different performance using different LD-SCMs. When applying LD-SCM_{NL}, almost all the pixels (in both sign region and background region) are incorrectly segmented as black. Instead, when applying LD-SCM_{UE}, the pixels are correctly segmented as yellow and green for the sign region and background region, respectively.

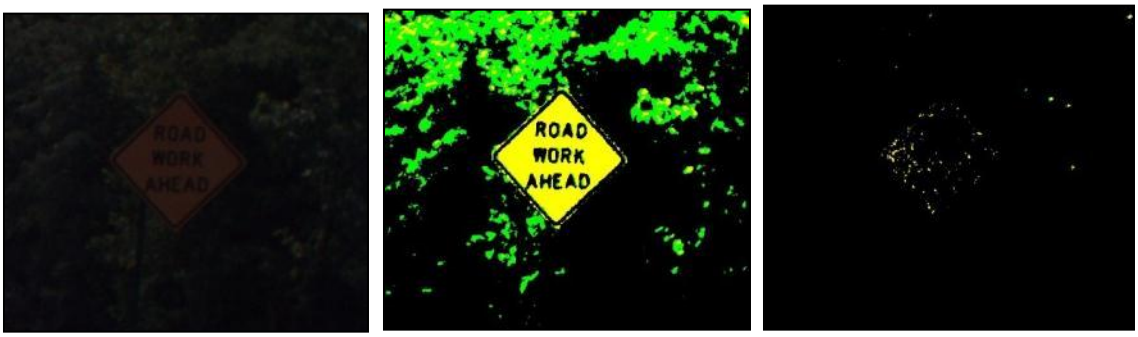

Sign in Under-Exposure **LD-SCM_{UE} Segmentation** **LD-SCM_{NL} Segmentation**

Figure 3-5 Examples of segmentation results using different LD-SCMs

To accelerate the processing speed of color segmentation, three LUTs are created for LD-SCM_{OE}, LD-SCM_{UE}, and LD-SCM_{NL} separately. Instead of running through the model and conducting color space transformation for each individual pixel, the LUTs are created, and the corresponding probabilities are hardcoded in the LUT for each color (Gomez-Moreno et al., 2010; Tsai et al., 2009). To practically implement the LUTs, 8 bits are assigned to each color component, i.e. representing the (*H, S, V*) as in [0, 255] levels, while 3 bits are assigned to each homogeneity indices, i.e. representing the$(C_{ij,}^{H}\ C_{ij}^{S}, C_{ij}^{V})$ as in [0, 7] levels.

3.2.1.3. Adverse Lighting Region Identification Using Adaptive Thresholding

Video log images captured under adverse lighting conditions typically contain two peaks in the histograms, one peak with high-intensity values (i.e. non-adverse lighting region, typically over-exposed) and one with low-intensity values (i.e. adverse lighting region, typically under-exposed). The objective of the adverse lighting region identification is to cluster the image into two regions using adaptive thresholding so that different LD-SCM models can be applied to minimize the color distortion due to different lighting conditions. Figure 3-6 shows the flow of the proposed adaptive thresholding method for adverse lighting region identification. The video log image is first diffused using an anti-geometric heat equation to produce a threshold surface (i.e. diffused image *u(x, y)*). By comparing the video log image and the threshold surface, the regions that are above the threshold surface are the candidates for non-adverse lighting regions, while the regions that are below the threshold surface are the candidates for adverse lighting regions. To remove the isolated noise points in the candidates, morphological open and close operations are applied to candidate regions. The outputs of the operations are respectively indexed as the adverse lighting region $R^{-}(x, y)$ and non-adverse lighting region $R^{+}(x, y)$.

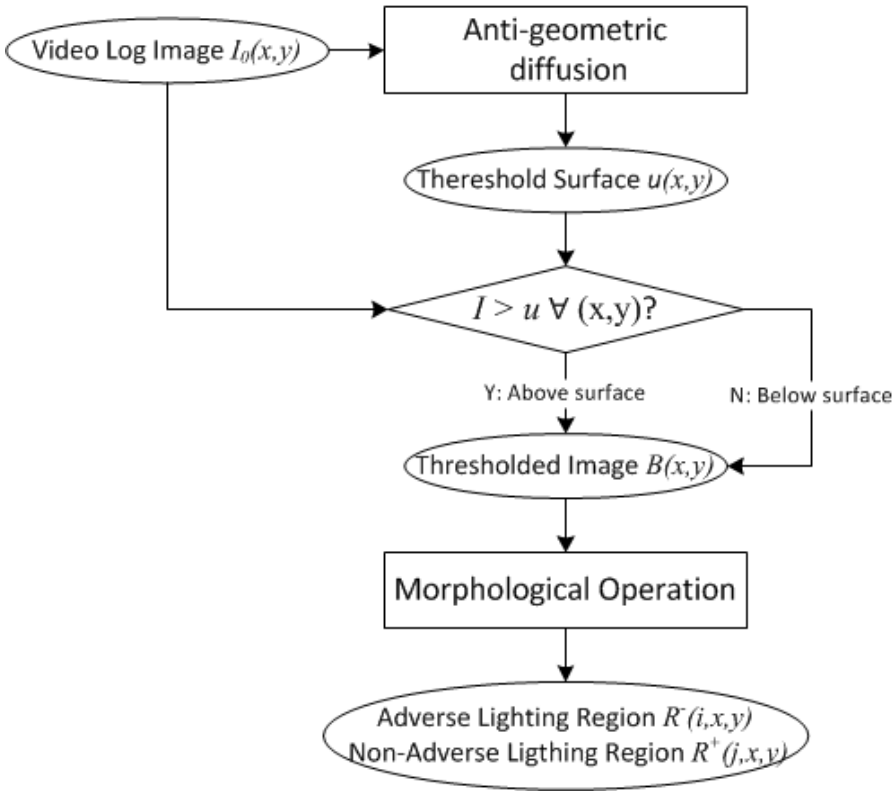

Figure 3-6 Flowchart of the adaptive thresholding method for adverse lighting region identification

A standard adaptive thresholding technique is to generate a threshold surface over the whole image domain and binarize the image by determining whether the intensity of a pixel is below or above the threshold surface. The most frequently used method is to blur the image with a designed Gaussian low-pass filter to smooth the image (equivalent to a linear heat equation). The challenge of such a method is that the filter cannot adaptively yield an optimal variance to the pixels from an edge concerning a local average (i.e. a small variance) or away from an edge concerning a global average (i.e. a large variance). To minimize the impact of image edges in finding a reliable threshold surface, an anti-geometric heat equation (Manay & Yezzi, 2003) is introduced to diffuse the image. By applying such an equation, only the diffusion in the normal direction of the edge is preserved, while the diffusion in the tangential direction is omitted.

Assuming the edge in the image is decomposed into two orthogonal directions, normal direction η and tangential direction ξ, the directions in terms of the first derivatives of the image I_x and I_y can be written as

$$\eta = \frac{(I_x, I_y)}{\sqrt{I_x^2 + I_y^2}}, \xi = \frac{(-I_y, I_x)}{\sqrt{I_x^2 + I_y^2}}$$

As the Laplacian operator is rotationally invariant, the linear heat equation can be rewritten by replacing the second order derivatives in x and y directions into in η and ξ.

$$\frac{\partial I}{\partial t} = \nabla \cdot (\nabla I) = I_{\eta\eta} + I_{\xi\xi}$$

To minimize the impact of edges in creating the threshold surface, the component in the tangential direction is omitted, i.e. ξ direction. Therefore, the anti-geometric heat equation is constructed, whose "*diffusion occurs deliberately across the boundaries of image features*" (Manay & Yezzi, 2003).

$$\frac{\partial I}{\partial t} = \nabla \cdot (\nabla I) = I_{\eta\eta} = \frac{I_x^2 I_{xx} + 2 I_x I_y I_{xy} + I_y^2 I_{yy}}{I_x^2 + I_y^2}$$

Figure 3-7 shows an image captured under adverse lighting conditions and the adaptive thresholding result using *dt = 0.2* and total 100 steps. By applying the anti-geometric heat equation to the image for diffusion, it is observed that the equation successfully identifies the adverse lighting region in the image.

Figure 3-7 Examples of the results from the proposed adaptive threshold

The final step for identifying the adverse lighting region, a morphological open and close operation, is applied to the thresholded image so that the small spikes and holes

will be removed. Figure 3-8 shows the final results after the morphological operations. The bright regions are corresponded to the non-adverse lighting regions, while the dark regions are corresponded to the adverse lighting regions. Different LS-SCMs will be applied to the two identified regions respectively.

Figure 3-8 Examples of the results before and after the morphological operation

3.2.2. ODE/PDE-Based Shape Detection Algorithm

A cluttered background is frequently captured in the video log images for traffic sign inventory, as in many other outdoor scenes. Different man-made objects, vegetation, and casting shadows of these objects are captured in the images to produce cluttered backgrounds. Figure 3-9 shows two examples of a cluttered background. A cluttered background poses a challenge for most of the shape detection algorithms using edge-based operation because the cluttered background not only contains false edges that complicate the shape detection process, but, more importantly, they intersect with the true edges that potentially destructs the shape feature of traffic signs. In this section, an ODE/ PDE-based shape detection algorithm is proposed to address the identified challenge. In this section, a region-based energy function is formulated to minimize the impact of false edges produced by a cluttered background. Both the standard region-based active contour and region-based active polygon are formulated to fit the energy function, and the optimal solution is suggested. A generalized Hough transform model for different

MUTCD defined traffic sign shapes is created to fast locate the initialization of the active polygon.

Cluttered shadows **Cluttered objects**

Figure 3-9 Examples of the cluttered background

3.2.2.1. Region-Based Energy Functional

The concept for the region-based curve evolution model defines the energy functional based on the statistics from image regions rather than gradient. Such a model was first introduced by Mumford and Shah (1989) which "*approximates the image to a piece-wise smooth representation forms of the basis for various region statistics based on segmentation algorithms*" (Appia & Yezzi, 2011). A specific case of the Mumford and Shah energy functional was implemented by Chan and Vese (2001), and uses the mean value of inside and outside the curve as the region statistics. This formulation is widely accepted for different image segmentation and object detection problems because of the simple implementation, strong physical meaning, and its unique, gradient-free feature. The same energy functional proposed by Chan and Vese is introduced in this dissertation. The intent of introducing such an energy functional is to minimize the impact of the false edges (gradients) due to the cluttered background.

The region-based energy functional consists of four components, including 1) the arc-length component, 2) the area component, 3) the inside energy and 4) the outside energy.

$$F(c_1, c_2, C) = \mu \cdot Length(C) + \nu \cdot Area\big(inside(C)\big) + \lambda_1 \int_{inside(C)} |u_0(x,y) - c_1|^2 dxdy\, \lambda_1 + \lambda_2 \int_{outside(C)} |u_0(x,y) - c_2|^2 dxdy$$

Where c_1 and c_2 are the average intensity levels inside and outside of the contour, λ_1, λ_2, μ and γ are fixed parameters that need calibration. The solution of the minimization problem is the solution for the specific object detection problem in the image domain.

$$inf_{c_1,c_2,C} F(c_1, c_2, C)$$

3.2.2.2. Formulation

This section develops and presents two formulations, active contour (AC) /active polygon (AP), using the region-based energy functional and compares their outcomes to choose the one most suitable for traffic sign detection.

3.2.2.2.1. Active Contour Formulation

Active contour is first formulated to implement the region-based energy functional. The original region-based energy functional is customized to fit the need for detection of traffic signs with 1) appropriate initialization location for the video log image and 2) fast convergence to trace the traffic sign shape. To achieve this, a new hybrid active contour (HAC) is proposed (Ai & Tsai, 2012) by incorporating three sub-energy components: location probability distribution function (PDF) sub energy, SCM sub energy, and global contour length sub energy. The complete energy functional is formulated as shown below:

$$E = \lambda \cdot \left[\int_R (I_{PDF} - u_{PDF})^2 dA + \int_{R^c} (I_{PDF} - v_{PDF})^2 dA \right] + (1 - \lambda)$$
$$\cdot \left[\int_R (I_{SCM} - u_{SCM})^2 dA + \int_{R^c} (I_{SCM} - v_{SCM})^2 dA \right] + \mu |c|$$

Where

I_{SCM} is the color-segmented video-log images,

I_{PDF} is the location PDF bitmap;

λ is a scaling parameter to balance the two sub energy components 1 and 2;

μ is a scaling parameter to control the sub energy component 3;

u and v are the average intensity inside and outside of the contour respectively.

The suffix indicates the intensity value is either from the color-segmented video-log image or the location PDF bitmap.

Sub energy component 1: Location PDF energy. The Location PDF is a 2-D probability density function that is spatially represented by a gray level bitmap in the range of a video log image, shown as Figure 3-10. It is one of the traffic sign spatial distribution characteristics that have been identified and incorporated into the energy function to speed up active contour convergence speed. The Location PDF bitmap shown in Figure 3-10 is created using 1500 video log images containing traffic signs collected by the city of Nashville by manually extracting the sign boundary. The pixels inside of the boundary are marked as black and outside of the boundary are marked as white. By cumulating the entire 1500 manually marked images, normalizing them into gray level scale and smoothing, the location PDF is generated (Hu & Tsai, 2011). The dark area indicates the locations with the high sign occurrence frequency (i.e. an image location with high likelihood of having a sign). This component is formulated using the location PDF bitmap and controls the evolvement of a contour at the early stage and enables the initial contour to quickly converge to the area with a high sign occurrence frequency with a larger contour evolving step size. Component 2 is designed to accurately trace the

detailed traffic sign boundary with a smaller contour evolving step size as described below:

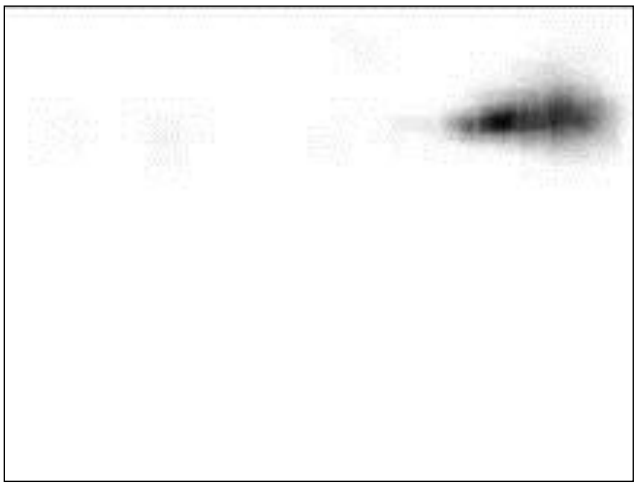

Figure 3-10 A location PDF created using 1500 video log images containing traffic signs

Sub energy component 2: SCM energy. SCM is a 2-D probability density function that is spatially represented by a gray level image in the range of the video log image shown in Figure 3-11, i.e. short for LD-SCM in this subsection. It is another important traffic sign characteristic in a 2-D image. The image is called a color-segment image, which indicates that each pixel of the image represents the likelihood of a standard MUTCD color. The dark area indicates the locations with the high likelihood of a certain color (Tsai et al., 2009). There are ten color-segmented images produced in the procedure of color segmentation using SCM, as shown in Figure 3-3. This component is formulated over one of the ten color-segmented images. For example, a yellow color-segmented image is used in Figure 3-11 because it is a yellow warning sign. This component controls the contour's evolvement at the later stage and enables the contour to accurately trace the detailed traffic sign boundary with a smaller contour-evolving step size.

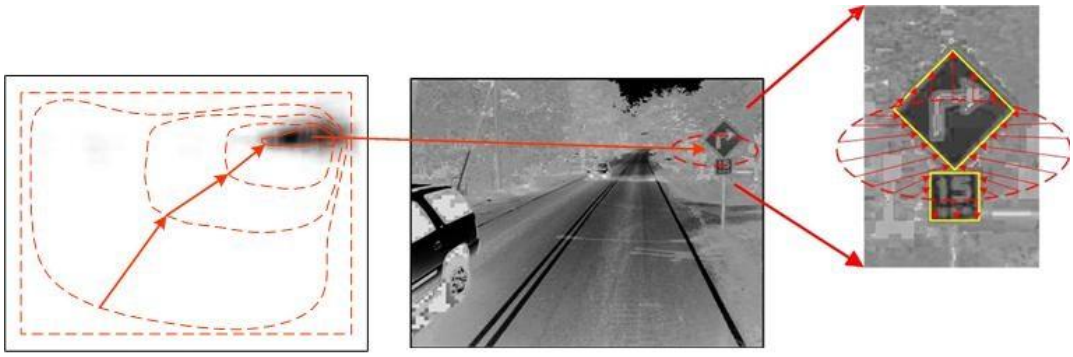

Figure 3-11 Contour evolvement forced by three sub energy components

Sub energy component 3: Global contour length energy. Global contour length is represented as the pixel length of the contour. This component is used to establish a termination criterion at the later stage that prevents the contour from being over-evolved**.** A termination criterion of a contour length not exceeding ½ of the perimeter of a video log image is used because a traffic sign in a video log image is typically less than ¼ of the entire image.

By constructing the three sub energy components, the key characteristics of a traffic sign in a video log image are incorporated into the HAC energy function formulation. The contour evolves to minimize the formulated energy function and converges when the energy is minimized. The contour evolvement is divided into a global evolvement at the early stage and a local evolvement at the later stage.

At the early stage, based on location PDF, the contour will converge to the location at which a traffic sign is mostly likely to occur in a vide log image (i.e. dark area in the location PDF bitmap), shown as Figure 3-11. The arrows show one of the contour pixels progressing directions with the contour evolvement (i.e. shrinking to the rough location globally) in this stage to quickly identify the rough location of a traffic sign at a larger step size. After the sign location is identified roughly, at the later stage, the detailed sign boundary can be traced (as shown in Figure 3-11) using a smaller contour-evolving step size. The arrows show the contour pixels progressing directions with the contour evolvement (i.e. deformation and tracing the boundary locally) at this stage. The contour

within the traffic sign area is pulled by the energy outward and with the contour outside of the traffic sign area is pushed by the energy inward until the accurate boundary is obtained. The sign boundary can be accurately traced with fast convergence speed using the proposed two-stage, contour-evolving process based on unique traffic sign characteristics.

The formulated energy in HAC can be implemented using the level set method (Chan & Vese, 2001). The energy function can be rewritten using the Heaviside function H as

$$
\begin{aligned}
&E(u_{SCM}, v_{SCM}, u_{PDF}, v_{PDF}, \phi) \\
&\quad = \lambda \cdot \left[\int_R |I_{PDF} - u_{PDF}|^2 H(\phi) dA + \int_{R^c} |I_{PDF} - v_{PDF}|^2 \big(1 - H(\phi)\big) dA \right] \\
&\quad + (1 - \lambda) \\
&\quad \cdot \left[\int_R |I_{SCM} - u_{SCM}|^2 H(\phi) dA + \int_{R^c} |I_{SCM} - v_{SCM}|^2 \big(1 - H(\phi)\big) dA \right] \\
&\quad + \mu \int_R \left| \nabla \big(H(\phi)\big) \right|
\end{aligned}
$$

where

ϕ is the level set function, where $\phi=0$ is used to guarantee each point of the contour evolves in its normal direction (Osher & Sethian, 1988);

H is the Heaviside function, which is used to differentiate the inside and outside of the contour.

The objective of the implementation is to minimize the energy function E with respect to u_{SCM}, u_{PDF}, v_{SCM}, v_{PDF} and ϕ. Keeping ϕ fixed and minimizing the energy function with respect to the constants u_{SCM}, u_{PDF}, v_{SCM} and v_{PDF}, these constants can be expressed using Equation (3). Keeping u_{SCM}, u_{PDF}, v_{SCM} and v_{PDF} fixed and minimizing the

energy function with respect to ϕ, ϕ can be expressed using the equation below, where an artificial time *t* is introduced for the energy decent direction.

$$u_X = \frac{\int_{R_X} I_X H(\phi) dA}{\int_{R_X} H(\phi) dA} \quad v_X = \frac{\int_{R_X^c} I_X \big(1 - H(\phi)\big) dA}{\int_{R_X^c} \big(1 - H(\phi)\big) dA} \quad X = SCM, PDF$$

$$\frac{\partial \phi}{\partial t} = \delta_\varepsilon(\phi)[-\lambda |I_{PDF} - u_{PDF}|^2 + \lambda |I_{PDF} - v_{PDF}|^2 - (1-\lambda)|I_{SCM} - u_{SCM}|^2$$

$$+ \lambda |I_{SCM} - v_{SCM}|^2] + \mu div\left(\frac{\nabla \phi}{|\nabla \phi|}\right) = 0$$

where $\delta_\varepsilon = H_\varepsilon$, that H_ε is a C^1-approximation of *H*, which is a classical approximation function as proposed by Chan and Vese (2001).

The objective of introducing the location PDF sub energy component is to let the contour quickly evolve to the location where a traffic sign is most likely to occur. In order to accelerate the contour convergence, the variant step sizes are designed based on location PDF area. When the evolving contour intersects with the location PDF area with 95% probability having a sign, the evolving speed will reduce from 5 pixels per step size to 1 pixel per step size. Changing the evolving speed enables a faster contour convergence with a larger step size when it is outside the location PDF area and a detailed traffic sign boundary trace with a small step size when reaching the location PDF area with high probability having a sign.

μ is defined as the scaling factor to balance the energy between the contour shape and its boundary length. 0.1 is used for the μ value as recommended in the region-based active contour method (Chan & Vese, 2001). λ is the scaling factors to balance the importance of the energy value contributed from the location PDF and the energy contributed from the color segmented image using the SCM. It is between 0 and 1. With λ closes to 1, the contour demonstrates the evolving behavior globally (in the whole image) to converge the contour quickly, controlled by the location PDF. With λ close to 0, the contour demonstrates the evolving behavior locally (in the traffic sign area) to trace

the boundary accurately, controlled by the SCM. The values of λ can be adaptively selected to balance the contour converging speed and the contour accuracy. Based on our trial and error test, the value of 0.85 can achieve a reasonable outcome in obtaining the sign boundary.

3.2.2.2.2. Active Polygon Formulation

An active polygon is, also, formulated to compare the performance of the ones obtained from the active contour (detailed results can be found in Chapter 5). Although the active contour formulation, in general, obtains good detection results, there are several cases in which the formulated unconstraint active contour using the region-based energy does not converge to the boundary of the traffic signs. Figure 3-12 shows an example where the unconstraint active contour intrudes the pictogram of the traffic sign. Many of these cases are due to the unconstraint contours over-evolving over the traffic sign that are not perfectly color segmented. To further improve the performance dealing with these cases, a constrained active contour is needed, not only following the formulated energy to trace the traffic sign boundary, but also maintaining the geometrical shape. In addition, by maintaining the geometrical shape of the active contour, the processing time will be significantly reduced.

Figure 3-12 Example of a false negative case using the unconstraint active contour

To achieve the above-mentioned objective and improve the performance of the shape detection algorithm, a constraint version of region-based active contour, i.e. region-based AP, is proposed. The region-based AP algorithm follows the same philosophy as the unconstraint active contour, but by adding additional constraints, the constructed shape only evolves following a limited number of vertices rather than arbitrarily evolve at each contour point.

The principle of formulating an active polygon initially is similar to formulating an active contour where the contour evolves following the gradient flow associated with the energy *E*. Instead of evolving each point of the contour following the gradient flow at each point, the goal is to design flows to move the "contour" by its vertices. The general form of contour $C: [a\ b] \subset \mathrm{R} \to \mathrm{R}^2$ around some region $R \subset \mathrm{R}^2$, in which the integrand f consists of a function $f: \mathrm{R}^2 \to \mathrm{R}$ is written as below:

$$E(\boldsymbol{C}) = \iint_R f(x,y)dxdy = \oint_{C=\partial R} \langle \boldsymbol{F}, \boldsymbol{N} \rangle \, ds,$$

where N denotes the outward unit normal to *C*, ds the Euclidean arc-length, and where $F = (F^1, F^2)$ is chosen so that $\nabla \cdot F = f$. By parameterization of the curve where $C(a) = C(b)$ using $p \in [a, b]$:

$$E(C) = \int_a^b \langle \boldsymbol{F}, \boldsymbol{N} \rangle \left\| \boldsymbol{C_p} \right\| dp = \int_a^b \langle \boldsymbol{F}, \boldsymbol{JC_p} \rangle dp,$$

where

$$\boldsymbol{J} = \begin{bmatrix} 0 & 1 \\ -1 & 0 \end{bmatrix}, \text{and } \boldsymbol{N} \left\| \boldsymbol{C_p} \right\| = \boldsymbol{JC_p}.$$

For the proposed active polygon, *v* denotes a Cartesian coordinate of any vertex; therefore, as manipulated by Zhu and Yuille (1996) and Yezzi et al. (2002), the gradient flow is associated with *E*, the derivative of *E* with respect to *v*.

$$E_v(\boldsymbol{C}) = \int_a^b f \langle \boldsymbol{C_v}, \boldsymbol{JC_p} \rangle dp$$

When considering C as a closed polygon V instead of a smooth curve with a fixed number of vertices $\{V_1, V_2, \dots, V_n\} = \{(x_i, y_i), i = 1,2, \dots, n\}$. Therefore, C is parameterized by $p \in [0, n]$ as

$$\boldsymbol{C}(p, \boldsymbol{V}) = L(p - \lfloor p \rfloor, \boldsymbol{V}_{\lfloor p \rfloor}, \boldsymbol{V}_{\lfloor p \rfloor + 1})$$

Where $\lfloor p \rfloor$ denotes the largest integer which is not greater than p, and where *L(t, A, B) = (1-t)A+tB* parameterized between 0 to 1 the line from A to B with constant speed, where A and B denote the end points of a polygon edge. Following such a parameterization, Unal et al. derived the gradient descent flow is

$$\frac{\partial \boldsymbol{V_k}}{\partial t} = \int_0^1 pf\big(L(p, \boldsymbol{V}_{k-1}, \boldsymbol{V}_k)\big) dp \boldsymbol{N}_{k,k-1} + \int_0^1 (1-p) f\big(L(p, \boldsymbol{V}_k, \boldsymbol{V}_{k+1})\big) dp \boldsymbol{N}_{k+1,k}$$

Where $\boldsymbol{N}_{k,k-1}$ (resp. $\boldsymbol{N}_{k+1,k}$) denotes the outward unit normal of edge ($\boldsymbol{V}_{k-1}$-$\boldsymbol{V}_k$) (resp.($\boldsymbol{V}_k$-$\boldsymbol{V}_{k+1}$)). Such a gradient descent flow essentially indicates that each of the vertices is controlled by the images values along two adjacent edges ($\boldsymbol{V}_{k-1}$-$\boldsymbol{V}_k$) and ($\boldsymbol{V}_k$-$\boldsymbol{V}_{k+1}$). The motion of each vertex is based on a weighted combination of the unit normal only at the polygon's edge points. The PDE problem as defined in an unconstraint active contour formulation is converted to an ODE problem by individually solving the ODE for each vertex for the proposed active polygon. Figure 3-13 shows an illustration of how the active polygon evolves over a video log image. The detected diamond shape maintains its geometrical shape even when there is a slight part of the legend merged into the background.

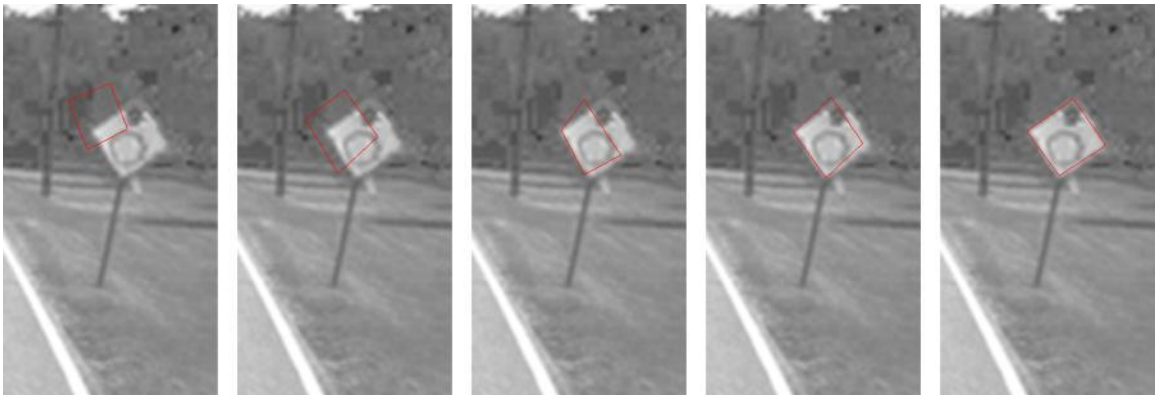

Figure 3-13 Demonstration of the active polygon flow

3.2.2.2.3. Polygon Initialization

One of the most important steps for the active polygon problem is to define the initialization location for the active polygon. The objective of polygon initialization is to identify the rough locations that have the highest likelihood for each traffic sign type. Since traffic signs are man-made objects with well-defined geometrical shapes specified in the MUTCD with a limited number of types, it is straightforward to find the polygon initialization by taking advantage of such strong geometry features. Therefore, a generalized Hough transform (GHT) is introduced for the polygon initialization. The advantages of the GHT algorithm include its being 1) capable of detecting arbitrary objects without using any analytic equation, and 2) capable of adapting to different object orientations and scales.

The GHT algorithm is a two-step algorithm containing an R-table establishment step and a detection step. The R-table establishment step is to create a template table that contains the complete specification of the exact shape of the target object.

- For the arbitrary shape shown in Figure 3-14, select the centroid (x_c, y_c) as a reference point;
- Connect the reference point and the boundary point (x, y).
- Compute the angle ϕ (i.e. the angle between the normal of the boundary point (x, y), $\boldsymbol{G}$, and the horizontal direction, $\boldsymbol{X}$);
- Store the corresponding parameters r (i.e. distance between the reference point and the boundary point) and α (i.e. the angle between the line linking (x_c, y_c) and (x, y) and the horizontal direction) as a function of ϕ;

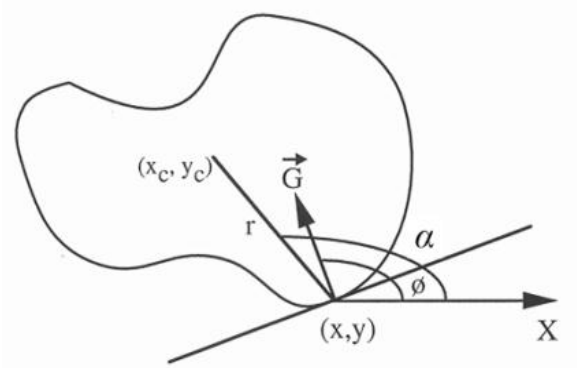

Figure 3-14 Illustration of the R-table establishment for each ϕ and edge point (x, y)

The R-table represents the complete specification of the exact shape of the target object. For different traffic sign shapes, different R-tables should be prepared individually. There are seven different convex traffic sign shapes that are defined in the MUTCD as shown in Figure 3-15, including, triangle, rectangle, trapezoid, diamond, pentagon, octagon, and circle. Nine different R-tables are created for sign detection purposes.

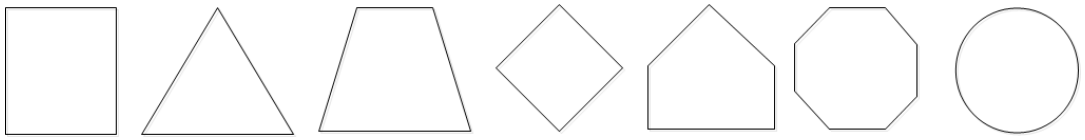

Figure 3-15 Illustrations of different MUTCD defined traffic sign shapes

The detection step is to find the object center where the maximal similarity is identified based on the complete specification of the target object. The pseudo-code below shows the process of shape detection step. As the orientation and scale of traffic signs captured in the video log images can be changed due to different capture distances, angles or the condition changes of the signs themselves, the orientation and scale factors are introduced.

```
Quantize the parameter space:
          P[x_{c_min} ··· x_{c_max}][y_{c_min} ··· y_{c_max}][θ_min ··· θ_max][s_min ··· s_max]
For each edge point (x, y)
      Using gradient angle φ, retrieve all the (α, r) values from the
      R-table
      For each (α, r), compute the candidate reference points:
                x′ = rcos(α)
                y′ = rsin(α)
      For (θ = θ_min; θ ≤ θ_max; θ++)
```

For $(s = s_{min}; s \leq s_{max}; s{+}{+})$
$x_c = x - (x'\cos(\theta) - y'\sin(\theta))\, s$
$y_c = y - (x'\sin(\theta) - y'\cos(\theta))s$
$++P[x_c][y_c][\theta][s]$

Possible locations of the object are given by local maxima in $P[x_c][y_c][\theta][s]$.

Figure 3-16 shows an example of the result finding a diamond-shaped polygon initialization location. The initialization shown in Figure 3-16(c) will be used as the starting shape of the proposed active polygon algorithm. The exact shape of the traffic sign will be extracted.

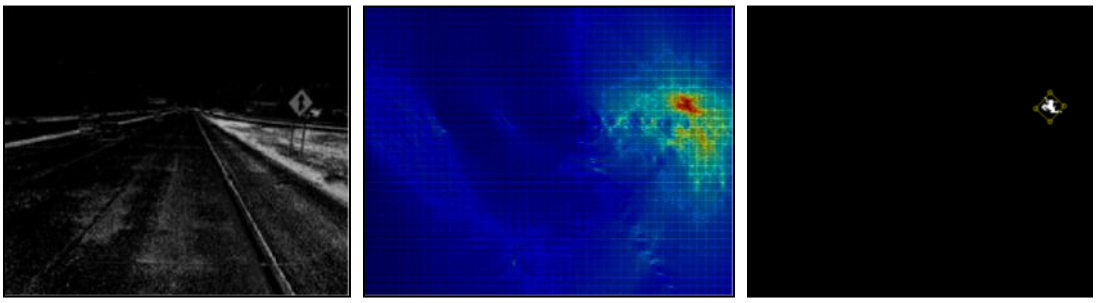

(a) Segmented Image **(b) GHT Accumulator** **(c) Initial Polygon**

Figure 3-16 Examples of the results from GHT-based polygon initialization

CHAPTER 4

AN MOBILE TRAFFIC SIGN RETROREFLECTIVITY CONDITION ASSESSMENT METHODOLOGY USING MOBILE LIDAR AND COMPUTER VISION

4.1. Objective

The objective of this chapter is to propose a mobile traffic sign retroreflectivity condition assessment method to improve the efficiency and reliability of the current retroreflectivity condition assessment method used by state department of transportation (DOTs). As identified in Chapter 2, the intent of proposing such a mobile method is to explore the feasibility of using emerging mobile light detection and ranging (LiDAR) and computer vision technologies for retroreflectivity condition assessment purposes, along with existing image-based methods. First, an image-LiDAR registration algorithm is developed to associate the 3D LiDAR point with traffic sign color information. Second, a study of the fundamental behavior of LiDAR retro-intensity values with respect to the key mobile LiDAR data attributes is conducted. Finally, the traffic sign retroreflectivity condition is associated with the LiDAR retro-intensity value for condition assessment.

4.2. Proposed Methodology

Retroreflectivity is the most critical attribute of a traffic sign for nighttime visibility. It is defined as the ratio of the luminance that is redirected from a sign's surface to the luminance originating from a vehicle's headlight (ASTM, 2011). A LiDAR system collects the retro-intensity values in a way similar to the measurement of traffic sign retroreflectivity. A retro-intensity value is acquired with each LiDAR point, which measures the ratio of the energy redirected from the object to the energy emitted from the

LiDAR sensor. Hence, there is a possible correlation between the retro-intensity values and the traffic sign retroreflectivity conditions. Such a correlation can potentially be used to conduct an automatic traffic sign retroreflectivity condition assessment. Nevertheless, there are two challenges preventing direct application of the raw LiDAR point cloud data to assess the traffic sign retroreflectivity condition: 1) multiple colors for the same traffic sign need to be assessed separately to meet the manual of uniform traffic control devices (MUTCD) requirements, but the raw LiDAR point cloud data does not contain any color information; 2) the raw retro-intensity values are acquired at different beam distances and incidence angles, but the population of the retro-intensity values associated with the same traffic sign should be assessed at the same beam distance and incidence angle. Therefore, the proposed method focuses on three key points: 1) automatically clustering the raw LiDAR point cloud data to generate the populations of retro-intensity values for different traffic sign colors; 2) normalizing the retro-intensity values based on the beam distance and incidence angle to make a consistent assessment of the traffic sign; 3) establishing the relationship between the retro-intensity values and the retroreflectivity conditions. Figure 4-1 shows the flow for the proposed method. The proposed method includes five steps:

- Traffic sign detection to automatically extract the traffic sign ROIs from video log images.
- Color segmentation to segment different traffic sign colors for each extracted ROI from the previous step.
- Traffic sign-associated LiDAR point extraction to register the LiDAR point cloud with the corresponding image pixels and to extract these LiDAR points with the associated sign and color information.
- Retro-intensity normalization to normalize each retro-intensity value within the clusters created in STEP 3 based on the beam distance and the incidence angle.

- Retroreflectivity condition assessment to quantitatively assess the traffic sign retroreflectivity condition by comparing the median value from the population of the normalized retro-intensity with the established threshold defining PASS and FAIL conditions.

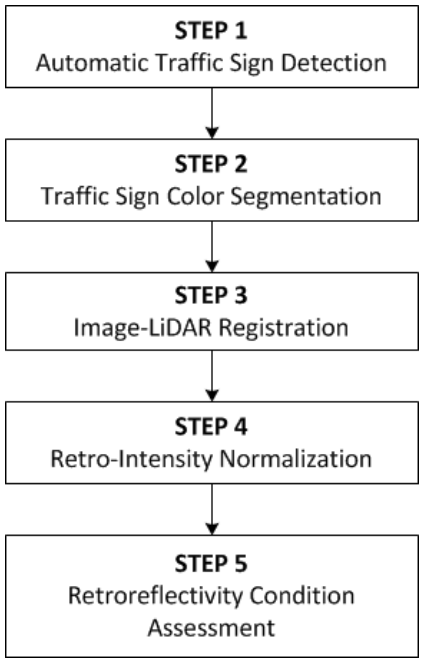

Figure 4-1 The proposed method for traffic sign retroreflectivity condition assessment

4.2.1. STEP 1 and STEP 2 - Traffic Sign Detection and Color Segmentation

Traffic sign detection and color segmentation in this step uses the method proposed in Chapter 3. The output of this step is the traffic sign ROIs and the color segmentation results for each detected ROI. Every traffic sign-associated image pixel is indexed with a MUTCD color.

4.2.2. STEP 3 - Traffic Sign-Associated LiDAR Point Extraction

A 3D LiDAR point contains accurate position information and a corresponding retro-intensity value. However, there is no prior traffic sign location information or traffic sign color information incorporated into the point cloud. It is essential to incorporate the results from STEP 1 (i.e. traffic sign location information in a 2D coordinate system) and

STEP 2 (i.e. traffic sign color information for legend and background), so that the subsequent condition assessment can be conducted based on the corresponding population of LiDAR points that are associated with each color for the same traffic sign.

Figure 4-2 shows the flowchart for the proposed traffic sign-associated LiDAR point extraction method. First, camera calibration is conducted to obtain the intrinsic camera parameters and to establish the camera homography. Using the camera homography and the existing sensor configuration, the transformation matrix from GPS coordinates and image coordinates can be obtained. As the camera homography and the sensor configuration are the same during the data collection, an image-LiDAR registration can be achieved using only the transformation matrix. With the detected traffic sign's location in the image and the corresponding color segmentation results, traffic sign-associated LiDAR points for each sign can be extracted. Due to the noise and irregularity of the LiDAR points, the extracted sign-associated LiDAR points for each traffic sign can be projected as a 2D image containing the essential retro-intensity information for subsequent condition assessment steps.

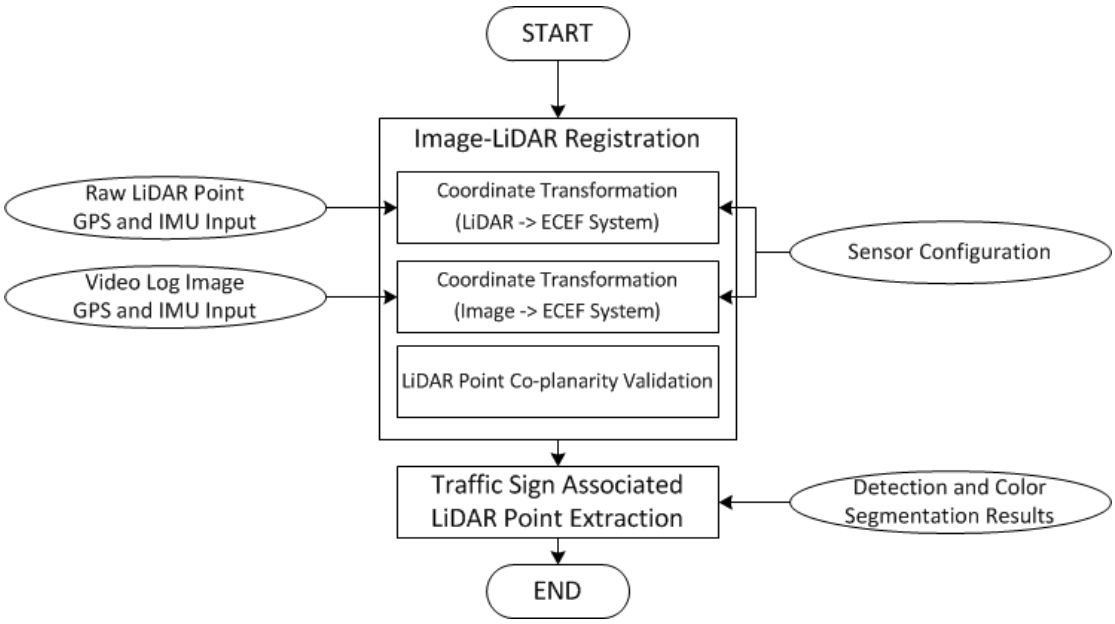

Figure 4-2 The flowchart for the STEP 3 of Traffic Sign-Associated LiDAR Point Extraction

4.2.2.1. An Image-LiDAR Registration Method

The objective of image-LiDAR registration is to obtain the transformation matrix between the 2D image coordinate system and the 3D LiDAR sensor collection system. Therefore, each LiDAR point can be associated with the traffic sign detection result and it corresponding color. There are many studies that have been conducted for registering LiDAR point clouds with satellite/airborne imagery, most of which use feature matching techniques between a 3D LiDAR point cloud and a 2D image using control points or unique objects that are visible in both data (Mishra & Zhang, 2012). However, it is identified that the feature-matching-based registration methods are not only computationally expensive, but most of them require re-registration for different datasets. In this study, an image-LiDAR registration method is proposed using only the sensor position transformation, camera calibration, and point cloud co-planarity, as shown in Figure 4-2.

4.2.2.1.1. Coordinate Transformation between LiDAR Sensor and ECEF

For a LiDAR system, the measurement from the sensor includes the distance between the LiDAR sensor center to the object and the offset angle between the laser beam and the center scanning beam. To obtain the 3D coordinates in the Earth-Centered, Earth-Fixed (ECEF) reference datum (e.g. WGS-84 in this study), a series of translations and rotations obtained from sensor observation and configuration constants is essential to a LiDAR pulse measurement for direct geo-positioning of the object (NGA, 2009). Figure 4-3 shows the illustration of all the necessary translations and rotations .

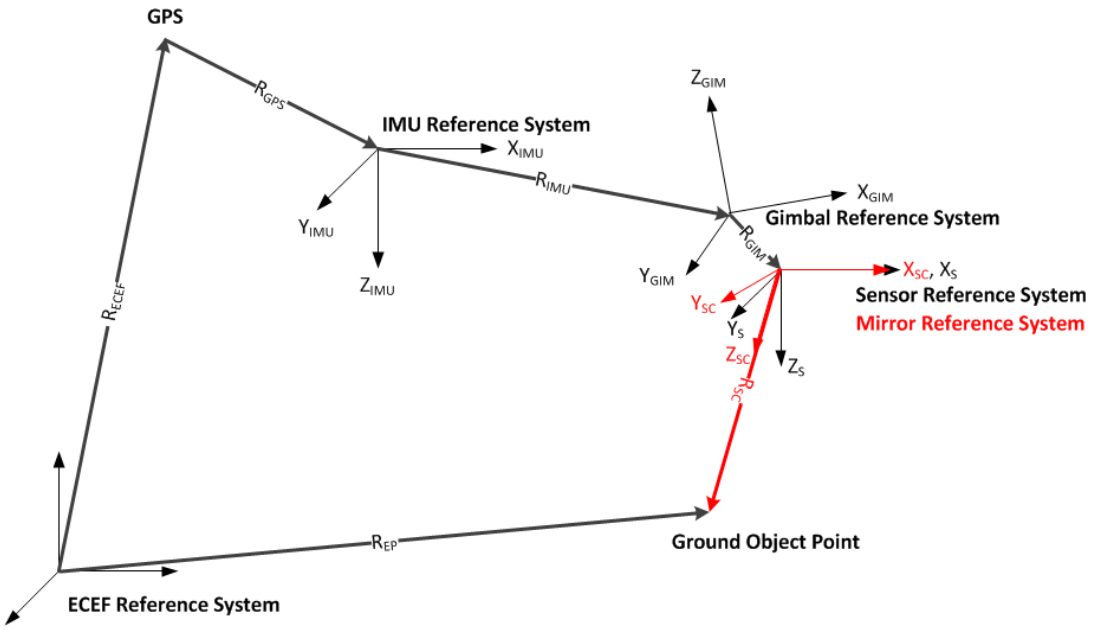

Figure 4-3 Translations and rotations between the LiDAR and the ECEF reference systems

The coordinates of a sensed object point in a geocentric ECEF coordinate system are obtained from the following equation:

$$R_{EP} = R_{ECEF} + M_{ECEF} \cdot M_{ELL} \cdot M_{VER} \cdot (M_{PLA} \cdot (M_{GIM} \cdot M_{SEN} \cdot (R_{SCA} + R_{GIM}) + R_{INS} + R_{GPS}))$$

- R_{SCA} - vector from the scanner to the ground point in the scanner reference frame
- R_{GIM} - vector from the gimbal center of rotation to the sensor in the gimbal reference frame
- R_{INS} - vector from the IMU to the gimbal center of rotation in the platform reference frame
- R_{GPS} - vector from the GPS antenna phase-center to the IMU in the platform reference frame
- R_{ECEF} - vector from the ECEF origin to the GPS antenna phase-center in the ECEF reference
- R_{EP} - vector from the ECEF origin to the ground point in the ECEF reference frame
- M_{SEN} - rotation matrix from scanner reference frame to sensor reference frame
- M_{GIM} - rotation matrix from the sensor reference frame to the gimbal reference frame
- M_{PLA} - rotation matrix from the gimbal reference frame to the platform reference frame
- M_{VER} - rotation matrix from the platform reference frame to the local-vertical reference frame
- M_{ELL} - rotation matrix from the local-vertical reference frame to the ellipsoid-tangential (NED) reference frame
- M_{ECEF} - rotation matrix from the NED reference frame to the ECEF reference frame

In the equation, M represents the rotation matrix between different reference coordinate systems, while R represents the translation between different reference coordinate systems. Specifically, R_{SCA} and M_{SEN} are the readings obtained from the LiDAR sensor for each scanning point, while M_{VER} is the reading obtained from the IMU sensor for each scanning point, and the R_{ECEF} is the reading obtained from the GPS for each scanning point. The remaining values can be obtained from the sensor configuration on the data collection vehicle (i.e. lever arms) and the simple geo-referencing system conversion (i.e. M_{ELL} and M_{ECEF}).

By applying the above equation for each LiDAR point, corresponding GPS coordinates (i.e. ECEF coordinates) can be obtained. These 3D coordinates will be input into the subsequent camera coordinate system to obtain the corresponding image coordinates.

4.2.2.1.2. Coordinate Transformation between Camera Sensor and ECEF

For a camera system, the measurement from the sensor includes the color intensity information obtained by the camera (i.e. lens and the photometric device). To project the ECEF coordinate to the camera coordinate system, a 3D-to-2D translation and rotation matrix is necessary. In this study, the simple linear model using a collinearity equation is introduced to obtain such a transformation matrix. Figure 4-4 shows the illustration for the collinearity between the object in the ECEF reference system and the camera reference system. As shown in the figure, the camera perspective center L, an arbitrary object point A, and its corresponding image point captured in the image plane are collinear. Therefore, vectors from the perspective center L to the image point and the object point are directly proportional. In order to associate each component of these vectors, these vector components must be defined with respect to the same coordinate system (NGA, 2009).

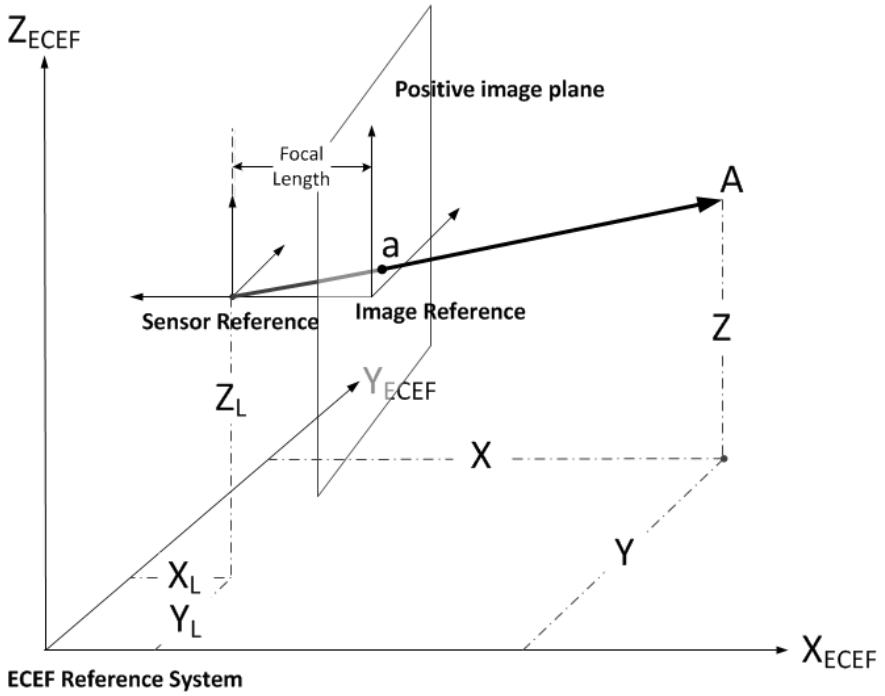

Figure 4-4 Collinearity relationship between the object in the ECEF and the camera reference systems

Therefore, the association between the object point A and the image point a can be defined as

$$a = k\boldsymbol{MA}$$

where k is the scalar multiplier and M is the orientation matrix of the camera that incorporates the camera rotation angles in three directions (i.e. roll, pitch and yaw) with respect to the vehicle local-vertical reference frame and the rotation angles between the vehicle local-vertical reference system to the ECEF reference system. From Figure 4-4, the collinearity condition can be represented as shown below:

$$\begin{bmatrix} x & 0 \\ y-0 & \\ 0 & f \end{bmatrix} = k\boldsymbol{M}\begin{bmatrix} X & X_L \\ Y-Y_L & \\ Z & Z_L \end{bmatrix}$$

Where (x, y) are the image coordinates of a, (X, Y, Z) and (X_L,Y_L,Z_L) are the coordinates of the object A and the camera perspective center L, respectively. Using the subscripts to represent the transformation matrix $\boldsymbol{M}$, the collinearity equation results in the following representation:

$$\begin{bmatrix} x & 0 \\ y-0 & \\ 0 & f \end{bmatrix} = k \begin{bmatrix} m_{11} & m_{12} & m_{13} \\ m_{21} & m_{22} & m_{23} \\ m_{31} & m_{32} & m_{33} \end{bmatrix} \begin{bmatrix} X & X_L \\ Y-Y_L & \\ Z & Z_L \end{bmatrix}$$

Note that although the earlier derivation expressed coordinates with regard to the image plane ("negative" plane), the image point *a* in Figure 4-4 is represented by coordinates (*x*, *y*) whose relation is simply a mirror of the image plane. Thus, the components of a will have opposite signs of their mirror components (*x*, *y*) as follows:

$$\bar{x} = -(x - x_0)$$

$$\bar{y} = -(y - y_0)$$

where (x_0, y_0) is the image coordinates for the image center. By solving the collinearity equation for any give object, its ECEF ground coordinates (*X*, *Y*, *Z*) are related to its image coordinates (*x*, *y*) by the following equation:

$$x = x_0 - f \cdot \left[\frac{m_{11}(X - X_L) + m_{12}(Y - Y_L) + m_{13}(Z - Z_L)}{m_{31}(X - X_L) + m_{32}(Y - Y_L) + m_{33}(Z - Z_L)} \right]$$

$$y = y_0 - f \cdot \left[\frac{m_{21}(X - X_L) + m_{22}(Y - Y_L) + m_{23}(Z - Z_L)}{m_{31}(X - X_L) + m_{32}(Y - Y_L) + m_{33}(Z - Z_L)} \right]$$

where x_0, y_0 and f are derived from intrinsic camera calibration process as in the following matrix:

$$M_{in} = \begin{bmatrix} -f/s_x & 0 & x_0 \\ 0 & -f/s_y & y_0 \\ 0 & 0 & 0 \end{bmatrix}$$

where s_x and s_y are the pixel size of the camera in x and y directions. These parameters can be obtained based on the actual camera sensor scale and the corresponding resolution. There are many methods that have been conducted in previous studies. In this study, Zhang's approach (Tsai, 1987; Zhang, 2000) was used because it is the most popular approach nowadays. The camera calibration results M_{in} can be obtained before the data collection is conducted. The transformation matrix **M** provides the alignment between the camera coordinate system and the ECEF coordinate system. Therefore, the matrix is simple: the rotation matrices provided for the LiDAR system,

where the only difference is that instead of using the M_{PLA} for the LiDAR system, simply apply the camera orientation angles.

$$M = M_{ECEF} \cdot M_{ELL} \cdot M_{VER} \cdot M_{PLA}$$

For the camera position (X_L,Y_L, Z_L), following the same line of thought as shown in Figure -4 sets the range vector R_{SCA} to be zero and the R_{GIM} to be the vector between the camera sensor and its corresponding support frame R_{CAM}. Therefore, the camera position in the ECEF reference system can be represented as

$$R_L = R_{ECEF} + M_{ECEF} \cdot M_{ELL} \cdot M_{VER} \cdot (M_{PLA} \cdot R_{CAM} + R_{INS} + R_{GPS})$$

4.2.2.1.3. LiDAR Point Co-Planarity Validation

Using the ECEF coordinates computed from the LiDAR presented in section 4.2.2.1.1 and the transformation equation derived from section 4.2.2.1.2, each LiDAR point can be associated with an image pixel (x, y). With an accurate camera calibration and measurements of the offsets and poses among different sensors, i.e. mobile LiDAR, cameras, IMU and GPS, the registration between the LiDAR points and the image is reliable. However, there are some cases in which some points can be falsely computed from the LiDAR sensor. Figure 4-5 shows an example of such a LiDAR measurement error. Most of these error points occur at the edge of traffic signs due to the partial reflection of the laser beam. Therefore, the retro-intensity values within these points are significantly smaller than the typical point reflected from the traffic sign surface. Although these points can be registered with image pixels that are associated with the detected traffic signs, the retro-intensity values within these points should not be included in the subsequent condition assessment.

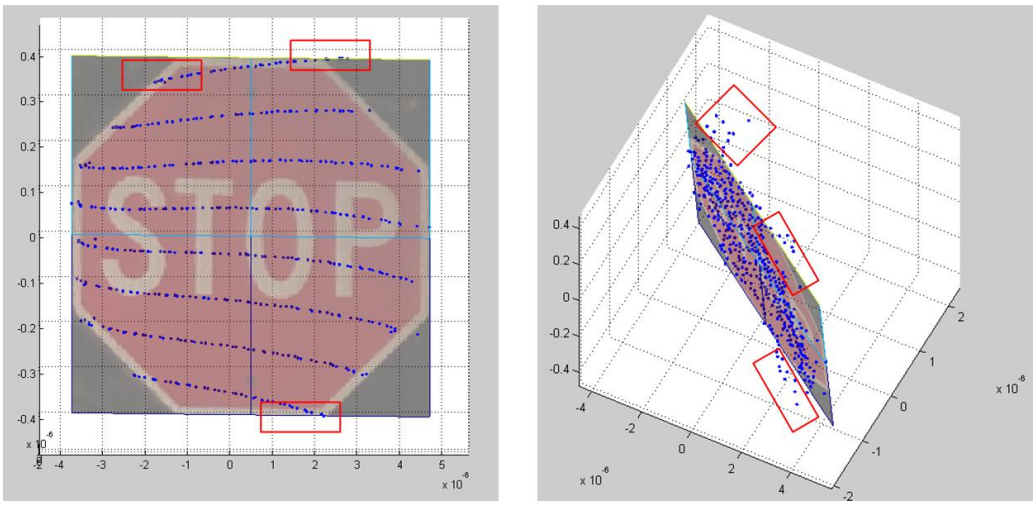

Figure 4-5 An example of LiDAR measurement error – "abnormal points"

Therefore, a co-planarity validation process is introduced to eliminate these "abnormal points." For each traffic sign associated LiDAR point cloud, principle component analysis (PCA)-based traffic sign surface plane estimation is first conducted to regenerate the traffic sign surface. The following equations are constructed for PCA computation for the optimal normal of the given data, i.e. each traffic sign associated LiDAR point cloud. The solution is obtained from the three eigenvectors. The eigenvectors represent the three axes of the point cloud, while the eigenvalues denote the square sum of points deviating along the corresponding axis. Therefore, the eigenvector corresponding to the smallest eigenvalue will be the normal direction of the best-fit plane.

$$C = \frac{1}{k}\sum_{i=1}^{k}(\boldsymbol{p}_i - \overline{\boldsymbol{p}}) \cdot (\boldsymbol{p_i} - \overline{\boldsymbol{p}})^T, \qquad C \cdot \vec{v}_j = \lambda_j \cdot \vec{v}_j, j \in \{0,1,2\}$$

where k is the number of points in the point cloud $\boldsymbol{p_i}$, $\overline{\boldsymbol{p}}$ is the centroid of the cluster, λ_j is the j-th eigenvalue of the covariance matrix C and $\vec{v}_j$ is the j-th eigenvector.

The PCA approach utilizes all the data within the cloud for plane estimation, including the "abnormal points." Therefore, the "abnormal points" could still impact the surface estimation results. Therefore, a robust estimation approach proposed by Daniels, et al. (2007) is introduced here to minimize the impact of the "abnormal points" on the final surface estimation results. After the first estimation using PCA, the distances from

the points to the initial plane can be computed. If a distance is within 2 times of the standard deviation, the point will maintain its weight. Otherwise, it will be assigned a lower weight for recalculating the optimal plane. The following equation is used to determine the weights:

$$\omega = \begin{cases} 1 & where\ |V| \leq 2\sigma \\ e^{-c \cdot V^2} & where\ |V| > 2\sigma \end{cases}$$

Where V is the residual for each point, c is a constant for calibration, and p is the weight of each point that will be contributing to the optimal plane. Through trial and error, c=100 gives the best results for this study. Using the robust estimation approach, an optimal plane using PCA and the adjusted weights can be derived. All the points with a distance that is greater than 2 cm from the derived plane, i.e. the LiDAR ranging measurement precision in this study, from the regressed surface are rejected from the subsequent condition assessment steps.

4.2.2.2. Traffic Sign-Associated LIDAR Point Extraction

The principle for associating the LiDAR points with the traffic sign detection results is straightforward. After establishing the registration between the LiDAR point cloud and video log images, the traffic sign-associated LiDAR points can be identified and indexed with different traffic sign colors by inputting the traffic sign detection results from video log images from Steps 1 and 2 (i.e. image coordinates for the traffic sign bounding box). Each detected ROI is associated with a population of LiDAR points. Within each ROI, each pixel (*x*,*y*) is segmented as one traffic sign color, e.g. red and white for a stop sign. The population of the LiDAR points is further indexed based on the corresponding segmentation color. Figure 4-6 shows an example of a stop sign after this step. The LiDAR points that are indexed with red and white are separated, and they will be assessed separately in subsequent steps.

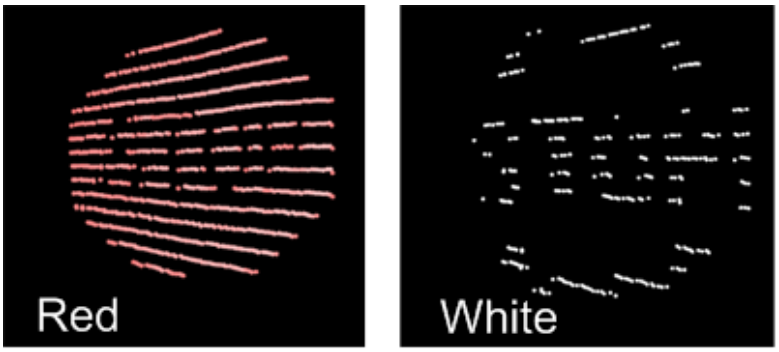

Figure 4-6 The result of a stop sign after sign associated LiDAR point cloud retrieval

4.2.3. STEP 4 - LiDAR Retro-Intensity Value Normalization

The objective of LiDAR retro-intensity value normalization is to establish the relationship between the raw retro-intensity values obtained by the LiDAR and key data collection factors that could impact the retro-intensity values. These relationships are critical to maintaining the consistency of the retroreflectivity condition assessment for traffic signs as proposed in this chapter. Two key factors that are identified from the literature are focused on in this study (Voegtle & Wakaluk, 2009): the LiDAR beam distance and the LiDAR incidence angle.

4.2.3.1. LiDAR Retro-Intensity Normalization Modeling

Characteristics of LiDAR retro-intensity have been studied by other researchers, especially in the field of airborne LiDAR. Both theoretical and empirical models have been established for airborne LiDAR point cloud data. The key characteristics identified in previous studies include beam distance (Aytac & Barshan, 2005; Cheng & Glenn, 2009), incidence angle (Aytac & Barshan, 2005), atmosphere distortion (Kaasalainen et al., 2005; Mazzarini et al., 2007) and surface structure (Voegtle & Wakaluk, 2009). However, it is found that establishing a robust retro-intensity model with respect to the key factors is challenging due to the imperfect data collection condition, limited measurement capability, and complication of surface radiology characteristics. It is recommended that a theoretical-empirical model for different applications and individual LiDAR equipment (Voegtle & Wakaluk, 2009) be established. However, there are very

few studies of the key factors for mobile LiDAR application, e.g. traffic sign retroreflectivity condition assessment. Therefore, the focus of this section is to study the characteristics of the key factors for the mobile LiDAR application on traffic sign retroreflectivity. Beam distance and incidence angle are the two key factors in the mobile LiDAR application for traffic sign retroreflectivity condition assessment, while the impact of the other factors, i.e. atmosphere distortion and surface structure, is minimal in such an application.

4.2.3.1.1. Theoretical Model

In previous studies on airborne LiDAR sensors, Kamermann (1993) and Pfeifer et al. (2007) introduce a general energy receiving model for laser scanning systems:

$$I_A = IR^a e^{2bR} cos^c(\vartheta) e^d$$

where *I* is the measured intensity, and *R* is the distance between the sensor and the object ϑ, the incidence angle and *a, b, c, d* are constant parameters to be calibrated. Following is a description of beam divergence. The exponent *2bR* concerns the attenuation by the two way propagation of the laser beam. The term *c* models the type of reflectivity and *d* normalizes the whole value to be 1. For mobile LiDAR, as the atmosphere attenuation is ignorable, the equation can be further simplified as follows:

$$I_A = IR^a cos^c(\vartheta) e^d$$

By further incorporating the classic light illumination model using an empirical Phong surface model (including ambient light, diffused reflection light, and specular reflection light (Foley et al., 1995)), the general formula is as follows:

$$I_A = I_a k_a + I_{in}[k_d cos(\vartheta) + k_s cos^n(\theta)]$$

For retroreflective material, the specular reflection angle is always zero, as the incidence beam is always parallel to the reflecting beam. By ignoring the ambient lighting (LiDAR operates in the near-infrared spectrum) and considering $k_a + k_d + k_s = 1$, the equation is simplified as

$$I_A = IR^a/[(1-k_s)cos(\vartheta)+k_s]$$

For the LiDAR retro-intensity value, which is the ratio between the emitted energy from the sensor and the received energy reflected from the surface, the retro-intensity value from mobile LiDAR can be modeled as

$$\rho = I/I_A = [(1-k_s(\vartheta))cos(\vartheta)+k_s(\vartheta)]\cdot R^{-a} = f(\vartheta)\cdot g(R)$$

where

$$f(\vartheta) = (1-k_s(\vartheta))cos(\vartheta)+k_s(\vartheta) \text{ and } g(R) = R^{-a}$$

Depending on different traffic sign sheeting material, the specular light is a function of incidence angles, i.e. $k_s(\vartheta)$. Such a function requires calibration to determine the detailed values at each incidence angle. Based on the internal research conducted by 3M, the specular function can be a second order function with respect to the incidence angle.

4.2.3.1.2. Empirical Model Parameter Calibration

To obtain the relationship between the retro-intensity and the beam distance and the incidence angle by calibrating the function $k_s(\vartheta)$, two lab tests were conducted. For the beam distance test shown in Figure 4-7(a), the position of the testing traffic sign was manually changed to simulate different beam distances, while the LiDAR sensor was stationary and adjusted at a fixed orientation. For the incidence angle test shown in Figure 4-7 (b), the orientation of the tested traffic sign was manually rotated from 0 °to 80 °, and the LiDAR sensor was stationary and adjusted at the fixed beam distance. The collected LiDAR data, then, was processed to obtain the retro-intensity relationships as functions of the beam distance and of the incidence angle, as shown in Figure 4-7.

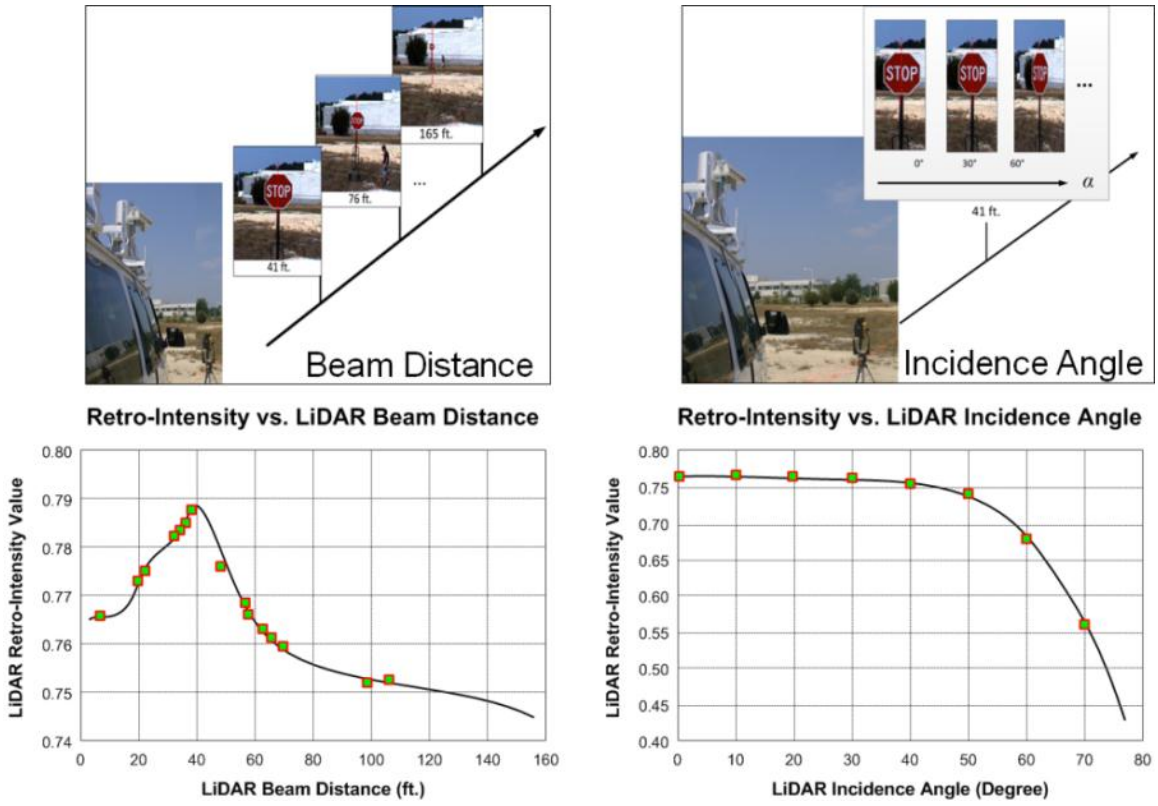

(a) **(b)**

Figure 4-7 Field test for retro-intensity normalization and generated retro-intensity curves

For beam distance, by fitting the collected data to the exponential model with respect to the beam distance, it is identified that the data points with beam distances greater than 15m (approx. 50 ft.) fit the exponential model very well, while the points with beam distances less than 15m fit the exponential model poorly. Further investigation identified that the specific model used for the field test (i.e. RIEGL LMS-Q120i) contains a range-dependent amplification of the laser signal when the range is smaller than 15m. Therefore, the beam distance model for the specific LiDAR model is modified based on the internal configuration shown below. Figure 4-8 shows the regression results for the relationship between the LiDAR retro-intensity and the beam distance.

$$g(R) = \begin{cases} 1.0939 \cdot R^{-0.04224} & when\ R > 15 \\ 0.0042R + 0.9357 & when\ R \leq 15 \end{cases}$$

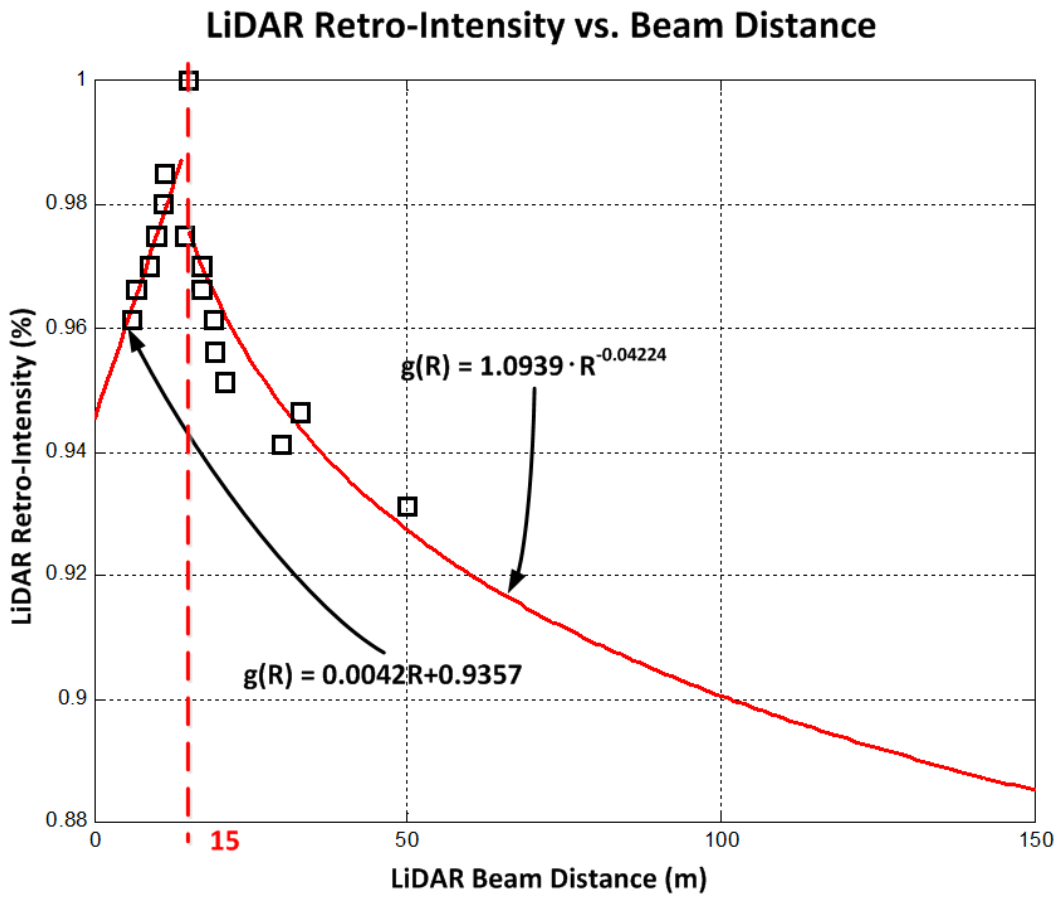

Figure 4-8 Regression results for the relationship between the LiDAR retro-intensity and the beam distance

For incidence angle, different k_s values are tested to better fit the $k_s(\vartheta)$ with the observed retro-intensity values in response to a different incidence angle. Figure 4-9(a) shows an illustration of different k_s values and the observed retro-intensity values from the test. Figure 4-9(b) shows the k_s value in response to a different incidence angle. By using a second order polynomial regression, the function of $k_s(\vartheta) = -0.0001 \cdot \vartheta^2 - 0.0003 \cdot \vartheta + 0.9985$ can be derived. Therefore, the incidence angle model can be represented as shown below:

$$f(\vartheta) = (0.0015 - 0.0001 \cdot \vartheta^2 + 0.0003 \cdot \vartheta)cos(\vartheta) - 0.0001 \cdot \vartheta^2 - 0.0003 \cdot \vartheta + 0.9985$$

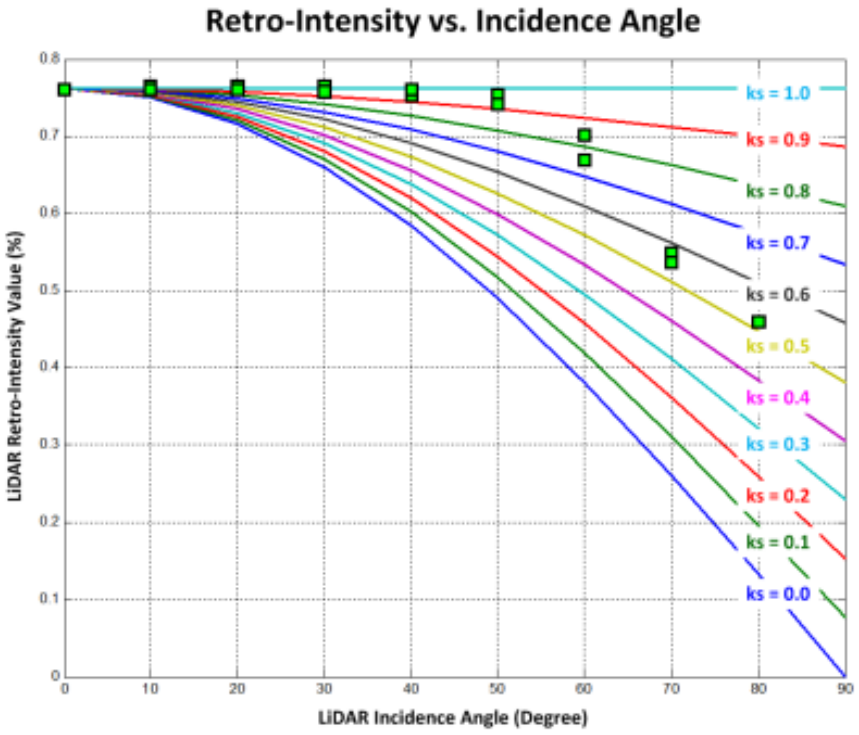

(a)

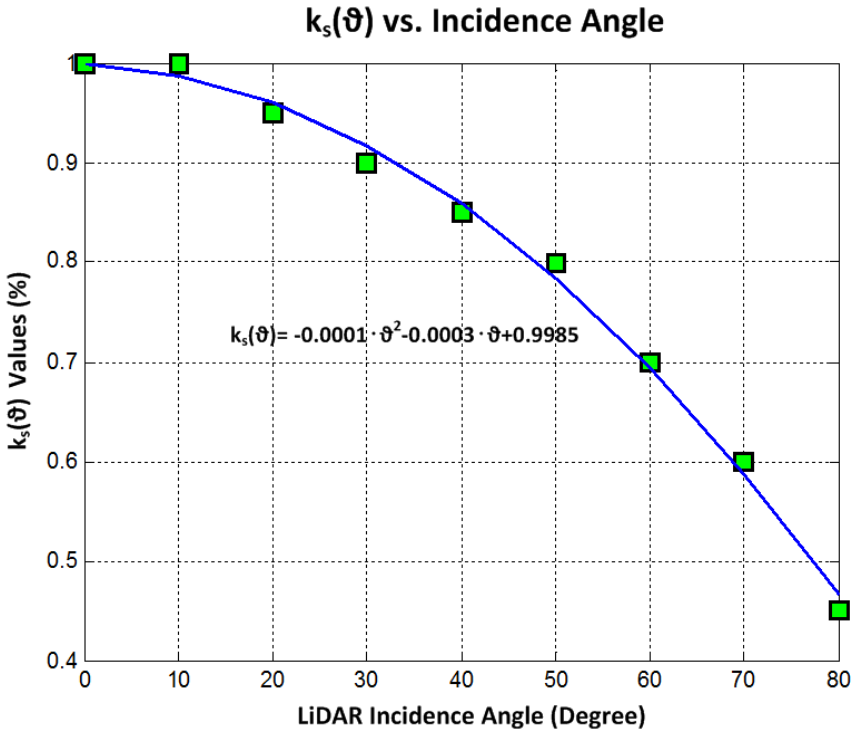

(b)

Figure 4-9 Modeling the relationship between k_s and incidence angle

By combining the model established for the beam distance and the incidence angle, the normalization function can be derived. The raw retro-intensity values acquired by the LiDAR system can be normalized using the generated retro-intensity normalization. In this study, the curves were generated using Type 1 sheeting. Different sheeting types and different LiDAR models might introduce different retro-intensity relationships that are different from this study. Nevertheless, following a similar process, additional curves can be generated for other types of sheeting and LiDAR models.

4.2.3.2. Beam Distance and Incidence Angle Computation for Sign Associated LiDAR Point Cloud

To conduct the LiDAR retro-intensity value normalization, the beam distance and incidence angle for each LiDAR point should be obtained. Figure 4-10 shows the flow for obtaining beam distance and incidence angle for each LiDAR point.

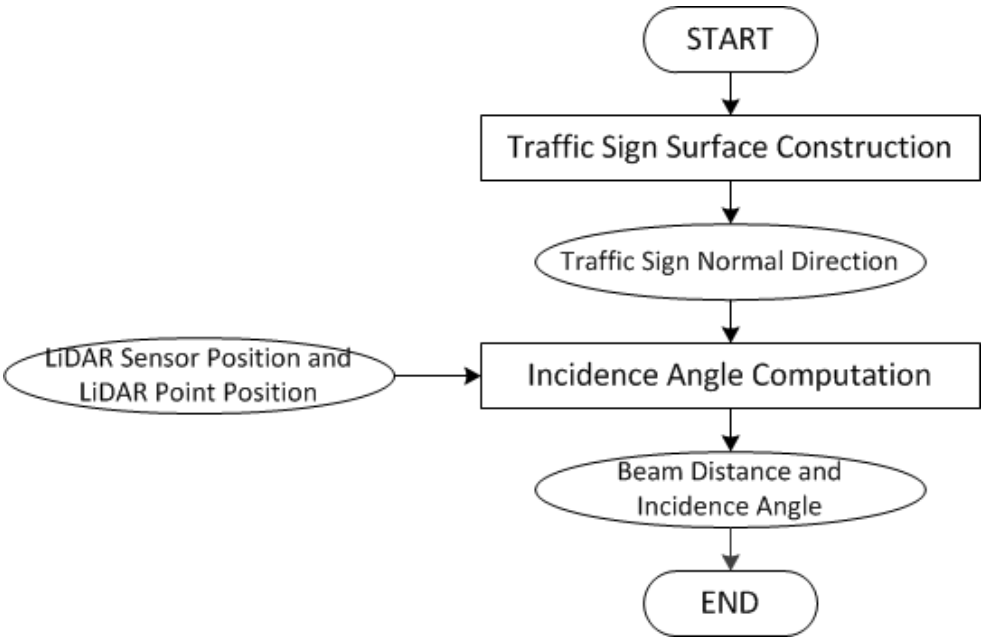

Figure 4-10 Flow for determining LiDAR point beam distance and incidence angle

Based on the results from section 4.2.2.2, the LiDAR point cloud that is associated with each detected traffic sign is extracted. Using such a LiDAR point cloud, the normal direction of the corresponding traffic sign surface can be obtained using the

PCA method in the ECEF reference system, as presented in Section 4.2.2.1.3. As the LiDAR sensor position and the position for each LiDAR point within the corresponding point cloud can be obtained based on the result from section 4.2.2.1.2, the direction of each laser beam can be obtained in the ECEF reference system. Therefore, the incidence angle of the each LiDAR point can be obtained using the following equation:

$$\alpha = \arccos\left(\frac{\langle \vec{p}, \vec{n} \rangle}{\|\vec{p}\| \|\vec{n}\|}\right)$$

where $\vec{p}$ is the direction of the laser beam, $\vec{n}$ is the normal direction of the traffic sign surface, and $\langle \vec{p}, \vec{n} \rangle$ is the product of the two direction vector. The beam distance can be directly read from the LiDAR point data. With the obtained beam distance and incidence angle, the retro-intensity value corresponding to this LiDAR point can be normalized using the normalization equation derived from section 4.2.3.1.

4.2.4. STEP 5 - Traffic Sign Retroreflectivity Condition Assessment

The last step is retroreflectivity condition assessment. The objective of this step is to determine the retroreflectivity condition based on the population of the normalized retro-intensity values obtained from the previous steps for each color of the detected traffic signs. The key component in this step is to establish a model that depicts the relationship between the retroreflectivity values measured using handheld retroreflectometer and the normalized retro-intensity values.

To establish the model with the help of GDOT signing maintenance office, a lab test was conducted by measuring both of red and white colors in 15 Type 1 engineer grade stop signs with various retroreflectivity conditions (including 5 brand new signs and 10 different in-service signs). The LiDAR point clouds for each traffic sign were collected using the sensing van. Based on registration results from Step 3 presented in Section 4.2.3, the location of each LiDAR point can be projected to the traffic sign surface. Figure 4-11 shows the registration result of the LiDAR points on the traffic sign surface in 3D space. At each LiDAR point location, the corresponding handheld

retroreflectometer measurement was conducted. To accurately match the location where the LiDAR point is collected and the location where the retroreflectometer is measured, the layout of the LiDAR point for each sign was sketched on the actual sign surface. At each location, three measurements were conducted using small apertures provided by the manufacturer, and the average of the four measurements was used to represent the actual retroreflectivity of this point.

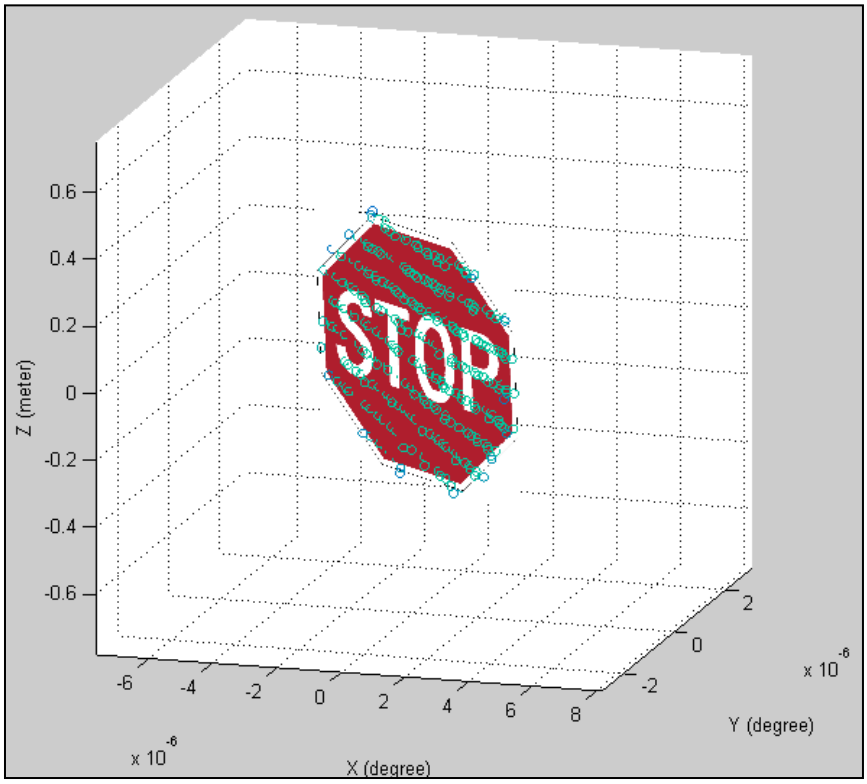

Figure 4-11 Registration result of the LiDAR points on the traffic sign

For all of the 15 traffic signs, there were 1123 pairs of measurements conducted to establish the correlation between the normalized retro-intensity values and the retroreflectivity values. The retroreflectivity values ranged between 0 mcd/m^2/lux and 64 mcd/m^2/lux, while the retroreflectivity of the typical Type 1 engineer grade sheeting is between 0 mcd/m^2/lux and 70 mcd/m^2/lux. Figure 4-12 shows the correlation between the retroreflectivity and the normalized retro-intensity. The blue points represent the actual paired measurements, while the red line represents the linear regression results of the

measurements. Based on this specific lab test, the regression results can be derived from the following equation:

$$Retroreflectivity_{EST} = -285.9 + 392.3 \times RetroIntensity_{NORM}$$

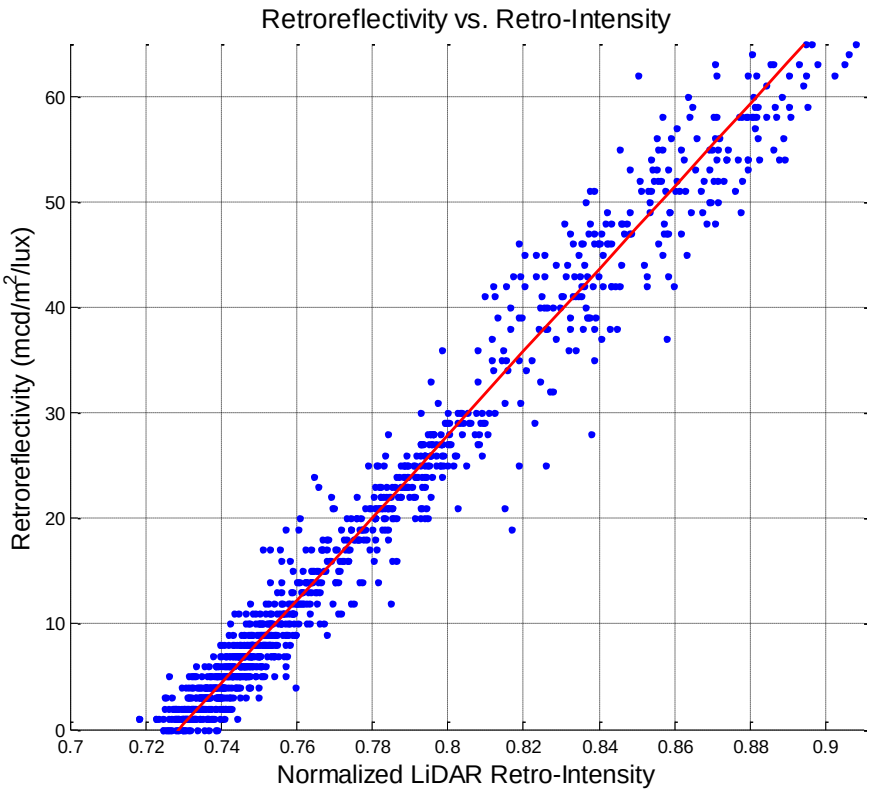

Figure 4-12 Correlation between the retroreflectivity and the normalized retro-intensity

Using the linear regression equation, each normalized retro-intensity value can be estimated as the corresponding retroreflectivity value. Therefore, for each traffic sign, the population of the normalized retro-intensity values measured from the LiDAR can be translated into the population of the retroreflectivity values, which is used to determine the retroreflectivity condition of the traffic sign. To make a consistent comparison with the current measurement method (i.e. handheld retroreflectometer), the median value of the population of the estimated retroreflectivity is used to represent the whole population (i.e. tested color) without being biased by some outliers. It is noted that there is a chance that the median of the estimated retroreflectivity values can be below zeros following the regression result, which does not realistically represent the true values. Therefore, for all

the medians of the estimated retroreflectivity values that are below zero, zero values are assigned. By comparing the estimated retroreflectivity of the whole population with the requirements defined in the MUTCD for different colors, the "FAIL" and "PASS" condition can be determined. Section 5.2 in Chapter 5 presents the detailed results and the discussion about the drawbacks of current retroreflectometer measurement methods.

It should be noted that the normalization curve (in Section 4.2.3) and the correlation curve between the normalized LiDAR retro-intensity values and the measured retroreflectivity values (in Section 4.2.4) are based on the specific LiDAR model (i.e. Riegl LMS-Q120i.) in response to the studied material (i.e. Type 1 engineer grade sheeting) used in this study. Different LiDAR models and different studied material could introduce completely different correlations. Further investigations on different LiDAR models (e.g. different beam spectrums, different beam divergence, etc.) and on different sheeting types (e.g. diamond grade, prismatic, etc.) are recommended for future research. Following the same methods and scheme proposed in this methodology, optimal correlations are expected to be derived accordingly.

CHAPTER 5

EXPERIMENTAL TEST

A comprehensive experimental test was conducted to validate the proposed methodologies for the enhanced traffic sign detection and the mobile traffic sign retroreflectivity condition assessment. For each methodology, both the individual algorithms and the complete methodology were tested using both lab and field tests.

5.1. Experimental Test for the Enhanced Traffic Sign Detection Methodology

In the experimental test for the enhanced traffic sign detection methodology, two focused tests were conducted to validate the performance of the two individual algorithms, only focusing on the color segmentation step and the shape detection step respectively. Datasets were purposely designed to include the challenging cases for the two algorithms to reveal the improvement of the enhanced algorithms. Then, a general test was conducted using containing five datasets with different road functions, data collection sources, and data qualities to comprehensively validate the overall performance of the complete methodology.

5.1.1. Focused Test for the LD-SCM-Based Color Segmentation Algorithm

A focused test was conducted to evaluate the accuracy of the proposed lighting dependent statistical color model (LD-SCM)-based color segmentation algorithm. The testing dataset was collected on I-285 and SR-275 and included different lighting conditions, e.g. over-exposure, under-exposure, normal exposure, and adverse lighting conditions. To acquire these lighting conditions, different driving directions, times of the day, and weather conditions were considered. Overall, 890 signs containing eight

different colors were manually extracted, and the corresponding pixels extracted from traffic signs under different lighting conditions were manually marked with the corresponding Manual of Uniform Traffic Control Devices (MUTCD) colors as the ground truth. More than 8 million pixels were collected for this focused test.

The result of the proposed LD-SCM-based color segmentation algorithm was compared with the existing color segmentation algorithm (Tsai et al., 2009). The pixels were processed by the existing color segmentation algorithm and the proposed LD-SCM-based color segmentation algorithm. The confusion matrices are shown in Table 5-1 and Table 5-2.

Table 5-1 Confusion matrix for the color segmentation results using the existing algorithm

	White	Black	Green	Blue	Red	Yellow	Orange	FYG
White	0.7676	0.1455	0.0003	0.0000	0.0080	0.0780	0.0006	0.0000
Black	0.0878	0.6207	0.0703	0.0040	0.0924	0.1082	0.0142	0.0024
Green	0.0143	0.1391	0.6128	0.1707	0.0004	0.0023	0.0007	0.0597
Blue	0.0327	0.1505	0.1531	0.6633	0.0000	0.0000	0.0000	0.0004
Red	0.0985	0.0855	0.0000	0.0000	0.7084	0.0182	0.0884	0.0010
Yellow	0.0419	0.0947	0.0030	0.0000	0.0064	0.7601	0.0757	0.0182
Orange	0.0007	0.0396	0.0000	0.0000	0.1062	0.1542	0.6893	0.0100
FYG	0.0206	0.0534	0.0100	0.0003	0.0081	0.0414	0.0021	0.8641

Table 5-2 Confusion matrix for the color segmentation results using the proposed LD-SCM algorithm

	White	Black	Green	Blue	Red	Yellow	Orange	FYG
White	0.9611	0.0136	0.0060	0.0014	0.0084	0.0043	0.0052	0.0000
Black	0.0109	0.8245	0.0046	0.0071	0.0501	0.0906	0.0082	0.0040
Green	0.0118	0.0266	0.9491	0.0125	0.0000	0.0000	0.0000	0.0000
Blue	0.0071	0.0400	0.0024	0.9502	0.0000	0.0000	0.0000	0.0003
Red	0.0434	0.0405	0.0001	0.0006	0.9007	0.0076	0.0071	0.0000
Yellow	0.0096	0.0341	0.0001	0.0078	0.0123	0.9118	0.0238	0.0005
Orange	0.0000	0.0102	0.0000	0.0000	0.0647	0.0648	0.8603	0.0000
FYG	0.0015	0.0039	0.0057	0.0053	0.0000	0.0088	0.0089	0.9659

By comparing the results from both algorithms, it can be observed that the proposed LD-SCM-based color segmentation algorithm dramatically improves the performance of the existing algorithm by reducing the color confusion caused by the distortion of different lighting conditions as described below:

- **Distortion caused by under-exposure or adverse lighting conditions.** In the existing color segmentation algorithm, 14.55% of the white pixels, 13.91% of the green pixels, and 15.05% of the blue pixels are falsely segmented as black pixels. By identifying these lighting conditions and applying the new LD-SCM, only 1.36% of the white pixels, 2.66% of the green pixels and 4% of the blue pixels are still falsely segmented as black pixels (highlighted with yellow in Table 5-1 and Table 5-2).
- **Distortion caused by over-exposure condition.** In the existing color segmentation algorithm, 8.78% of the black pixels and 9.85% of the red pixels are falsely segmented as white pixels. By identifying such lighting condition and applying the new LD-SCM, only 1.09% of the black pixels and 4.34% of the red pixels are still falsely segmented as white pixels (highlighted in blue in Table 5-1 and Table 5-2).
- **Distortion caused by under-exposure or over-exposure conditions.** In the existing color segmentation algorithm, more than 15% of the blue and the green pixels are confused with each other, while more than 25% of the orange pixels are confused with each red or yellow. By identifying these lighting conditions and applying the new LD-SCM, less than 2% of the blue or green pixels are confused with each other, and less than 13% of the orange pixels are falsely segmented as red or yellow pixels (highlighted as pink in Table 5-1 and Table 5-2).

5.1.2. Focused Test for the ODE/PDE-Based Shape Detection Algorithm

A focused test was conducted to evaluate the performance of the proposed ordinary/partial differential equation (ODE/PDE)-based shape detection algorithm with discontinuous image boundaries in cluttered backgrounds. Twenty-six images with cluttered backgrounds and discontinuous boundary problems were tested by simultaneously running both the active contour and active polygon algorithms. These images could not be detected previously using the existing sign detection system (Tsai et al., 2009) and led to false negatives.

For the proposed active contour algorithm, of the 26 images, 24 images were correctly detected by the proposed active contour. Figure 5-1 shows an example of the results. From left to right, Figure 5-1 shows the original image, the color-segmented image, the extracted contour using existing system, the polygon detection result using the existing system, the extracted contour using the proposed active contour algorithm, and the polygon detection result using the enhanced system with active contour algorithm incorporated.

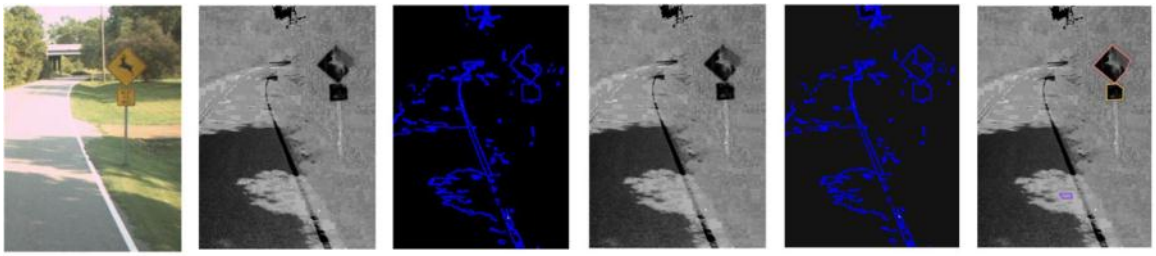

1 2 3 4 5 6

Figure 5-1 Comparison of the processed images obtained using the existing sign detection system and the proposed active contour algorithm. 1. Original video log image; 2. Color segmented image; 3. Extracted contour using the existing system; 4. Detection result using existing system; 5. Extracted contour using the proposed active contour algorithm; 6. Detection result using the enhanced system

The proposed active contour algorithm performs well in detecting traffic signs that have discontinuous boundary problems, although there are two cases in which the proposed active contour algorithm cannot detect signs correctly. Figure 5-2 shows two cases that cannot be detected correctly using active contour algorithm. In Figure 5-2(a), the original image has a similar foreground and background in the color space, which causes undistinguished color segmentation. When the proposed active contour algorithm is applied in that area, the contour region expands unwillingly. Figure 5-2(b) shows that the proposed active contour algorithm extracts the traffic sign boundary, except the upper portion because the contour evolves into part of the legend area. This occurs because, after the color segmentation, the upper portion of the boundary is decomposed as a different color from the rest of the boundary.

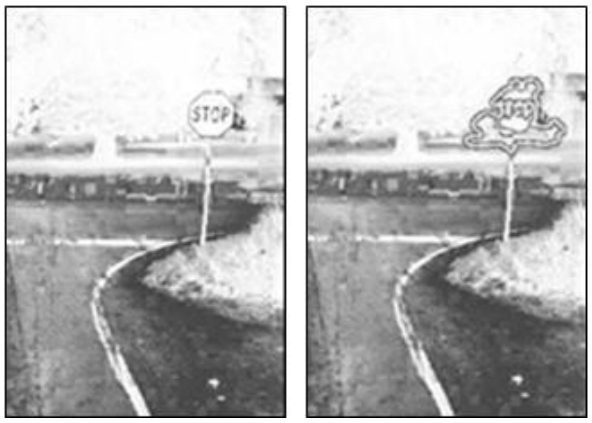

(a)

(b)

Figure 5-2 False negative cases using the active contour algorithm

For the proposed active polygon algorithm, all of the 26 images are correctly detected, including the two cases that could not be detected by the active contour algorithm, as shown in Figure 5-3. The results of testing both the proposed active contour algorithm and the active polygon algorithm show that the active polygon algorithm has better performance for detecting traffic signs with discontinuous boundaries. In addition, by constraining the movement only by limited number of vertices, the proposed active polygon algorithm performs approximately twice as fast as the proposed active contour algorithm. Nevertheless, both of the proposed active contour and active polygon algorithms out-perform the existing shape detection algorithm in detecting traffic signs containing discontinuous boundaries in cluttered backgrounds. Considering the performance and the processing speed, the active polygon-based shape detection algorithm was integrated into the final detection methodology.

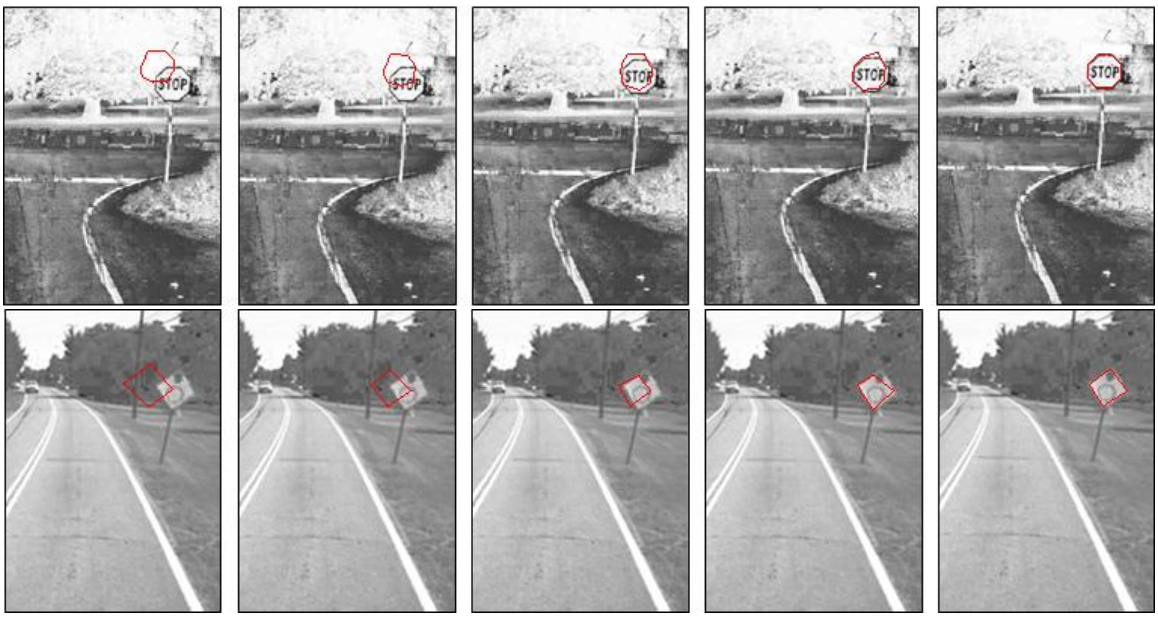

Figure 5-3 Active polygon algorithm detection result for the identified false negative cases

5.1.3. General Test

The objective of the general test is to comprehensively evaluate the performance of the complete methodology by integrating the individual enhanced algorithms. Datasets for the general test were first designed and collected, followed by comprehensive testing of the complete methodology.

5.1.3.1. Dataset Selection

In the process of testing dataset selection, an effort was made to cover different aspects that could comprehensively validate the performance of the complete methodology. The selected datasets consist of a rich diversity. Table 5-3 shows the detailed information for the selected datasets and reveals the following:

1) Three different roadway function levels were included to comprehensively cover different sign types and visual conditions, i.e. interstate, state routes, and local roads in both rural and urban areas;
2) Three different data sources were included to cover different image qualities and configurations, i.e. Louisiana Department of Transportation and Development (LaDOTD), the city of Nashville, and the sensing van at Georgia Tech;

3) Two identified challenging cases are included to fully assess the performance of the developed algorithm: changing lighting conditions and a cluttered background with discontinuous boundaries.

Table 5-3 List of the selected datasets for general test

#	Source	Location	Image	Sign
1	LaDOTD	SR-541, Westwego, LA	1547	303
2	City of Nashville	Cane Ridge Rd, Nashville, TN	607	133
3	Sensing Van	37th Street, Savannah, GA	933	475
4	Sensing Van	SR-67, Statesboro, GA	2216	392
5	Sensing Van	I-95, Savannah, GA	5623	875

LaDOTD dataset: The dataset from LaDOTD contains 1547 images collected on SR-541, Westwego, Louisiana (LA). In the 1547 images, there are 1244 negative images (i.e. without traffic signs) and 303 positive images (i.e. with traffic signs of different sizes, colors, shapes, and conditions). As provided by LaDOTD, the image quality is very good with a resolution of 1920x1080. The data was pre-processed by Roadware Corp, which was the contractor for the data collection. Therefore, most of the lighting condition issues had been already eliminated by the pre-processing. Figure 5-4 shows a sample image in this dataset.

Figure 5-4 Sample image in the LaDOTD dataset

City of Nashville dataset: The dataset from the city of Nashville contains 607 images collected on Cane Ridge Road, Nashville, Tennessee. In the 607 images, there are

474 negative images and 133 positive images. As provided by the city of Nashville, the image quality is reasonable with a resolution of 1300x1030. Figure 5-5 shows a sample image in this dataset.

Figure 5-5 Sample image in the city of Nashville dataset

37th Street dataset: The dataset from 37th Street, Savannah, Georgia, contains 933 images,. In the 933 images, there are 458 negative images and 475 positive images. Because they were collected by the sensing van developed at Georgia Tech, the image quality is very good, with a resolution of 2448x2048. Figure 5-6 shows a sample image in the dataset. This dataset is designed to incorporate the challenging cases of a severely cluttered background.

Figure 5-6 Sample image in the 37th Street dataset

SR-67 dataset: The dataset from SR-67 contains 2216 images collected on SR-67, in Statesboro, Georgia. In the 2216 images, there are 1824 negative images and 392

positive images. Using the Georgia Tech sensing vehicle, the data quality and resolution are similar for the data collected on 37th Street. Figure 5-7 shows a sample image in the dataset. This dataset is designed to incorporate the challenging case of changing lighting conditions.

Figure 5-7 Sample image in the SR-67 dataset

I-95 dataset: The dataset from I-95 contains 5623 images collected on I-95 in Savannah, Georgia. In the 5623 images, there are 4748 negative images and 875 positive images. Using the Georgia Tech sensing vehicle, the data quality and resolution are similar to the data collected on 37th Street. Figure 5-8 shows a sample image in the dataset.

Figure 5-8 Sample image in the I-95 dataset

5.1.3.2. Detection Results

Table 5-4(a) shows the overall detection results of the five selected datasets. In general, the results show that the enhanced algorithm, compared with the existing algorithm (Tsai et al., 2009), can reduce the false negative rates by 12.2%. The results also show that the enhanced algorithm, compared with the existing algorithm (Tsai et al., 2009), increases the false positive rate by only 1.7%. The detailed analysis for each individual dataset is discussed below based on the breakdown in Table5-4(b)-(f).

Table 5-4

(a) Overall detection results by the existing algorithm and the enhanced algorithm

	True Positive	True Negative	False Positive	False Negative
Existing algorithm	72.8% (1586/2178)	87.1% (7618/8748)	12.9% (1130/8748)	27.2% (592/2178)
Enhanced algorithm	85.0% (1852/2178)	85.4% (7472/8748)	14.6% (1276/8748)	15.0% (326/2178)

(b) Detection results on the LaDOTD dataset

	True Positive	True Negative	False Positive	False Negative
Existing algorithm	82.2% (249/303)	89.5% (1113/1244)	10.5% (131/1244)	17.8% (54/303)
Enhanced algorithm	91.7% (278/303)	87.9% (1094/1244)	12.1% (150/1244)	8.3% (25/303)

(c) Detection results on the City of Nashville dataset

	True Positive	True Negative	False Positive	False Negative
Existing algorithm	78.9% (105/133)	88.8% (421/474)	11.2% (53/474)	21.1% (28/133)
Enhanced algorithm	88.0% (117/133)	87.6% (415/474)	12.4% (59/474)	12.0% (16/133)

(d) Detection result on the 37th Street dataset

	True Positive	True Negative	False Positive	False Negative
Existing algorithm	53.9% (256/475)	68.1% (312/458)	31.9% (146/458)	46.1% (219/475)
Enhanced algorithm	72.0% (342/475)	72.9% (334/458)	27.1% (124/458)	28.0% (127/475)

(e) Detection result on the SR-67 dataset

	True Positive	True Negative	False Positive	False Negative
Existing algorithm	70.9% (278/392)	84.1% (1534/1824)	15.9% (290/1824)	29.1% (58/392)
Enhanced algorithm	85.7% (336/392)	83.7% (1527/1824)	16.3% (297/1824)	14.3% (/392)

(f) Detection result on the I-95 dataset

	True Positive	True Negative	False Positive	False Negative
Existing algorithm	79.8% (698/875)	89.3% (4238/4748)	10.7% (510/4748)	20.2% (177/875)
Enhanced algorithm	89.0% (779/875)	86.4% (4102/4748)	13.6% (646/4748)	11.0% (125/875)

- The enhanced algorithm improves the most for the 37th Street dataset in terms of reducing the false negative rate. The existing algorithm can only detect 53.9% of the signs in the 37th Street dataset due to the discontinuous boundaries produced by the severely cluttered backgrounds, while the enhanced algorithm can detect 72.0% of the

signs correctly. The newly detected signs contain discontinuous boundaries produced by the tree shadows and complex backgrounds. The edge-based shape detection method in the existing algorithm produces excessive false edges within and across the boundaries of the traffic signs. Therefore, the shape approximated in the subsequent step fails to formulate a complete sign shape. On the contrary, the proposed active polygon method in the enhanced algorithm is a region-based method that dictates the average intensity changes in and out of the polygon region. Therefore, as the false edges contribute minimal changes to the average intensity, the proposed method is immune to such discontinuous boundaries. Figure 5-9 shows an example that could not be detected using the existing method.

Figure 5-9 Challenging case due to the casting tree shadow
(Left: color segmented image; right: original image)

- The enhanced algorithm improves the SR-67 dataset, which contains lighting condition issues (i.e. adverse lighting), the most. The existing algorithm can only detect 70.9% of the signs in the dataset due to the lighting condition issues, while the enhanced algorithm can detect 85.7% of the signs. Most of the newly detected signs are in the adverse lighting condition. The existing color model tends to cluster all the dark pixels as black pixels, regardless of the subtle color information in these dark pixels. On the contrary, the new color models in the enhanced system classify different lighting conditions first and then cluster the colors within each lighting

condition category. Therefore, the subtle difference in the dark pixels can be dictated more precisely. Figure 5-10 shows an example of the segmentation results.

Figure 5-10 Detection results using 1) the existing algorithm and 2) the enhanced algorithm

- The enhanced algorithm can consistently improve the performance of the existing algorithm on the datasets containing different roadway function levels (i.e. different sign types and visual conditions) and data collection sources (i.e. different data qualities, resolutions, etc.). Within the selected datasets, there are more than 200 types of signs with nine shapes and eight colors, and with different visual conditions. The enhanced algorithm reduces the false negative rate in the existing algorithm by 9.0% to 18.1%. The enhanced algorithm demonstrates slightly better results on the LaDOTD dataset because of the pre-processing conducted by Roadware Corp. Further performance improvement is expected if similar pre-processing steps are applied to the rest of the datasets. Currently, the pre-processing algorithm is proprietary by Roadware Corp., but customizing the pre-processing algorithm that can be incorporated into the enhanced algorithm is recommended for future research.
- The enhanced algorithm does not excessively increase the false positive rate and effectively reduces the false negative rate. In some cases, the false positive rate can be reduced by the enhanced algorithm, e.g. 37th Street dataset. In the 37th Street dataset, the existing algorithm falsely detected many tree shadows as traffic signs. The shape approximation step of the existing algorithm assembles the detected contours into shapes based on the extracted edges. Since many false edges were produced by the

spotty tree shadows, many false shapes were formulated. Figure 5-11 shows an example of the false shapes detected using the existing method. On the contrary, the proposed algorithm uses the generalized Hough transform (GHT) algorithm to identify the shapes. Although the edge information is still used, the neighboring edges are considered as a whole based on the shape template rather than individually, and then they are ranked by a global accumulator. Therefore, the false edges that are not associated with the polygons initialized by the GHT algorithm do not impact the final result.

Figure 5-11 An example of the false shapes detected using the existing method

From the test results on the selected datasets, the enhanced methodology demonstrates, overall, good capability to detect traffic signs under variant conditions while, also, showing strong capabilities to detect traffic signs that were challenging to the existing algorithm. However, there are still some false negative cases and false positive cases that are produced by the enhanced algorithm, which can be improved by further research. Three types of false negative cases were identified in the test using the enhanced algorithm, including severe casting shadow, occlusion, and several specific signs.

As shown in Figure 5-12, casting shadows distort the color in part of the sign surface, which destroys the integrity of the sign in the color segmentation result. The broken pieces will be hard to be detected even using the enhanced algorithm. A severe

casting shadow issue is identified as the most frequent false negative case through the experimental test. There are 56.7% of the false negative cases identified in the experimental test are due to this issue. This type of false negative case can be reduced by introducing the fuzzy color segmentation approach. Using the fuzzy logic, each pixel can be assigned with multiple MUTCD-defined colors instead of a single color according to the likelihood. By assigning multiple colors to each pixel, the color fragments broken by the casting shadows can be reunited as a complete traffic sign shape when one of the colors assigned to the fragment matches another fragment.

Figure 5-12 False negative cases due to severe casting shadow
(Left: original image; right: color segmented image)

As shown in Figure 5-13, like the casting shadow cases, the integrity of the sign is destroyed by the obstruction. The unique color and shape patterns of the traffic sign will not be maintained. There are 26.5% of the false negative cases identified in the experimental test are due to this issue. This type of false negative case can be reduced by relaxing the shape constraints used in the proposed generalized Hough transform (GHT). By relaxing the shape constraints, part of the occluded sign shape can still be identified. However, the relaxation may introduce more false positive cases because more irregular shapes might still be qualified as sign shape candidates. When the occlusion is so severe that almost all of the important information for a sign is diminished, it becomes extremely hard to detect it using any advanced algorithm.

Figure 5-13 False negative cases due to occlusion
(Left: original image; right: color segmented image)

As shown in Figure 5-14, the no-parking sign and the object marker sign are the two types of specific signs that are frequently undetected. For the no-parking sign, the complex legend segments the sign into tiny blocks (i.e. the no-parking signs are the smallest type of signs), which can be very easily merged into background after the segmentation. For the object marker signs, the yellow-black pattern of this type of sign fragments the sign into different color blocks, and there is no clear boundary by which the sign can be defined. There are 12.1% of the false negative cases identified in the experimental test are due to this issue. These cases can be potentially minimized by applying a shape-merging algorithm to combine the individual pieces into a regular sign shape, or directly introducing specific traffic sign recognition algorithms to recognize the unique pictogram of the signs.

Figure 5-14 Several specific types of signs undetected
(Left: original image; right: color segmented image)

Several types of false positive cases are identified in the test using the enhanced methodology, including house windows, commercial signs, the back of signs, vehicle parts, etc. The color features and shape features are used in the enhanced methodology.

However, sometimes these two features are not sufficient for traffic signs to be distinguished from other objects, as there are many other objects sharing characteristics similar to the traffic signs in terms of color and shape. Figure 5-15 shows some of the examples of the identified false positive cases. Some of the false positive cases can be rejected by identifying their locations if GPS data is available during the data collection, e.g. on the pavement, etc. By integrating different traffic sign features for each detected traffic sign candidate, e.g. color, shape, location, etc., a confidence score can be designed to represent the quality of the detection. Therefore, the false positive cases can be systematically reduced by determining a robust confidence level.

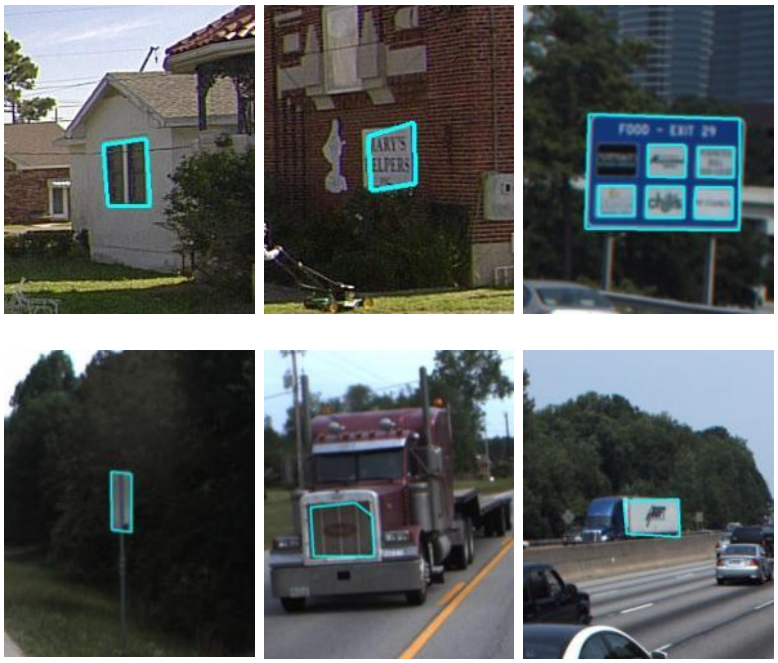

Figure 5-15 False positive cases identified for the enhanced algorithm

5.2. Experimental Test for the Proposed Traffic Sign Retroreflectivity Condition Assessment Methodology

In the experimental test for the proposed traffic sign retroreflectivity condition assessment methodology, a lab test with a controlled environment was first conducted to study the fundamental characteristics of light detection and ranging (LiDAR) retro-intensity measurement, including the repeatability of consecutive scans, the impact of

ambient lighting, and the impact of beam distance and incidence angle. Then, field test containing 35 Type 1 engineer grade stop signs was conducted to validate the overall performance of the proposed methodology and evaluate the feasibility of its application in state departments of transportation's (DOTs') practices. The dataset was purposely selected to include the most important traffic sign type that is related to roadway safety, and the most important traffic sign sheeting type that is the most frequent failed traffic sheeting type in service due to the retroreflectivity condition.

5.2.1. Lab Test for Studying Fundamental Characteristics of LiDAR Retro-Intensity Measurement

This section presents the laboratory tests that were conducted in a controlled environment to study the key characteristics of the LiDAR retro-intensity measurement. These key characteristics are closely related to the feasibility of applying LiDAR retro-intensity values for traffic sign condition assessment. Repeatability of the retro-intensity measurement, the impact of ambient lighting conditions, and the impact of LiDAR beam distance and incidence angle are studied through the three designed lab tests.

5.2.1.1. Repeatability of the Retro-Intensity Measurement

To conduct traffic sign condition assessment with consistent results, it is important to validate the repeatability of the retro-intensity measurement on the same retro-reflective objects. Only when the measurement is consistent through successive LiDAR scans (having minimal variance) is it feasible to use LiDAR for consistent retroreflectivity condition assessment.

A blank white traffic sign sample with brand new, Type 1 engineer grade sheeting was used for the test. The sample was attached to a static platform 2 ft. from the road edge, as shown in Figure 5-16, while the LiDAR device was stationary at a 41 ft. distance from the surface of the sample. To study the repeatability of continuous scans and the repeatability of different scans, two scenarios were created in the test: 1) continuous

scanning for ten minutes, using the first scan at the beginning of each minute for repeatability assessment; 2) discretely triggering one scan at the beginning of each minute for ten minutes with the LiDAR device remaining idle between consecutive triggers.

Figure 5-16 Repeatability test conducted using white Type 1 sheeting on campus

Table 5-5 shows the repeatability under the two designed scenarios. It can be observed that both the continuous scanning and discrete triggering scenarios showed good repeatability, i.e. standard deviation of the measurement among ten scans is smaller than 0.0003. As discussed in the section 4.2.4, the standard deviation of 0.0003 can potentially introduce less than ±0.1 mcd/m^2/lux, which is ignorable in the process of sign retroreflectivity condition assessment.

Table 5-5 Repeatability results using two designed scenarios

Minute #	Scenario 1	Scenario 2
1	0.78304	0.78315
2	0.78250	0.78277
3	0.78305	0.78280
4	0.78296	0.78274
5	0.78321	0.78224
6	0.78296	0.78252
7	0.78262	0.78278
8	0.78263	0.78300
9	0.78253	0.78265
10	0.78297	0.78254
Std. Dev.	0.00025	0.00026

5.2.1.2. Impact of Ambient Lighting Condition

As the data acquisition is complete during the daytime, it is important to quantify the impact of ambient lighting condition on the LiDAR retro-intensity measurement. Only during daytime with different ambient lighting conditions when the LiDAR retro-intensity measurement is not sensitive to the intensity of ambient lighting condition is it feasible to use LiDAR for consistent retroreflectivity condition assessment. A standard 36x36 stop sign sample with brand new Type 1 engineer grade sheeting was used for this test. The sample was attached to a static platform in the laboratory, as shown in Figure 5-17, and the LiDAR device was placed so that it was stationary at a 41 ft. distance from the surface of the sample. With the current configuration, 64 points were collected within each LiDAR scan. As shown in Figures 5-17(a) and (b), the light was switched on and off to simulate two different lighting conditions (i.e. regular ambient lighting and darkness). The first scan under each lighting condition was used to represent the corresponding scanning result.

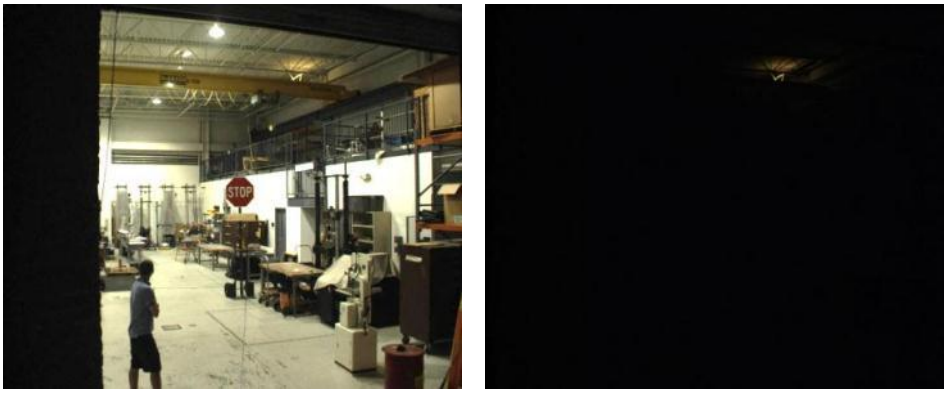

(a) **(b)**

Figure 5-17 Ambient lighting condition tests in lab

Figure 5-18 shows the results from the single scan with the light switched on and off. It is observed that the LiDAR retro-intensity measurements are very close with the light switched on and off. When the light is off, the measurements are slightly smaller than when the light is switched on at the scale of 0.0002. As discussed in the following sections (4.2.4), the standard deviation of 0.0002 can potentially introduce less than

±0.08 mcd/m^2/lux, which is even less than the variance of the successive scans. Therefore, the impact of the ambient lighting condition is ignorable in the process of traffic sign retroreflectivity condition assessment.

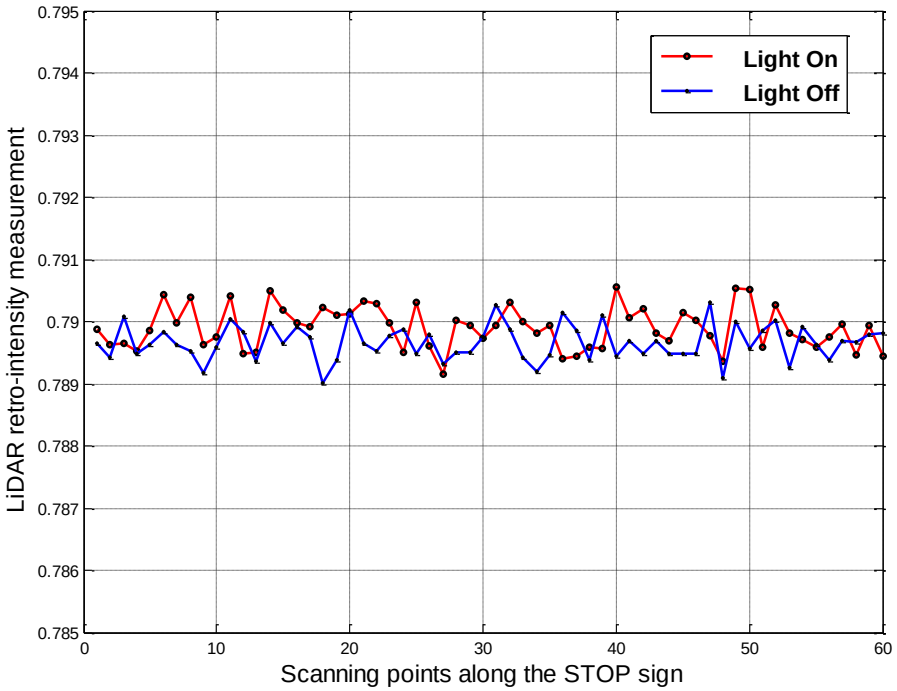

Figure 5-18 Result of the ambient lighting condition test

5.2.2. Field Test for Traffic Sign Retroreflectivity Condition Assessment

A field test was conducted to assess the accuracy of the proposed LiDAR-based traffic sign retroreflectivity condition assessment method. Thirty-five stop signs with Type 1 engineer grade sheeting were collected in a community in a city from Georgia in support of this test. Ground truth was established using the Delta GR3 handheld retroreflectometer following the American Society for Testing and Materials (ASTM) E1709 standard (2009). Using the handheld retroreflectometer, four readings of each sign color were collected; the median of the four readings represents the retroreflectivity of the measured color. A visual inspection method following the recommendations proposed in the MUTCD was used to validate the results. Figure 5-19 shows the map of the data collection site and the corresponding location of the stop signs.

Figure 5-19 Sites for the general traffic sign retroreflectivity condition assessment test

5.2.2.1. Image-LiDAR Registration Result

The accuracy of the proposed image-LiDAR registration algorithm was evaluated first using the collected stops signs. The bounding boxes from the LiDAR point cloud that are associated with the tested stops signs were manually digitized, each of which was represented by a 3D polygon. Using the proposed registration method, each 3D polygon can be projected into the corresponding 2D image. The projected polygons were compared with the original detection results (i.e. bounding boxes derived from Step 1 and 2 in Section 4.2.2). Figure 5-20 illustrates three example of the comparison result for Signs #17, #27 and #33. The traffic shown in the figures represents the detected results, while the red polygons represent the projected results. As shown in Figure 5-20, there are very few points that could not be correctly projected due to the measurement outliers for the LiDAR sensor that could not be eliminated using co-planar validation, as presented in Section 4.2.2.1.3. The result shows that the developed registration method can accurately register the 3D LiDAR point cloud with the 2D video log images.

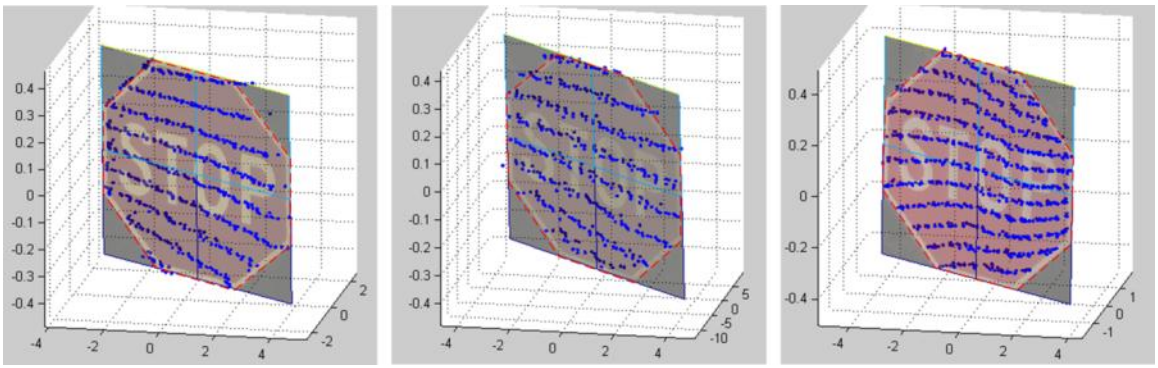

Figure 5-20 Illustrations of the registration results for Sign #17, #27 and #33

By comparing the projected polygon and the detected traffic sign polygon in detail, the average offset is less than two pixels along the boundary's normal direction. Such pixel offset represents no more than a ½ inch geometrical offset on the tested traffic sign surfaces. To conservatively estimate the traffic sign retroreflectivity conditions for each sheeting color, all the projected LiDAR points that are close to the boundary of different colors (i.e. less than ½ inch) will be removed from the subsequent computation.

5.2.2.2. Retroreflectivity Condition Assessment Result

Figure 5-21 shows the overall result for the 35 stop signs, including the assessment for both the red and white colors. The blue dots represent the actual results of the estimated retroreflectivity using LiDAR retro-intensity values vs. the ground truth values measured from the handheld retroreflectometer. The red line represents the ideal result between the estimation and the ground truth, while the blue-dashed line represents the actual correlation. It can be observed that the estimations align well with the ground truth, although some of the estimates over or under-estimate the truth retroreflectivity values as recorded in the ground truth. Nevertheless, as each ground truth only contains four measurements using the handheld retroreflectometer, measurement bias could be inherited when collecting ground truths. Therefore, further investigation for determining the traffic sign retroreflectivity condition for each color was done instead of just comparing the absolute measurement values.

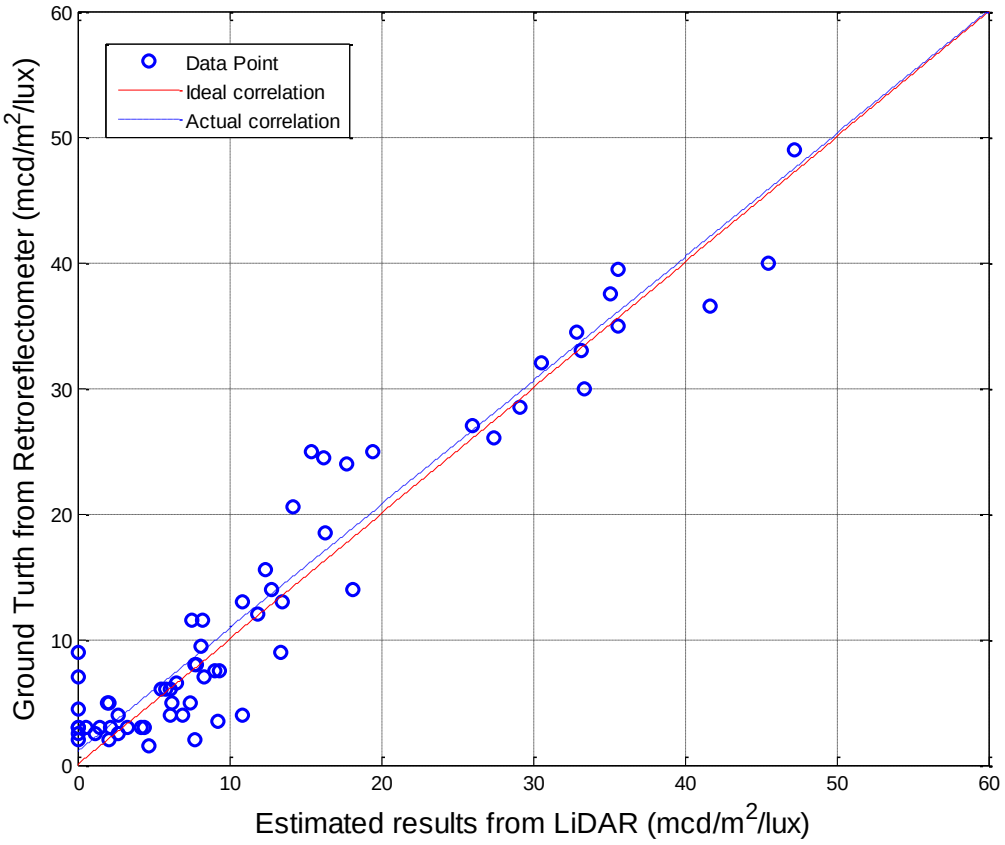

Figure 5-21 Correlation results between the estimated retroreflectivity and ground truth

Table 5-6 shows the detailed results for the 35 stop signs, including the condition assessment for both red and white colors. By applying the proposed minimum retroreflectivity standard defined in the MUTCD, if the retroreflectivity measurement is smaller than 7 mcd/m^2/lux for red and/or 35 mcd/m^2/lux for white, respectively, the corresponding traffic sign is in "FAIL" retroreflectivity condition, while in a "PASS" condition otherwise.

Table 5-6 Testing result for both the background and legend colors of the 35 stop signs

#	Red (Background Color)					White (Legend Color)				
	Retroreflectivity			Condition		Retroreflectivity			Condition	
	Handheld	Est.	Diff.	Handheld	Est.	Handheld	Est.	Diff.	Handheld	Est.
1	4.0	2.7	-1.3	FAIL	FAIL	26.0	27.4	1.4	FAIL	FAIL
2	3.0	4.2	1.2	FAIL	FAIL	4.5	0.0	-4.5	FAIL	FAIL
3	6.0	5.5	-0.5	FAIL	FAIL	37.5	35.1	-2.4	PASS	PASS
4	9.5	8.1	-1.4	PASS	PASS	78.0	72.4	-5.6	PASS	PASS
5	3.0	0.6	-2.4	FAIL	FAIL	20.5	14.2	-6.3	FAIL	FAIL
6	14.0	12.8	-1.2	PASS	PASS	70.5	66.4	-4.1	PASS	PASS
7	8.0	7.7	-0.3	PASS	PASS	28.5	29.1	0.6	FAIL	FAIL
8	6.0	6.1	0.1	FAIL	FAIL	33.0	33.2	0.2	FAIL	FAIL
9	4.0	6.9	2.9	FAIL	FAIL	36.5	41.7	5.2	PASS	PASS
10	3.0	2.2	-0.8	FAIL	FAIL	14.0	18.1	4.1	FAIL	FAIL
11	7.0	8.3	1.3	PASS	PASS	32.0	30.6	-1.4	FAIL	FAIL
12	3.0	3.3	0.3	FAIL	FAIL	18.5	16.3	-2.2	FAIL	FAIL
13	3.0	0.0	-3.0	FAIL	FAIL	3.5	9.2	5.7	FAIL	FAIL
14	3.0	0.0	-3.0	FAIL	FAIL	1.5	4.7	3.2	FAIL	FAIL
15	2.5	2.7	0.2	FAIL	FAIL	11.5	8.2	-3.3	FAIL	FAIL
16	13.0	10.9	-2.1	PASS	PASS	61.0	65.7	4.7	PASS	PASS
17	5.0	7.4	2.4	**FAIL**	**PASS**	15.5	12.4	-3.1	FAIL	FAIL
18	6.0	5.8	-0.2	FAIL	FAIL	25.0	15.4	**-9.6**	FAIL	FAIL
19	4.0	10.9	6.9	**FAIL**	**PASS**	24.0	17.7	-6.3	FAIL	FAIL
20	5.0	6.2	1.2	FAIL	FAIL	8.0	7.8	-0.2	FAIL	FAIL
21	2.5	1.2	-1.3	FAIL	FAIL	7.5	9.0	1.5	FAIL	FAIL
22	2.0	7.7	5.7	**FAIL**	**PASS**	24.5	16.2	**-8.3**	FAIL	FAIL
23	7.0	0.0	-7.0	**PASS**	**FAIL**	13.0	13.5	0.5	FAIL	FAIL
24	2.0	2.1	0.1	FAIL	FAIL	5.0	2.0	-3.0	FAIL	FAIL
25	12.0	11.9	-0.1	PASS	PASS	63.5	62.9	-0.6	PASS	PASS
26	2.0	0.0	-2.0	FAIL	FAIL	34.5	32.9	-1.6	FAIL	FAIL
27	6.5	6.5	0.0	FAIL	FAIL	25.0	19.4	-5.6	FAIL	FAIL
28	3.0	1.5	-1.5	FAIL	FAIL	9.0	13.4	4.4	FAIL	FAIL
29	11.5	7.5	-4.0	PASS	PASS	49.0	47.2	-1.8	PASS	PASS
30	7.5	9.3	1.8	PASS	PASS	35.0	35.6	0.6	PASS	PASS
31	5.0	2.1	-2.9	FAIL	FAIL	27.0	26.0	-1.0	FAIL	FAIL
32	3.0	0.0	-3.0	FAIL	FAIL	40.0	45.5	5.5	PASS	PASS
33	4.0	6.1	2.1	FAIL	FAIL	30.0	33.4	3.4	FAIL	FAIL
34	9.0	0.0	-9.0	**PASS**	**FAIL**	39.5	35.6	-3.9	PASS	PASS
35	2.5	0.0	-2.5	FAIL	FAIL	3.0	4.4	1.4	FAIL	FAIL

A false positive case is defined as a “PASS” condition if mistakenly identified as a “FAIL” condition, while a false negative case is defined as a “FAIL” condition if mistakenly identified as a “PASS” condition. In this test, only two false positive cases and three false negative cases are identified from the testing results, all of which occur in assessing the red background color, which is typically <10 mcd/m^2/lux. Comparison of the results from the proposed method and the ground truth shows that most of the absolute difference is within 3.0 mcd/m^2/lux. Considering the data-driven theoretical-empirical normalization process for beam distance and incidence angle (in Section

4.2.3.1) and the limited number of samples in establishing the correlation curve between the LiDAR retro-intensity and the actual retroreflectivity measurement in the lab (in Section 4.2.4), the sensitivity of the model may introduce errors and propagate them to the final condition assessment result. Such errors could result in the false negative and false positive cases in the final condition assessment, especially when the retroreflectivity is small (i.e. <10 mcd/m^2/lux), e.g. Sign #17.

However, the remaining false negative and false positive cases, i.e. Signs #19, #22, #23 and #34, require further investigation because the absolute differences are relatively large. For white, there is no false positive or false negative case identified. However, some of the estimates have relatively big differences from the ground truth, e.g. Signs #18 and #22. As previously pointed out, the relatively big differences could be introduced by bias in ground truth establishment using retroreflectometer, rather than the estimation error using the proposed method. Therefore, the background of Signs #19, #22, #23, and #34 and the legend of Signs #18 and #22 need further investigation. To further investigate these signs, still images were taken for these traffic signs during nighttime using the geometry and headlight setup as specified in ASTM D4956 (2011).

Signs #19 and #22 – False Negative Cases for Background

The proposed methodology overestimated the retroreflectivity for red in these signs. Figure 5-22(a) shows the nighttime image of Sign #19. It can be observed that the background of the traffic sign is in an overall fair condition. However, three of the four quadrants (left-up, right-up and right-bottom) of the sign are deteriorated more than the rest of the sign. While measuring the retroreflectivity using the handheld retroreflectometer, retroreflectivity from each quadrant was collected. Due to the non-homogeneous deterioration of the sign, the handheld retroreflectometer just happened to be biased on the low values of the sign, while the LiDAR still collected the complete distribution of the sign. Therefore, the result from the proposed methodology overestimated the actual retroreflectivity for red in this sign. This is the intrinsic

drawback of the current ground truth establishment method because the non-homogeneous deterioration of the sign retroreflectivity cannot be seen during the ground truth data collection in daytime. Sign #22 is, also, non-homogeneously deteriorated, which causes the over-estimation in the result. Figure 5-22(b) shows the nighttime and daytime images for Sign #22.

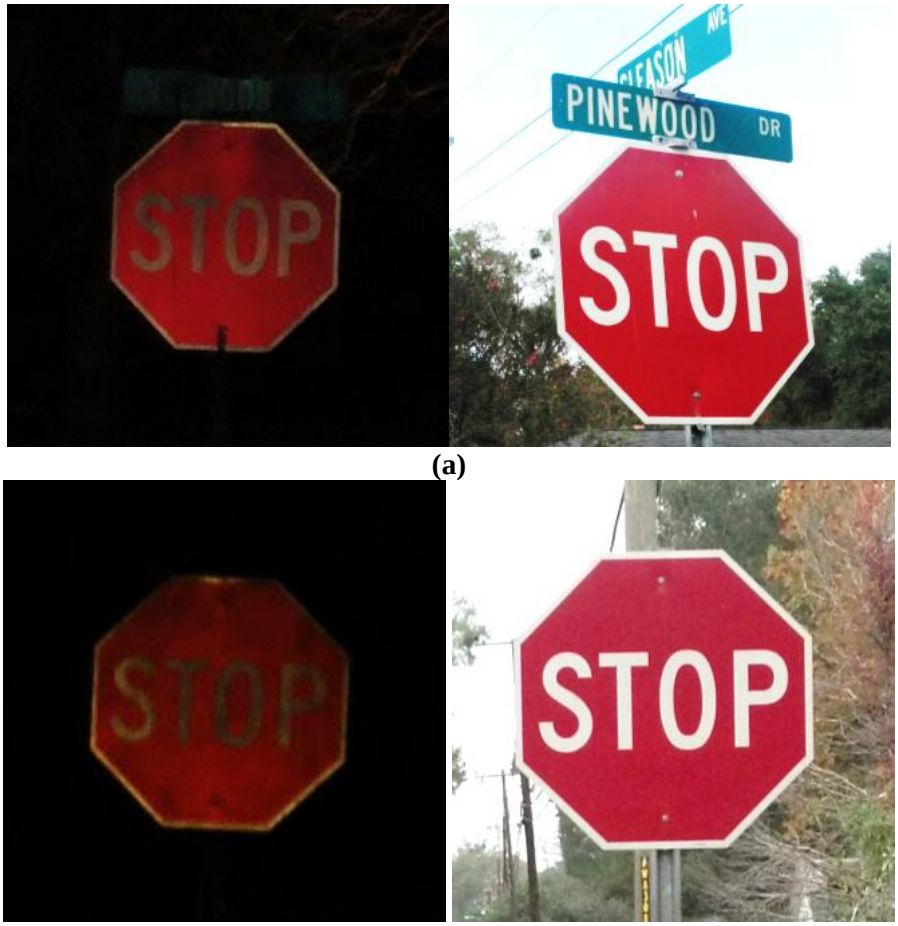

Figure 5-22 Nighttime and daytime images for (a) Sign #19 and (b) Sign #22 (Image enhanced to visualize the defects)

Signs #23 and #34 – False Positive Cases for Background

The proposed methodology underestimated the retroreflectivity for red in these signs. Figure 5-23 shows the nighttime image of Sign #23. It can be observed that the background of the traffic sign is in an overall poor condition due to the water damages for the majority of the sheeting. However, some of the points in good condition were selected

at the four quadrants of each sign where the retroreflectivity using the handheld retroreflectometer. Due to such non-homogeneous deterioration of the sign, the handheld retroreflectometer just happened to be biased on the high values of the sign, while the LiDAR still collected the complete distribution of the sign. Therefore, the proposed methodology underestimated the actual retroreflectivity for red in this sign. This is the intrinsic drawback of the current ground truth establishment method because the non-homogeneous deterioration of the sign's retroreflectivity cannot be seen during the ground truth data collection in daytime, as shown in Figure 5-23(a). Sign #34 also non-homogeneously deteriorated, which causes the underestimation in the result. Figure 5-23(b) shows the nighttime and daytime images for Sign #34.

Figure 5-23 Nighttime and daytime images for (a) Sign #23 and (b) Sign #34 (Image enhanced to visualize the defects)

Signs #18 and #22 – Underestimation Cases for Legend

Similar to the background, the legends of the traffic signs can, also, deteriorate in a non-homogeneous pattern. Parts of the letterings deteriorate more than the rest of the letterings. Since only four points were collected for the legend, the readings cannot cover the complete region of the legend to dictate the true distribution of their retroreflectivity condition. As shown in Figure 5-24, the legends of Signs #18 and #22 are in overall poor condition. However, the ground truth just happened to be collected at the locations where the relatively high retroreflectivity is located.

(a) **(b)**

Figure 5-24 Nighttime images for (a) Sign #18 and (b) Sign #22

5.2.2.3. Result Discussion

As shown in Section 5.2.2.2., the proposed retroreflectivity condition assessment methodology can consistently determine the condition, but the ground truth measured using the handheld retroreflectometer cannot. It is also identified that the current retroreflectometer measurement using four points may not be a consistent and adequate way to define the actual retroreflectivity condition due to the limited measurement. Figure 5-25 shows the populations of the estimated retroreflectivity for the red color of Sign #22. The locations of the four measurements conducted using the handheld retroreflectometer and corresponding values are marked in Figure 5-25. The red bar indicates the median of the population of the estimated retroreflectivity. It can be observed that the limited number of retroreflectometer measurements cannot adequately reflect the true condition of the whole traffic sign. Nevertheless, it is not feasible to manually measure more than 100 points for each traffic sign using a retroreflectometer on

field. Therefore, the proposed method can serve as a better alternative to reliably reflect the true retroreflectivity condition for each sign, since the proposed method assesses the traffic sign retroreflectivity condition using the whole population of the sign-associated LiDAR points.

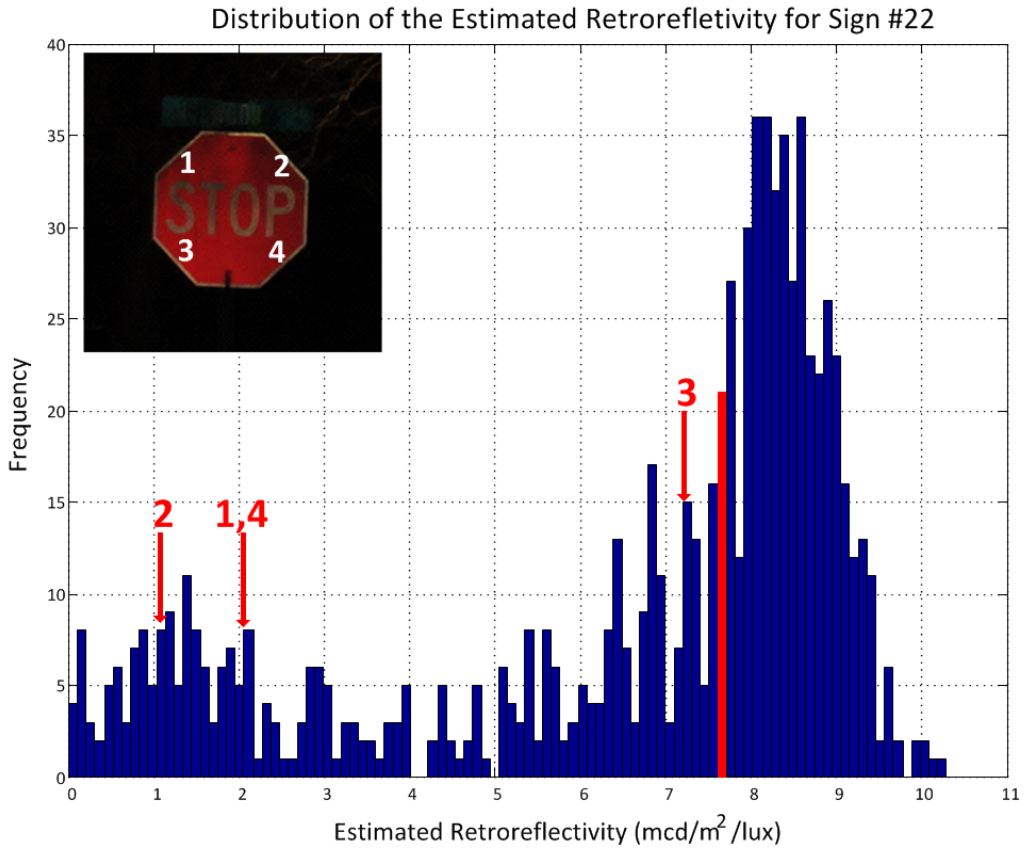

Figure 5-25 Distribution of the estimated retroreflectivity for Sign #22 and the retroreflectometer measurements

Currently, the median value derived from the proposed method is used to represent the whole population of the traffic sign so that the value can be compared with the requirement defined in the MUTCD. Nevertheless, a retroreflectivity condition assessment using the complete population of measurements requirement can also be achieved using the proposed methodology for practical use, which is more consistent with a human's perception during the nighttime. For example, based on the population, it is observed that the majority of the retroreflectivity values (i.e. 61.5% in this case) are still above 7 mcd/m^2/lux, which warrants a "PASS" condition. Therefore, by defining a

conservative percentage (e.g. 50%) of the points that are above the requirement can be an adequate way to determine the overall condition of a traffic sign. It will provide a more reliable and consistent condition assessment result than the current retroreflectometer measurement.

CHAPTER 6

CONCLUSIONS AND RECOMMENDATIONS

Traffic signs are one of the most important roadway assets because they are used to ensure roadway safety and provide important travel guidance/information. Transportation agencies must inventory and manage their traffic signs as required by the Manual of Uniform Traffic Control Devices (MUTCD). Traffic sign inventory and condition assessment are the two most important components in a traffic sign management system to ensure a cost-effective and sustainable traffic sign management system. Traditionally, state departments of transportation (DOTs) conduct manual traffic sign inventory and condition assessment, which is time-consuming, labor-intensive, and sometimes hazardous to field engineers in the roadway environment. Methods have been developed to automate traffic sign inventory and condition assessment using video log images. However, the performance of these methods remains to be improved. There is a need to develop a sensing methodology to achieve a cost-effective traffic sign inventory and condition assessment. This study focuses on two methodologies, one of which is on an enhanced traffic sign detection methodology in support of a cost-effective and reliable image-based traffic sign inventory, while the other is on a new mobile retroreflectivity condition assessment methodology employing the emerging computer vision and mobile light detection and ranging (LiDAR) technologies in support of a cost-effective and reliable traffic sign condition assessment. This chapter summarizes the major contributions and findings of this study and proposes recommendations for future research.

6.1. Contributions

The contributions of this research are the following:

- An enhanced image-based traffic sign detection methodology is proposed and developed to support current state DOTs' traffic sign inventory practices. Two key algorithms are developed to ensure the enhanced methodology produces a reliable outcome.
    - A lighting dependent statistical color model (LD-SCM)-based color segmentation algorithm using local homogeneity features and an artificial neural network (ANN). The developed algorithm is robust to different image lighting conditions, especially adverse lighting;
    - An ordinary/partial differential equation (ODE/PDE)-based shape detection algorithm using a region-based active polygon formulation and a generalized Hough transform (GHT) initialization. The developed algorithm is immune to discontinuous sign boundaries in a cluttered background.
- A mobile traffic sign retroreflectivity condition assessment methodology is proposed and developed to support state DOTs' traffic sign condition assessment practices using the emerging computer vision and mobile LiDAR technologies. Three key methods are developed to ensure the new mobile methodology achieves a reliable and consistent outcome.
    - An image-LiDAR registration method employing camera calibration and point co-planarity to register the 3D LiDAR point cloud with the 2D video log images;
    - A theoretical-empirical normalization scheme to adjust the magnitude of the LiDAR retro-intensity values with respect to LiDAR beam distance and incidence angle based on the radiometric responses;

- A population-based retroreflectivity condition assessment method to evaluate the adequacy of a traffic sign retroreflectivity condition based on the correlation between the normalized LiDAR retro-intensity and the retroreflectivity values.

6.2. Findings

For the enhanced traffic sign detection methodology,

- **The proposed LD-SCM-based color segmentation algorithm is robust to different lighting conditions, including the adverse lighting.**

  Experimental tests show that the proposed algorithm can improve the accuracy of color segmentation under different lighting conditions using the data collected on I-285 and SR-275. A comparison of the color segmentation confusion matrices between the existing color segmentation algorithm (Tsai et al., 2009) and the proposed algorithm shows an average of 20.5% reduction in the miss segmentation rate. Especially, the proposed algorithm can effectively identify the image regions that are affected by the adverse lighting condition and correctly segment the distorted colors under such lighting conditions.

- **The proposed ODE/PDE-based shape detection algorithm is immune to discontinuous sign boundaries in cluttered backgrounds.**

  Experimental tests show that the proposed algorithm can effectively and efficiently identify traffic sign shapes with discontinuous boundaries using the data collected on 37th Street in Savannah, Georgia. A comparison of results from the existing shape detection algorithm (Tsai et al., 2009) and the proposed algorithm shows an 18.1% false negative rate reduction. In addition, the performance of two different region-based ODE/PDE formulations (i.e. an unconstraint active contour model (Ai & Tsai, 2011) and the proposed active polygon model) is compared using the data collected by the Louisiana Department of Transportation and Development (LaDOTD) and the city of Nashville. The proposed active polygon algorithm demonstrates better

performance with a 7.7% false negative rate reduction and, approximately, a 50% processing time reduction.

- **The proposed enhanced traffic sign detection methodology can improve performance by significantly reducing the false negative rate without excessively increasing the false positive rate. More importantly, the enhanced methodology still performs consistently well under different lighting conditions and with discontinuous sign boundaries in cluttered backgrounds.**

  Comprehensive field tests were conducted using the selected five datasets, including an I-95 Interstate route, two state routes (SR-541 and SR-67) and two local routes (Cane Ridge Road and 37th Street). The five datasets also cover different data collection sources and different image qualities. The results show that the proposed enhanced methodology provides an overall improved performance of 15.0% in false negative rate and 14.6% in false positive rate over the existing system, which has a 27.2% false negative rate and a 12.9% false positive rate. It demonstrates a significant reduction of the false negative rate by 12.1%, while having only a slight increase in the false positive rate by 1.7%. Under the challenging lighting conditions and cluttered background conditions, the enhanced methodology can still successfully detect 85.7% and 72.0% of the traffic signs, respectively.

For the new mobile traffic sign retroreflectivity condition assessment methodology, the following are noted:

- **LiDAR beam distance and incidence angle can significantly impact the magnitude of LiDAR retro-intensity values, while the variability of consecutive scans and ambient lighting has minimum impact on the magnitude of LiDAR retro-intensity values.**

  Both theoretical models and empirical simulated tests show that the magnitude of the LiDAR retro-intensity is dependent on the beam distance and incidence angle of the

LiDAR beam. The difference between the raw LiDAR retro-intensity and the normalized LiDAR retro-intensity can be as high as 19.9 mcd/m^2/lux, which will significantly affect the final assessment results. The developed retro-intensity normalization scheme is essential to depict such a difference. The lab tests also show that the variability of consecutive scans and ambient lighting has an ignorable impact on the magnitude of LIDAR retro-intensity. The variation between consecutive scans is less than ± 0.1 mcd/m^2/lux, while the difference among different ambient lighting conditions is within ± 0.08 mcd/m^2/lux.

- **The proposed image-LiDAR registration method can accurately associate the traffic sign detection result and color information with the corresponding LiDAR points.**

  Experimental test results show that the proposed image-LiDAR registration method can accurately associate the sign detection result and color information with the LiDAR point cloud. The absolute distance between the actual traffic sign detection location in image and projected location using the registration method is less than two pixels (i.e. equivalent to less than ½ inch on traffic sign surface). The accurate registration result ensures that different colors of the same traffic sign can be automatically assessed separately using the proposed methodology.

- **The proposed mobile traffic sign retroreflectivity condition assessment methodology can reliably identify the traffic signs with a poor retroreflectivity condition.**

  The preliminary tests were conducted on 35 Type 1 engineer grade stops signs with different in-service lives and retroreflectivity conditions. The red color and the white color of the signs were measured separately. The measurements from the proposed methodology have average differences of 2.2 mcd/m^2/lux and 3.3 mcd/m^2/lux for the red and white sheeting, respectively. Out of the 35 signs, 26 failed due to red sheeting failure, while 25 out of the 35 signs failed due to white sheeting failure. The results

show that 23 out of the 26 signs for red sheeting failure and 25 out of the 25 signs for white sheeting failure were correctly identified. There were only three false negative cases and two false positive cases identified from the tests. Further investigation reveals that most of the false negative and false positive cases are due to the bias of the ground truth measurement using handheld retroreflectometer. The proposed methodology provides more reliable and unbiased condition assessment results than the current handheld retroreflectometer measurement methodology.

6.3. Recommendations for Future Work

For the enhanced traffic sign detection methodology,

- A fuzzy logic-based color segmentation algorithm is recommended to further remove the false negative cases produced by severe casting shadows;
- A relaxed GHT is recommended to further remove the false negative cases produced by occlusions. In addition, a set of more restricted sign candidate verification criteria is recommended consequently to remove additional false positive cases that might be introduced by the relaxed GHT;
- Several specialized traffic sign recognition algorithms are recommended to further remove the false negative cases produced by the small no-parking signs and the object marker signs. These algorithms can be attached in parallel to the proposed methodology without interfering with the current algorithms;
- A traffic sign feature-based confidence scoring scheme is recommended to systematically determine the quality of each detected candidates. Therefore, false positive cases can be systematically reduced by determining an adequate confidence level;
- The developed algorithms for color segmentation and shape detection should be further extended to traffic sign classification by accurately identifying the traffic sign shape and color and associating with new pictogram/character recognition algorithms.

For the new mobile traffic sign retroreflectivity condition assessment methodology,

- Additional field experimental test is recommended using more Type 1 engineer grade stop signs to further validate the performance of the proposed methodology;
- Comprehensive lab and field experimental tests are recommended to thoroughly study the fundamental characteristics of mobile LiDAR retro-intensity in response to different traffic sign reflective sheeting types by improving the current LiDAR retro-intensity normalization model, constructing additional correlation between the normalized retro-intensity values and the corresponding retroreflectivity values, and identifying additional factors that might impact the accuracy of the proposed methodology;
- The proposed traffic sign retroreflectivity condition assessment methodology is recommended to be further extended to assess other traffic sign conditions, e.g. traffic sign color deterioration, traffic sign sheeting cracking, etc.

APPENDIX

CRITICAL ASSESSMENT OF THE EXISTING TRAFFIC SIGN DETECTION ALGORITHM

This appendix presents the validation test designed to critically assess the performance of the existing sign detection algorithm at an image level. The objectives of the validation test is to critically evaluate the causes of false negative (FN) at an image level, to group the FN cases in a way that can be related to algorithm refinement, to reveal the FN categorization and their statistics (frequency) for refinement prioritization, and to study the FN category distribution among different road types for assisting in developing the strategy for refining the sign detection algorithm for practical implementation on different roadways.

The Louisiana Department of Transportation and Development (LaDOTD) collected 37,640 images on three different road types (including interstate, non-interstate rural and non-interstate urban), which were used to evaluate the performance of the generalized sign detection algorithm. The images were taken at an interval of 0.002 mi (approx. 10 ft. or 3 m). Each image has a resolution of 1,300 x 1,030 pixels and in JPEG format. The tested roadways are located in Jefferson Parish, Louisiana, and cover a portion of New Orleans. Although site-based sign detection produced promising results in the previous paper (Tsai et al., 2009), image-based assessment has not been conducted to critically evaluate the performance of the generalized sign detection algorithm. It is crucial to conduct such a detailed test so the technical challenges can be revealed that will provide a direction for the future algorithm refinement.

Four statistical indicators, including true positive (TP), true negative (TN), false positive (FP), and FN, are often used to evaluate the performance of the developed sign detection algorithms. TP means a correct detection/determination of the existence of an

object. TN means the correct detection/determination of the non-existence of an object. FP means an incorrect detection/determination of the non-existence of an object (i.e. there is no sign but the algorithm declares there is a sign). FN means an incorrect detection of the existence of an object (i.e. missing sign detection). FN is an important indicator that can quantitatively evaluate the performance of a sign detection algorithm based on its missing-sign detection rate.

In addition, to evaluate the performance of the generalized sign asset detection algorithm, we can compute the four statistical indicators described above based on either a site-based validation or an image-based validation. For a site-based validation, an FN means none of the images in a cluster are correctly detected as having a sign after evaluating a consecutive (cluster) set of images containing the same traffic sign. As long as one of the images in a consecutive image cluster of containing the same sign correctly detects the sign, we can correctly detect the sign; we consider it to be a correct detection when we can correctly inventory this sign in the inventory. For an image-based validation, each image is evaluated independently. It is based on an image rather than a cluster. Therefore, image-based validation is a more rigid assessment of the generalized sign detection algorithm than site-based. However, this critical assessment is crucial for revealing the insight gained from technical challenges for refining the algorithm refinement.

Figure A-1 shows how an FN image sample is generated to support the image-based validation. First, 37,640 images covering three road types are processed using the generalized sign detection algorithm. Second, image-based validation is then conducted to generate four categories of images, including TP, TN, FP, and FN. Then, 1,192 FN images are used to analyze the causes of false negative detection. These causes are then carefully categorized based on the features used in the developed algorithm and lead to the potential recommendations for the system improvement from both data acquisition algorithm refinement perspectives.

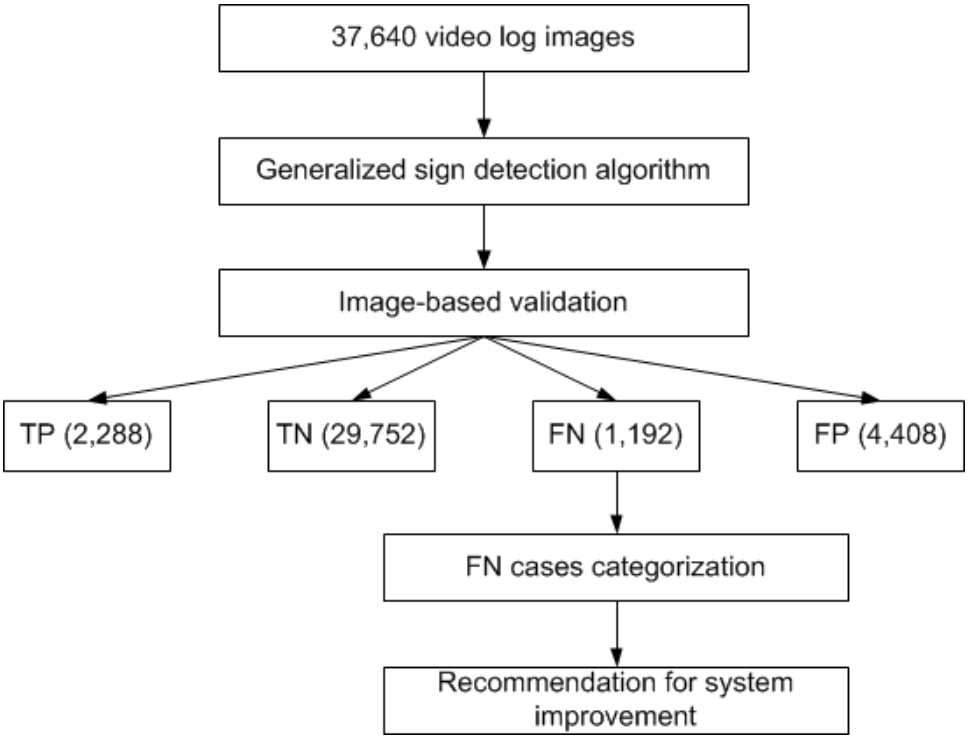

Figure A-1 Flowchart of how an FN images sample is generated to support the image-based validation

A.1. Categorization of the Identified False Negative Cases

To develop a sign detection algorithm to successfully detect the more than 670 types of signs specified in the MUTCD and in the real world environment with different lighting conditions and roadway characteristics is a technical challenge. There is a need to explore the insight of technical challenges that remain. There were 1,192 FN images containing 2,272 FN cases, which are critically assessed, and the causes of false negative detection are carefully identified. These causes are then categorized based on their characteristics related to the key features in the generalized sign detection algorithm so it can assist in defining the potential areas for algorithm refinement. The categorization is based on the fundamental features used in the algorithm, including the color and shape features of the traffic sign. It is likely that the FN cases are developed because the certain features in the traffic sign are not distinct enough from the background based on current mathematical representation of the traffic sign detection algorithm. Six categories of causes that lead to false negative detection are identified. They include the following:

- Variant lighting conditions: Two types of lighting issues are found in the FN cases. One is over-exposure and the other is under-exposure (especially in adverse lighting conditions). The over-exposure and under-exposure cases are the relatively low and high intensity values in the images. The over-exposure cases can be found in the whole image. The adverse lighting cases that can be found have low dynamic range in shadow areas (i.e. traffic sign area) but have normal global contrast (Safonov, et al., 2006). The over-exposure cases are probably produced due to the camera malfunctioning or inappropriate camera iris configuration, while the adverse lighting cases are likely to happen when the data collection vehicle is driving towards the sun and the traffic sign is shaded in its own shadow. Figure A-2 shows the examples of overexposure and back lighting issues.

(a) **(b)**

Figure A-2 Samples of FN cases due to lighting issues
a) over-exposure; b) adverse lighting

- Cluttered background shapes: Cluttered background shapes refer to the background objects that might impact the edge detection and polygon approximation in the algorithm. The cluttered background shapes are usually utility cables, building boundaries, and tree branches. These background shapes can produce additional interfering edges, which can, potentially, impact the polygon approximation of a traffic sign's region. Figure A-3 shows an example of a cluttered background shape FN case.

Figure A-3 Sample of FN cases due to the cluttered background shape

- Similar background and foreground color: Similar background and foreground color refers to the chromatic similarity between the traffic sign and its background. The color similarity can be visually assessed based on the perception of the traffic sign and its background. The Euclidean distance between the average intensity of the traffic sign area and the average intensity of the traffic sign background area is computed to assist the reviewer assesses this type of FN cases (Grest et al., 2003). The common cases are the street name and roadside information signs with green, which are similar to the background green color of tree branches. Some of the information signs with blue are also identified when the image contrast is low. Figure A-4 shows an example of similar background and foreground FN case.

(a) **(b)**

Figure A-4 Samples of FN cases due to similar background and foreground color a) green color; b) blue color

- Occlusion: Occlusion refers to the traffic sign in the video log images that are partially occluded by other objects, such as tree branches, passing vehicles, etc. The occlusion could produce interfering edges in the image and impact the performance of polygon approximation in the algorithm. This case is often identified in urban areas where the roadside vegetation and utilities are closer to the road. Figure A-5 shows an example of an occlusion FN case.

(a) **(b)**

Figure A-5 Samples of FN cases due to occlusion
a) by branches; b) by utility pole

- Small traffic signs: Small traffic signs refer to the pixel size of a traffic sign in which the image is too small for the algorithm to detect. In the process of ground truth establishment, the smallest traffic sign pixel size is 20 by 20. However, in the automatic traffic sign detection algorithm, the small traffic signs extracted in the ground truth might be too small to be identified using the algorithm. The minimum pixel size of 900 (30 x 30) is introduced to help the reviewer to determine this type of FN cases. The common cases are the small no parking signs, milepost, and street name signs on the roadsides. Figure A-6 shows an example of small traffic sign FN case.

(a) **(b)**

Figure A-6 Samples of FN cases due to small traffic signs
a) no parking sign; b) milepost and street name signs

- OM Sign: Different from other traffic signs having a close vertex shape boundary to bound the entire sign (refine it), the OM signs, including OM1-3, OM2-2H and OM2-2V, consist of alternating yellow and black stripes, which cannot formulate a defined boundary. The pattern of this type of sign provides some challenges to the current algorithm because the algorithm must identify the boundary of a sign to approximate the sign. Figure A-7 shows an example of an OM sign FN case.

Figure A-7 Sample of FN cases due to the OM signs

There are 2,272 FN cases that are manually reviewed and categorized based on the six categorizes of causes identified above. Based on statistical analysis, Figure A-8 shows the frequency of the six different categories. The categorization here is not exclusive, which means different causes could be applied for a single image. Therefore, one FN image could have more than one FN case. Based on the statistical analysis,

among the six categorizes, the traffic signs having lighting issues, interfering shapes, and similar background and foreground colors occur the most often. Based on frequency, they could be in a higher priority for algorithm refinement. The areas for the potential algorithm refinement are discussed below to provide researchers future research direction for developing refined sign detection algorithms.

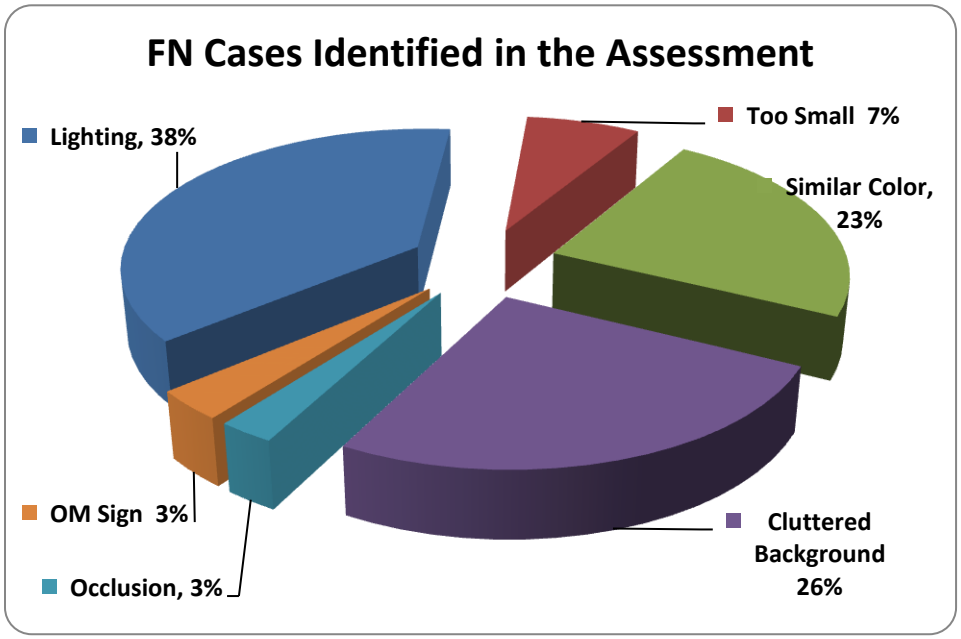

Figure A-8 FN cases distribution from 2,272 FN cases out of 1,192 FN images

A-2. Findings of Areas for Potential Traffic Sign Detection Algorithm Refinement

The potential areas for future algorithm refinement on each category of the FN causes are discussed and recommended below:

- Variant lighting conditions: There are 786 FN cases that are identified with lighting issues, including 565 cases with overexposure issues and 221 cases with back lighting issues. The overexposure issues, it is likely, are caused by the camera malfunctioning, which corrupted the image. To improve this type of FN case, it is recommended that quality control of the collected video log images to filter out the images with camera malfunctioning be done first; then, the automatic traffic sign detection algorithm

should be applied (Tsai & Huang, 2010). Varying lighting conditions are identified as the most frequent reason for FN cases in this study. They result from cameras collecting data from high or low intensity backgrounds, such as the sun or dark sky respectively. Adjusting the data collection time of a day, the camera angles, etc. should be considered to eliminate or minimize such problems. Adverse lighting issues indicate a low dynamic range in dark areas (i.e. traffic sign area), so they can be identified by determining the low dynamic range in the dark area and applying different color segmentation models.

- Cluttered background shapes: There are 535 FN cases that are identified as cluttered background shapes, such as utility cables, building boundaries, and tree branches. These objects produce interfering edges in the polygon detection process. In addition, these cluttered backgrounds will produce discontinuous boundaries after the color segmentation. Therefore, it is technically challenging to use the current image processing method for identifying a set optimized polygon detection parameters that fit all of the collected video log images, including the Canny for edge extraction and the Douglas-Peucker for polygon approximation. However, instead of considering the individual elements of traffic signs (e.g. edges, corners, etc.), taking each traffic sign shape as a whole pattern could, potentially, reduce the impact of cluttered background shapes so as to minimize such FN cases.
- Similar background and foreground color: There are 491 FN cases that are identified as having similar background and foreground colors. Among the 491 FN cases, about 90% of the images contain green or blue and share similar colors with background vegetation. By further exploring the color segmentation step in the current algorithm, it is noticed that the statistical color model (SCM) developed by Tsai, et al. (2009) in the step is established with 413,724 distinct pixels color-tagged with 10 MUTCD colors. However, out of 413,724 distinct pixels, only 1% and 2% of the values are depicted from green and blue colors, respectively. The lack of green and blue samples

is the major reason to produce this type of FN cases. It is recommended that additional green and blue pixel samples be added to the current SCM.

- Occlusion: There are 55 FN cases that are identified as occlusion issues. These FN cases are produced due to partial blockage of the traffic sign by branches and leaves, utility obstacles (due to the tilt of the sign), etc. In the processing of these images using the algorithm, the traffic sign boundaries are broken due to the occlusion. There are two types of occlusions identified in the assessment, including the temporary occlusion and the permanent occlusion. The temporary occlusion is caused by such things as waving tree branches or passing vehicles. For such issues as t analyzing a consecutive cluster of the images using a single camera stereo vision and object tracking method is recommended (Wang et al., 2010) to recover the occluded traffic sign. Permanent occlusion indicates that a traffic sign is partially occluded in all the frames containing this traffic sign. For this type, the stereo vision and tracking methods will no longer work. Considering in the current video log image collection process, each image is geo-referenced with the GPS receiver, retrieving the information from the previous data collection cycle based on the geo-reference to identify the traffic sign change and recover the traffic sign is recommended to minimize the impact of the occlusion issues (Tsai et al., 2010).
- Small traffic signs: There are 150 FN cases that are identified as small traffic signs. These FN cases are produced because either this traffic sign is physically small, such as no-parking sign, milepost, etc., or the traffic signs in the image has been captured from a relatively long distance, which makes the traffic sign captured in the image a small pixel size. From the data acquisition perspective, increasing the camera resolution could provide more pixel size for these small traffic signs, which could help the algorithm identify them. Consequently, the processing time increases for each image because of the high resolution. In addition, using a LiDAR system is recommended to use the unique characteristics of the high retroreflectivity of the

small traffic sign. The high retroreflectivity readings from the small sign's area can be used to locate the small traffic signs and differentiate them from other objects. Currently, the algorithm is using both the Canny edge detection and multi-level threshold to extract contours. There are many contours are spatially overlapped. Within overlapped polygons, if they form a traffic sign candidate, only the most external contours within the nested groups of contour are used as traffic sign candidates. Therefore, for the small traffic signs, there is a chance that the contours of the small traffic signs are ignored if there is a bigger external contour. Releasing this contour selection criterion to maintain all the extracted contours is recommended. Consequently, there will be more traffic sign regions of interest (ROI) produced, and a further enhancement in ROI validation algorithm is still needed.

- OM Signs: There are 255 FN cases are identified. Due to the unique pattern of this type of sign, the current system is challenged to fully identify the traffic sign region using shape feature because, unlike other traffic signs, OM signs do not have a boundary for the algorithm to extract the shape. From a data acquisition perspective, the LiDAR system could also be introduced to minimize the impact of this FN case. Instead of using the depth information to differentiate the foreground and background object, the received retroreflectivity readings from the LiDAR system could be used to locate this type of traffic sign. A subsequent algorithm to extract and validate the region with high retroreflectivity still needs to be developed. From the algorithm refinement perspective, by further testing the OM sign using polygon detection algorithm, it is noticed that instead of identifying the OM sign as a whole polygon, the black and yellow stripes on the sign are always individually identified as multiple polygons side by side. These polygons are further removed by the post validation shown in Chapter 3. Introducing an enhanced post validation criterion to avoid eliminating these side-by-side polygons from the OM sign is recommended. Instead, a polygon merging algorithm could be developed to reconstruct the multiple side-by-

side polygons into a single polygon. Therefore, this kind of FN case could be minimized.

This sub-section discussed and recommended the potential areas for minimizing false negatives. Among the six categories, variant lighting conditions and cluttered background shapes are the most frequent reasons for the FN cases (almost 64% of the FN cases). It should be the high priority for improvement. Again, it is hoped that the findings discussed above will reveal the technical challenges and provide researchers/direction for improvement that can lead to the successful implementation of an intelligent sign inventory system.

REFERENCES

Ai, C., and Tsai, Y. J. (2012). "Hybrid Active Contour-Incorporated Sign Detection Algorithm." *Journal of Computing in Civil Engineering*, 26(1), 28-36.

Appia, V., and Yezzi, A. (2011). "Active geodesics: Region-based active contour segmentation with a global edge-based constraint." *Proc., Computer Vision (ICCV),* , 1975-1980.

ASTM (2009). "ASTM E1709-09 Standard Test Method for Measurement of Retroreflective Signs Using a Portable Retroreflectometer at a 0.2 Degree Observation Angle."West Conshohocken, PA.

ASTM (2011). "ASTM D4956-11a Standard Specification for Retroreflective Sheeting for Traffic Control." West Conshohocken, PA.

Aytac, T., and Barshan, B. (2005). "Surface Differentiation by Parametric Modeling Of Infrared Intensity Scans." *Optical Engineering*, 44(6), 067202-067202.

Bahlmann, C., Zhu, Y., Visvanathan, R., Pellkofer, M., and Koehler, T. (2005). "A System For Traffic Sign Detection, Tracking, and Recognition Using Color, Shape, and Motion Information." *Proc., Intelligent Vehicles Symposium, 2005. Proceedings. IEEE*, 255-260.

Benallal, M., and Meunier, J. (2003). "Real-Time Color Segmentation of Road Signs." *Proc., Electrical and Computer Engineering, 2003. IEEE CCECE 2003. Canadian Conference on*, 1823-1826 vol.1823.

Berk, T., Kaufman, A., and Brownston, L. (1982). "A Human Factors Study of Color Notation Systems for Computer Graphics." *Commun. ACM*, 25(8), 547-550.

Blancard, M. d. S. (1992). "Road Sign Recognition: A Study of Vision-Based Decision Making for Road Environment Recognition." *Vision-based vehicle guidance*, M. Ichiro, ed., Springer-Verlag New York, Inc., 162-172.

BMW (2012). "Traffic Sign Recognition." <http://www.bmw.com/com/en/newvehicles/1series/3door/2012/showroom/safety/traffic_sign_recognition.html>. (March 12th, 2013).

Cambridge Systematics Inc., and Meyer, M. D. (2007). "U. S. Domestic Scan Program: Best Practices in Transportation Asset Management." TRB, Washington, D.C.

Carlson, P., and Picha, D. (2009). *FHWA-CFL/TD-09-005: Sign Retroreflectivity Guidebook for Small Agencies, Federal Land Management Agencies, and Tribal Governments*, Washington, D.C.

Chan, T. F., and Vese, L. A. (2001). "Active Contours without Edges." *Image Processing, IEEE Transactions on*, 10(2), 266-277.

Cheng, W., and Glenn, N. F. (2009). "Integrating LiDAR Intensity and Elevation Data for Terrain Characterization in a Forested Area." *Geoscience and Remote Sensing Letters, IEEE*, 6(3), 463-466.

Chiung-Yao, F., Sei-Wang, C., and Chiou-Shann, F. (2003). "Road-Sign Detection and Tracking." *Vehicular Technology, IEEE Transactions on*, 52(5), 1329-1341.

Cortes, C., and Vapnik, V. (1995). "Support-Vector Networks." *Machine Learning*, 20(3), 273-297.

de la Escalera, A., Moreno, L. E., Salichs, M. A., and Armingol, J. M. (1997). "Road Traffic Sign Detection and Classification." *Industrial Electronics, IEEE Transactions on*, 44(6), 848-859.

de la Escalera, A., Armingol, J. M., and Mata, M. (2003). "Traffic Sign Recognition and Analysis for Intelligent Vehicles." *Image and Vision Computing*, 21(3), 247-258.

de la Escalera, A., Armingol, J. M., Pastor, J. M., and Rodriguez, F. J. (2004). "Visual Sign Information Extraction And Identification by Deformable Models for Intelligent Vehicles." *Intelligent Transportation Systems, IEEE Transactions on*, 5(2), 57-68.

Daniels, J., Ha, L. K., Ochotta, T., and Silva, C. T. (2007). "Robust Smooth Feature Extraction from Point Clouds." *Proc., Shape Modeling and Applications, 2007. SMI '07. IEEE International Conference on*, 123-136.

Dew, G. (2010). "Georeferencing West Virginia DOT's Roadside Assets: An Asset Inventory Case Study." *Proc., AASHTO GIS for Transportation Symposium, Charleston, West Virginia*.

FHWA (2009). "Manual on Uniform Traffic Control Devices for Streets and Highways 2009 Edition (MUTCD 2009)."Washington D.C.

Findley, D. J., Cunningham, C. M., and Hummer, J. E. (2011). "Comparison of Mobile and Manual Data Collection For Roadway Components." *Transportation Research Part C: Emerging Technologies*, 19(3), 521-540.

Foley, J. D., Dam, A. v., Feiner, S. K., and Hughes, J. F. (1995). *Computer Graphics: Principles and Practice in C*, Addison-Wesley Professional.

Garcia-Garrido, M. A., Sotelo, M. A., Martin-Gorostiza, E., and Parra, I. (2006)."Real Time Driving-Aid System for Different Lighting Conditions, on Board a Road Vehicle." *Proc., IEEE Industrial Electronics, IECON 2006 - 32nd Annual Conference on*, 621-626.

Garcia, M. A., Sotelo, M. A., and Gorostiza, E. M. "Traffic Sign Detection in Static Images Using Matlab." *Proc., Emerging Technologies and Factory Automation, 2003. Proceedings. ETFA '03. IEEE Conference*, 212-215 vol.212.

Gil-Jimenez, P., Lafuente-Arroyo, S., Gomez-Moreno, H., Lopez-Ferreras, F., and Maldonado-Bascon, S. (2005). "Traffic Sign Shape Classification Evaluation. Part II. FFT Applied to the Signature of Blobs." *Proc., Intelligent Vehicles Symposium, 2005. Proceedings. IEEE*, 607-612.

Gil-Jimenez, P., Gomez-Moreno, H., Siegmann, P., Lafuente-Arroyo, S., and Maldonado-Bascon, S. (2007). "Traffic Sign Shape Classification Based on Support Vector Machines and The FFT of the Signature of Blobs." *Proc., Intelligent Vehicles Symposium, 2007 IEEE*, 375-380.

Gomez-Moreno, H., Maldonado-Bascon, S., Gil-Jimenez, P., and Lafuente-Arroyo, S. (2010). "Goal Evaluation of Segmentation Algorithms for Traffic Sign Recognition." *Intelligent Transportation Systems, IEEE Transactions on*, 11(4), 917-930.

Gonzalez, A., Garrido, M. A., Llorca, D. F., Gavilan, M., Fernandez, J. P., Alcantarilla, P. F., Parra, I., Herranz, F., Bergasa, L. M., Sotelo, M. A., and Revenga de Toro, P. (2011). "Automatic Traffic Signs and Panels Inspection System Using Computer Vision." *Intelligent Transportation Systems, IEEE Transactions on*, 12(2), 485-499.

Grest, D., Frahm, J. M., and Koch, R. (2003). "A Color Similarity Measure for Robust Shadow Removal in Real Time." *Proc., Vision, Modeling and Visualization (VMV)* 253-260.

Guizzo, E. (2011). "How Google's Self-Driving Car Works." *IEEE Spectrum Inside Technology Magazine*, IEEE Automation.

Haritaoglu, E. D., and Haritaoglu, I. (2003). "Real Time Image Enhancement and Segmentation for Sign/Text Detection." *Proc., Image Processing, 2003. ICIP 2003. Proceedings. 2003 International Conference on*, III-993-996 vol.992.

Hawkins, H., and Carlson, P. (2001). "Sign Retroreflectivity: Comparing Results of Nighttime Visual Inspections with Application of Minimum Retroreflectivity Values." *Transportation Research Record: Journal of the Transportation Research Board*, 1754(-1), 11-20.

Howe, S. J. (2006). "Assessment of Road Signs for Retroreflectivity." *Engineering Asset Management*, J. Mathew, J. Kennedy, L. Ma, A. Tan, and D. Anderson, eds., Springer London, 1080-1089.

Hu, Z., and Tsai, Y. (2011). "Generalized Image Recognition Algorithm for Sign Inventory." *Journal of Computing in Civil Engineering*, 25(2), 149-158.

Huang, Y.-S., Fu, M.-Y., and Ma, H.-B. (2010). "A New Traffic Sign Recognition System with IFRS Detector and MP-SVM Classifier." *Proc., Intelligent Systems (GCIS), 2010 Second WRI Global Congress on*, 23-27.

Janssen, R., Ritter, W., Stein, F., and Ott, S. (1993). "Hybrid Approach For Traffic Sign Recognition." *Proc., Intelligent Vehicles '93 Symposium*, 390-395.

Kaasalainen, S., Ahokas, E., Hyyppa, J., and Suomalainen, J. (2005). "Study Of Surface Brightness From Backscattered Laser Intensity: Calibration Of Laser Data." *Geoscience and Remote Sensing Letters, IEEE*, 2(3), 255-259.

Kamada, H., Naoi, S., and Gotoh, T. (1990)."A Compact Navigation System Using Image Processing and Fuzzy Control." *Proc., Southeastcon '90. Proceedings., IEEE*, 337-342 vol.331.

Kamermann, G. W. (1993). *Laser Radar - Active ElectroOptical Systems, The Infrared & Electro-Optical Systems Handbook*, Optical Engineering Press, SPIE, Michigan.

Kang, D. S., Griswold, N. C., and Kehtarnavaz, N. (1994). "An Invariant Traffic Sign Recognition System Based on Sequential Color Processing and Geometrical Transformation." *Proc., Image Analysis and Interpretation, 1994., Proceedings of the IEEE Southwest Symposium on*, 88-93.

Khan, J. F., Bhuiyan, S. M. A., and Adhami, R. R. (2009). "Distortion Invariant Road Sign Detection." *Proc., Image Processing (ICIP), 2009 16th IEEE International Conference on*, 841-844.

Khan, J. F., Bhuiyan, S. M. A., and Adhami, R. R. (2011). "Image Segmentation and Shape Analysis for Road-Sign Detection." *Intelligent Transportation Systems, IEEE Transactions on*, 12(1), 83-96.

Larson, C., and Skrypczuk, O. (2004). "Comprehensive Data Collection to Support Asset Management at Virginia Department of Transportation." *Transportation Research Record: Journal of the Transportation Research Board*, 1885(-1), 96-103.

Lowe, D. G. "Object Recognition from Local Scale-Invariant Features. (1999)." *Proc., Computer Vision, 1999. The Proceedings of the Seventh IEEE International Conference on*, 1150-1157 vol.1152.

Maldonado-Bascon, S., Lafuente-Arroyo, S., Gil-Jimenez, P., Gomez-Moreno, H., and Lopez-Ferreras, F. (2007). "Road-Sign Detection and Recognition Based on Support Vector Machines." *Intelligent Transportation Systems, IEEE Transactions on*, 8(2), 264-278.

Manay, S., and Yezzi, A. (2003). "Anti-Geometric Diffusion for Adaptive Thresholding and Fast Segmentation." *Image Processing, IEEE Transactions on*, 12(11), 1310-1323.

Marinas, J., Salgado, L., Arrospide, J., and Nieto, M. (2011). "Detection and Tracking of Traffic Signs Using a Recursive Bayesian Decision Framework." *Proc., Intelligent Transportation Systems (ITSC), 2011 14th International IEEE Conference on*, 1942-1947.

Mazzarini, F., Pareschi, M. T., Favalli, M., Isola, I., Tarquini, S., and Boschi, E. (2007). "Lava Flow Identification and Aging by Means of LiDAR Intensity: Mount Etna Case." *Journal of Geophysical Research: Solid Earth*, 112(B2).

McGee, H. W. (2010). "Maintenance of Signs and Sign Supports: A Guide for Local Roads Maintenance Personnel (FHWA-SA-09-025)." Federal Highway Administration, Washington D.C., .

Mishra, R. K., and Zhang, Y. (2012). "A Review of Optical Imagery and Airborne LiDAR Data Registration Methods" *The Open Remote Sensing Journal*, 5, 54-63.

Miura, J., Kanda, T., and Shirai, Y. (2000). "An Active Vision System for Real-Time Traffic Sign Recognition." *Proc., Intelligent Transportation Systems, 2000. Proceedings. 2000 IEEE*, 52-57.

Moreno, O., and Cook, R. T. (2010). "Presentation: Phoenix Sign Inventory and Replacement." Parsons Brinckerhoff Inc.

Mumford, D., and Shah, J. (1989). "Optimal Approximations by Piecewise Smooth Functions and Associated Variational Problems." *Communications on Pure and Applied Mathematics*, 42(5), 577-685.

Murakami, M., and Honda, N. (1996). "An Exposure Control System of Video Cameras Based on Fuzzy Logic Using Color Information." *Proc., Fuzzy Systems, 1996., Proceedings of the Fifth IEEE International Conference on*, 2181-2187 vol.2183.

NGA (2009). "NGA.SIG.0004_1.0: Lighting Detection and Ranging (LiDAR) Sensor Model Supporting Precise Geo-positioning." *National Center for Geospatial Intelligence Standards*.

NCDOT (2011). "Overhead Sign Inventory." <http://www.ncdot.org/doh/preconstruct/traffic/congestion/sign/inven/>. (Sept. 1st, 2011).

Nguwi, Y.-Y., and Kouzani, A. (2008). "Detection And Classification of Road Signs in Natural Environments." *Neural Computing & Applications*, 17(3), 265-289.

Nunn, C., Kummert, A., and Muller-Schneiders, S. (2008). "A Novel Region of Interest Selection Approach for Traffic Sign Recognition Based on 3D Modelling." *Proc., Intelligent Vehicles Symposium, 2008 IEEE*, 654-659.

Ohta, Y.-I., Kanade, T., and Sakai, T. (1980). "Color Information for Region Segmentation." *Computer Graphics and Image Processing*, 13(3), 222-241.

Osher, S., and Sethian, J. A. (1988). "Fronts Propagating with Curvature-Dependent Speed: Algorithms Based on Hamilton-Jacobi Formulations." *Journal of Computational Physics*, 79(1), 12-49.

Paclik, P., Novovicova, J., and Duin, R. P. W. (2006). "Building Road-Sign Classifiers Using a Trainable Similarity Measure." *Intelligent Transportation Systems, IEEE Transactions on*, 7(3), 309-321.

Pao, Y. H., and Takefuji, Y. (1992). "Functional-Link Net Computing: Theory, System Architecture, and Functionalities." *Computer*, 25(5), 76-79.

Paoly, D., and Staud, A. B. (2010). "Use of MobileGIS for Sign Inventories." *Proc., AASHTO GIS for Transportation 2010*.

Parada-Loira, F., and Alba-Castro, J. L. (2010). "Local Contour Patterns for fast traffic sign detection." *Proc., Intelligent Vehicles Symposium (IV), 2010 IEEE*, 1-6.

Paulo, C. F., and Correia, P. L. (2007). "Automatic Detection and Classification of Traffic Signs." *Proc., Image Analysis for Multimedia Interactive Services, 2007. WIAMIS '07. Eighth International Workshop on*, 11-11.

PennDOT (2010). "Pennsylvinia Department Transportation Online VideoLog Roadway Management System." Bureau of Maintenance and Operatioins Pennsylvinia Department Transportation, ed.

Pfeifer, N., Dorninger, P., Haring, A., and Fan, H. (2007). "Investigating terrestrial laser scanning intensity data: quality and functional relations." *Proc., 8th Conference on Optical 3-D Measurement Techniques*, 328 - 337.

Piccioli, G., De Micheli, E., Parodi, P., and Campani, M. (1994). "Robust Road Sign Detection and Recognition from Image Sequences." *Proc., Intelligent Vehicles '94 Symposium, Proceedings of the*, 278-283.

Piccioli, G., De Micheli, E., Parodi, P., and Campani, M. (1996). "Robust Method for Road Sign Detection and Recognition." *Image and Vision Computing*, 14(3), 209-223.

Rasdorf, W., Hummer, J. E., Harris, E. A., and Sitzabee, W. E. (2009). "IT Issues for the Management of High-Quantity, Low-Cost Assets." *journal article*, 23(2), 91-99.

Remias, S. M., Hubbard, S. M. L., Eric A. Hulme, E. I., Hainen, A. M., Farnsworth, G. D., and Bullock, D. M. (2011). "Bias and Uncertainty in Traffic Sign Retroreflectivity." *Journal of Transportation of ITE*, 1(1), 19.

Retterath, J. E., and Laumeyer, R. A. (2008). "System for Automated Determination of Retroreflectivity of Road Signs and Other Reflective Objects." Facet Technology Corporation, US, 26.

Retterath, J. E., and Laumeyer, R. A. (2011). "System for Road Sign Sheeting Classification." Facet Technology Corp., US.

Ruta, A., Yongmin, L., and Xiaohui, L. (2008). "Detection, Tracking and Recognition of Traffic Signs from Video Input." *Proc., Intelligent Transportation Systems, 2008. ITSC 2008. 11th International IEEE Conference on*, 55-60.

Ruta, A., Li, Y., and Liu, X. (2010). "Real-Time Traffic Sign Recognition from Video By Class-Specific Discriminative Features." *Pattern Recognition*, 43(1), 416-430.

Safonov, I. V., Rychagov, M. N., Kimin, K., and Sang Ho, K. (2006). "Automatic Correction of Exposure Problems in Photo Printer." *Proc., Consumer Electronics, 2006. ISCE '06. 2006 IEEE Tenth International Symposium on*, 1-6.

Sandoval, H., Hattori, T., Kitagawa, S., and Chigusa, Y. (2000). "Angle-Dependent Edge Detection for Traffic Signs Recognition." *Proc., Intelligent Vehicles Symposium, 2000. IV 2000. Proceedings of the IEEE*, 308-313.

Sheikh, H. R., and Bovik, A. C. (2005). "Information Theoretic Approaces to Image Quality Assessment." *Handbook of Image and Video Processing*, Elsevier.

Siegmann, P., Lopez-Sastre, R. J., Gil-Jimenez, P., Lafuente-Arroyo, S., and Maldonado-Bascon, S. (2008). "Fundaments in Luminance and Retroreflectivity Measurements of Vertical Traffic Signs Using a Color Digital Camera." *Instrumentation and Measurement, IEEE Transactions on*, 57(3), 607-615.

Smith, K., and Fletcher, A. (2001). "Evaluation of the FHWA's Sign Management and RetroReflectivity Tracking System (SMARTS) Van (FHWA-AK-RD-01-01)." Alaska Department of Transportation, Juneau, AK, .

Tsai, R. (1987). "A Versatile Camera Calibration Technique for High-Accuracy 3DMachine Vision Metrology Using Off-The-Shelf TV Cameras and Lenses." *Robotics and Automation, IEEE Journal of*, 3(4), 323-344.

Tsai, Y., Kim, P., and Wang, Z. (2009). "Generalized Traffic Sign Detection Model for Developing a Sign Inventory." *Journal of Computing in Civil Engineering*, 23(5), 266-276.

Tsai, Y., Hu, Z., and Chris, A. (2010). "Detection of Roadway Sign Condition Changes Using Multi-Scale Sign Image Matching (M-SIM)." *Photogrammetric Engineering and Remote Sensing.*, 76(4), 15.

Tsai, Y., and Huang, Y. (2010). "Automatic Detection of Deficient Video Log Images Using a Histogram Equity Index and an Adaptive Gaussian Mixture Model." *Computer-Aided Civil and Infrastructure Engineering*, 25(7), 479-493.

Vemuri, V. R. "Main Problems and Issues in Neural Networks Application. (1993)." *Proc., Artificial Neural Networks and Expert Systems, 1993. Proceedings., First New Zealand International Two-Stream Conference on*, 226.

Voegtle, T., and Wakaluk, S. (2009). "Effects on the Measurements of the Terrestrial Laser Scanner HDS 6000 (LEICA) Caused by Different Object Material." *Laser Scanning 2009 IAPRS*, Paris, France.

Volkswagan (2010). "Online Services and Dynamic Main Beam Control Arrive in the Phaeton." <https://www.volkswagen-media-services.com/medias_publish/ms/content/en/pressemitteilungen/2010/04/22/phaeton_debuts_with.standard.gid-oeffentlichkeit.html>. (March 10th, 2013).

Wang, K. C. P., Hou, Z., and Gong, W. (2010). "Automated Road Sign Inventory System Based on Stereo Vision and Tracking." *Computer-Aided Civil and Infrastructure Engineering*, Feb Online.

Wei, L., Jin, L., Haihua, G., Bobo, D., Huai, Y., and Hong, Z. (2011). "An Efficient Real-Time Speed Limit Signs Recognition Based on Rotation Invariant feature." *Proc., Intelligent Vehicles Symposium (IV), 2011 IEEE*, 1000-1005.

Wolshon, B. (2003). "Louisiana Traffic Sign Inventory and Management System Report-381." Louisiana Tranportation Research Center, Baton Rouge.

Wu, J., and Tsai, Y. (2006). "Enhanced Roadway Inventory Using a 2-D Sign Video Image Recognition Algorithm." *Computer-Aided Civil and Infrastructure Engineering*, 21(5), 369-382.

Zhang, Z. (2000). "A Flexible New Technique for Camera Calibration." *Pattern Analysis and Machine Intelligence, IEEE Transactions on*, 22(11), 1330-1334.